

8. SITE 1237¹

Shipboard Scientific Party²

INTRODUCTION

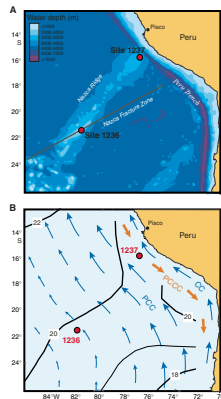
Site 1237 (proposed Site NAZCA-17A) is located at 16°0.421'S, 76°22.685'W, ~140 km off the coast of Peru (Fig. F1A). The site lies on a relatively flat bench (Fig. F2) on the easternmost flank of Nazca Ridge at a water depth of 3212 m. Nazca Ridge, a fossil hotspot track with its modern expression at Easter Island, terminates just outboard of the Peru-Chile Trench, where it is deformed and subducted beneath Peru. About 19 km west of Site 1237, an abrupt scarp (probably an active normal fault) rises to the summit of Nazca Ridge.

Eastern Nazca Ridge is covered by a thick drape of pelagic sediment to its shallowest reaches. The total thickness of the sedimentary section at Site 1237 is estimated at 280–300 m based on site survey seismic profiles (Fig. F3). The seismic record reveals well-stratified reflective layers, which clearly drape the underlying bathymetry from the sediment surface to acoustic basement, which may be either basalt or lithified sediment.

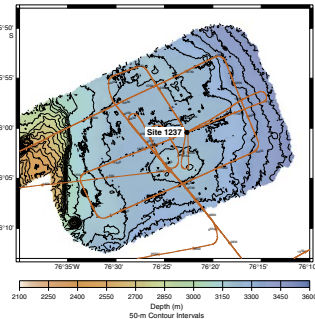
Basement ages are expected to be between 40 and 45 Ma, based on magnetic anomalies of the surrounding oceanic crust (Cande and Haxby, 1991). If we assume that the Nazca Ridge was formed at the Easter Island hotspot, then the age difference between the basement of the ridge and adjoining plate may only be a few million years. Therefore, triple coring with the advanced piston corer (APC) at Site 1237 had the potential of providing a continuous pelagic record that spans much of Neogene time and a potentially into the Paleogene.

The tectonic backtrack path on the Nazca plate moves Site 1237 about 20° westward relative to South America over the past 42 m.y. (Fig. F4). Removal of thermal subsidence effects would predict that the site was at shallower water depths early in its history. Although backtracking water depths is difficult on oceanic rises, we expect that the site may have risen to within a few kilometers of sea level in its early his-

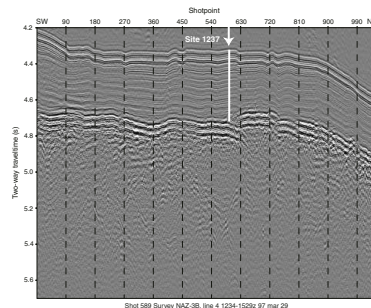
F1. Sites 1236 and 1237 and oceanographic features off Peru and northern Chile, p. 29.



F2. High-resolution swath bathymetry at Site 1237, p. 30.



F3. Seismic profile at Site 1237, p. 31.



¹Examples of how to reference the whole or part of this volume.

²Shipboard Scientific Party addresses.

tory. Uncertainties in this calculation include effects of faulting during the approach of the site to the Peru-Chile Trench, the inferred scarp just west of Site 1237 has a bathymetric expression of ~600 m, and an unknown history of movement.

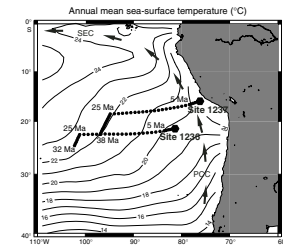
Today, Site 1237 is situated near the eastern edge of the northward-flowing Peru-Chile Current (Fig. F1B), a major conduit of cool-water transport from high to low latitudes. The site's position near the productive upwelling systems of Peru suggests that it may record changes in upwelling and biological production in this eastern boundary current setting (Fig. F5). Plate tectonic backtrack locations can be used to predict general features of paleoceanographic change at Site 1237 under the assumptions that overall conditions in the region remained constant over time and that the only change in the system is drift of the site location relative to this fixed oceanographic background (Fig. F6). In this analysis, we ignore the relatively small changes in the position of the South American margin through time. Sampling of modern oceanographic atlas values at the paleosite locations suggests that 25–30 m.y. ago, sea-surface temperatures at Site 1237 should have been ~2.5°C higher (and salinities 0.7 higher) than today. Pycnocline depth changes significantly along the backtrack path, starting at values of 70–80 m prior to 20 Ma and shallowing in steps to values of 25 m in the past 1 m.y. Sea-surface nutrient concentrations of silicate, phosphate, and nitrate would have been generally lower than at present with a pronounced increase after ~8 Ma. Modern primary productivity roughly follows sea-surface temperature trends along the backtrack path and implies that 30 m.y. ago primary productivity would have been less than one-third of its present value at the site. Thus we expect lower biogenic sedimentation rates and relatively minor amounts of terrigenous sediment with greater age at Site 1237. Significant deviations from these general trends, if detected in the sediment cores, would imply changes in regional oceanographic conditions or errors in the tectonic backtrack model. In its older intervals, the geologic record at Site 1237 is likely to resemble that of Site 1236, although Site 1237 probably resided at somewhat greater water depths than Site 1236 throughout its history.

The modern water depth of Site 1237 reflects the transition zone between the relatively oxygen rich (nutrient depleted) remnants of Circumpolar Deep Water (CPDW) that enter the Peru Basin as bottom water through the Peru-Chile Trench (Lonsdale, 1976) and the relatively oxygen-depleted (nutrient rich) Pacific Central Water (PCW) (Tsuchiya and Talley, 1998). In the Pliocene–Pleistocene interval, Site 1237 may record variations in carbonate preservation associated with changes in deepwater masses and global carbonate budgets. A tectonic backtrack to shallower depths suggests that it may have occupied depths of the modern PCW (or its paleoequivalent) during its early history (Fig. F7). The apparent fault scarp to the west (Fig. F3) suggests a step up to paleo-depths perhaps 600 m shallower than the present location within the past few million years.

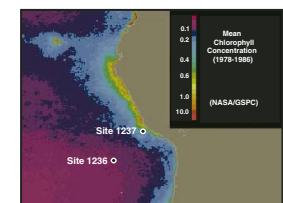
The primary objective at Site 1237 is to provide a continuous sedimentary sequence of the Neogene and Quaternary and as complete as possible a record of older intervals to

1. Improve on regional Cenozoic timescales by combining magnetostratigraphy, biostratigraphy, and isotopic stratigraphy (and perhaps orbital tuning) in a region midway between the tropical and high-latitude systems;

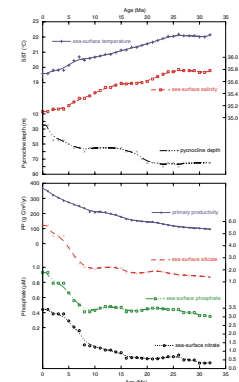
F4. Tectonic backtrack of Site 1237, p. 32.



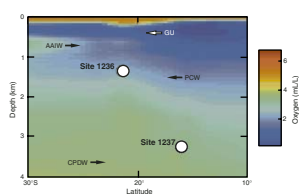
F5. Chlorophyll distributions in surface waters of the southeast Pacific, p. 33.



F6. Modern ocean properties at backtrack locations of Site 1237, p. 34.



F7. Meridional cross section of water masses, p. 35.



2. Assess climate changes of the southern subtropical Pacific over the past ~40 m.y., focusing on major intervals of changing climate (e.g., the early Miocene intensification in Antarctic glaciation [~24 Ma], the middle Miocene climatic optimum [14–15 Ma], the glaciation of the East Antarctic Ice Sheet [~13 Ma], the mid-Pliocene intensification of Northern Hemisphere glaciation [3.1–2.6 Ma], and the transition from early Pleistocene climate cycles dominated by ~41-k.y. rhythms to those of the late Pleistocene that are dominated by ~100-k.y. rhythms);
3. Examine the climatic responses of the subtropical gyre and eastern boundary current system to globally significant tectonic events, including the opening of Drake Passage (~25 Ma) (Barker and Burrell, 1977) and closure of the Isthmus of Panama (10–4 Ma, and especially the final closure after 4.6 Ma) (Haug and Tiedemann, 1998); and
4. Reconstruct changes in the boundary between PCW and CPDW on orbital and tectonic timescales.

OPERATIONS

The 432-nmi voyage to Site 1237 (proposed Site NAZCA-17A) was accomplished in 39.0 hr at an average speed of 11.1 kt. At 0340 hr on the morning of 26 April 2002, the vessel left Chilean waters and entered the territorial waters of Peru. During the evening of 26 April, the vessel received permission to operate in the national waters of Peru (Peruvian Navigation Permit 067-2002). On approach to site, the 3.5-kHz precision depth recorder (PDR) was used as a final check of site characteristics by comparison to precruise survey data. The vessel was positioning on the coordinates of Site 1237 by 2020 hr.

Hole 1237A

After the drill string was deployed to a depth of 3203 meters below rig floor (mbrf), the top drive was picked up and spaced out to a depth of 3225 mbrf. Hole 1237A was initiated with the APC at 0355 hr on 27 April. The core barrel was full (i.e., the mudline was not recovered), and the hole was terminated.

Hole 1237B

Hole 1237B was initiated with the APC at 0505 hr. The bit was positioned 5 m shallower than in Hole 1237A (3220 mbrf), and the mudline was recovered. The seafloor depth estimated by the amount of recovery was 3224.0 mbrf, 9.4 m shallower than the corrected PDR estimate. Piston coring advanced until the wireline parted at the rope socket while we attempted to recover Core 13H (110.0–119.5 meters below seafloor [mbsf]). An extra wireline trip was made with a core barrel fishing tool, and the tensor tool and sinker bars were retrieved. The shear pin on the sinker bars had also parted and an additional wireline run was needed to recover the barrel containing Core 13H.

APC coring resumed and deepened Hole 1237B to 317.4 mbsf, where Core 34H failed to achieve a full stroke with the APC (Table T1). During coring operations in this hole, permission was granted from Ocean Drilling Program/Texas A&M University (ODP/TAMU) headquarters to deepen the hole by as much as 30 m beyond the mandated 300 mbsf

maximum depth prescribed by the Pollution Prevention and Safety Panel (PPSP), as long as it could be accomplished with fully stroked piston cores. The core barrels containing Cores 20H through 34H were drilled over when they could not be pulled free of the sediment with a force of 60 klb. The nonmagnetic core barrel was deployed on even-numbered cores up to and including Core 20H (Table T1). The nonmagnetic core barrel was not used after this to prevent potential damage to the barrel as a result of the drilling-over process. The cores were oriented starting with Core 3H. Downhole temperature measurements were taken with the APC temperature (APCT) tool at various depths (Table T1). A total of 317.4 m was cored and 331.4 was recovered (Table T1). This represented the deepest penetration with the APC since Leg 162. To our knowledge, only four other piston-cored holes in ODP history had exceeded a penetration of 300 m: Leg 162, Hole 981A (320.0 mbsf); Leg 145, Hole 882A (398.3 m); and Leg 130, Holes 806B and 806C (320.0 and 309.6 mbsf, respectively).

Hole 1237C

The vessel was moved 10 m west. Prior to coring, a bottom water temperature measurement was obtained with the APCT tool with the bit positioned just above the seafloor. To obtain the desired stratigraphic overlap with the first hole, the bit was then positioned at 3223 mbrf and Hole 1237C was initiated with the APC at 0941 hr on 29 April. The seafloor depth inferred by the recovery of the initial core was 3223.2 mbrf. Piston coring deepened the hole to 315.3 mbsf, where Core 33H failed to achieve a full stroke. A total of 313.3 m was cored and 323.7 m recovered (recovery = 103%) (Table T1) in Hole 1237C.

The core barrels containing Cores 17H through 19H and 21H through 33H were drilled over. The nonmagnetic core barrel was deployed on odd-numbered cores up to and including Core 17H (Table T1). To maintain a stratigraphic overlap with the previous data, the interval from 113.8 to 115.8 mbsf was drilled. The cores were oriented starting with Core 3H. Downhole temperature measurements were taken with the APCT tool (Table T1). The thermal gradient at Site 1237, estimated from the temperature measurements in Holes 1237B and 1237C, was ~3.1°C/100 m. The bit was pulled free of the seafloor at 0325 hr on 1 May.

Hole 1237D

After the vessel was moved 10 m west, Hole 1237D was initiated with the APC at 0445 hr on 1 May. The objective for this hole was to spot-core intervals to cover coring gaps left in the previous holes. Another 11 piston cores were obtained, representing a cored interval of 104.5 m with 106.1 m recovered (Table T1). Cores were oriented starting with Core 3H. Four intervals were drilled in this hole: 0–2.8, 40.8–69.8, 79.3–80.3, and 108.8–224.5 mbsf. The total drilled interval amounted to 148.5 m. The nonmagnetic core barrel was deployed on Cores 2H, 4H, 6H, and 8H. The core barrels containing Core 9H through 11H (224.5–253.0 mbsf) were drilled over.

The vessel was secured for transit and left location at 0300 hr on 2 May.

COMPOSITE SECTION

We built a meters composite depth (mcd) scale and a splice from 0.00 to 360.36 mcd (as defined in “[Composite Section](#),” p. 4, in the “Explanatory Notes” chapter) that ranges from the top of Core 202-1237B-1H to the bottom of Section 202-1237B-34H-7 (Tables [T2](#), [T3](#)). All cores collected at Site 1237 were included in the composite.

The mcd scale and the splice are based on the stratigraphic correlation of the whole-core OSU Fast Track magnetic susceptibility data (OSUS-MS) collected at 5-cm intervals with 10-s integrations (Tables [T4](#), [T5](#), [T6](#), [T7](#)). In two intervals, 119–124 and 270–275 mcd, we also used natural gamma radiation (NGR) data, collected at 2.5-cm intervals with 5-s counts, and color reflectance (L^* and b^*), measured at 2.5-cm intervals, to correlate between holes. Tie points were then used to construct representative spliced records for color reflectance (L^* , a^* , and b^*) and multisensor track data (MST-MS) (Fig. [F8](#)).

We assumed that the uppermost sediment (the “mudline”) in Core 202-1237B-1H was the sediment/water interface. A mudline was also recovered in Core 202-1237C-1H, and this confirmed the fidelity of the top of the recovered section. Core 202-1237B-1H, the “anchor” in the composite depth scale, is the only core with depths that are the same on the mbsf and mcd scales. From this anchor, we worked downhole, correlating records on a core-by-core basis. The correlation between holes is not well constrained in three intervals: 120–123, 258–262, and 270–275 mcd. Final correlation of the multiple holes drilled at Site 1237 in these intervals will require additional shore-based analysis. The first interval (~121.5 mcd) includes the tie between Cores 202-1237C-12H and 202-1237B-13H (Fig. [F9D](#)). In this interval we used NGR in conjunction with OSUS-MS data to develop the composite section. The second interval (~260 mcd) in the middle of Core 202-1237C-25H was also recovered in Cores 202-1237B-25H and 26H as well as 202-1237D-9H and 10H (Fig. [F9I](#)). In this interval, the long-period variation in magnetic susceptibility was used for correlation, whereas some high-frequency spikes in magnetic susceptibility were ignored. The third interval (~273 mcd) includes the tie between the base of Core 202-1237C-26H and the top of Core 202-1237B-27H (Fig. [F9I](#)). Here, color reflectance (b^*) was used to aid in correlation.

A comparison of the mcd and mbsf depth scales (Fig. [F10](#)) shows that, unlike the first five sites drilled during Leg 202, the cumulative offset between mcd and mbsf within the splice is not linear, and thus, the growth factor is not constant. The mcd growth factor for the spliced interval at Site 1237 varies between 1.09 and 1.20. In Cores 202-1237B-1H through 16H (0.00–160.91 mcd), 202-1237C-1H through 16H (0.05–167.20 mcd), and 202-1237D-1H through 8H (2.30–116.32 mcd), mcd grows 9% relative to mbsf. In Cores 202-1237B-17H through 25H (162.80–259.49 mcd), 202-1237C-17H through 25H (167.65–263.93 mcd), and 202-1237D-9H (248.65–258.55 mcd), mcd grows at a rate of 13% relative to mbsf. Finally, from Cores 202-1237B-26H to 34H (259.15–360.61 mcd), 202-1237C-26H to 33H (264.65–354.18 mcd), and 202-1237D-10H to 11H (258.90–281.44 mcd), mcd increases at a rate of 20% relative to mbsf. These three intervals are marked by the blue lines in Figure [F10](#).

In order to facilitate the calculation of mass accumulation rates (MARs), we provide corrected meters composite depth (cmcd) (see “[Composite Section](#),” p. 4, in the “Explanatory Notes” chapter), a scale

[T2. Composite depth scale, p. 75.](#)

[T3. Splice tie points, p. 77.](#)

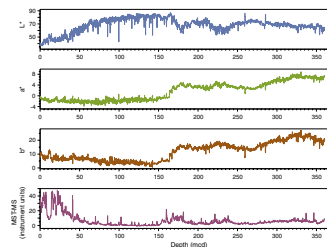
[T4. OSUS-MS measurements, Hole 1237A, p. 78.](#)

[T5. OSUS-MS measurements, Hole 1237B, p. 79.](#)

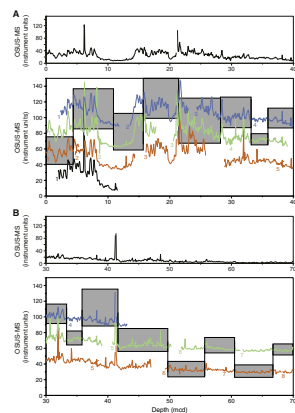
[T6. OSUS-MS measurements, Hole 1237C, p. 80.](#)

[T7. OSUS-MS measurements, Hole 1237D, p. 81.](#)

[F8. OSUS-MS vs. mcd, p. 36.](#)



[F9. Spliced records of \$L^*\$, \$a^*\$, and \$b^*\$ and MST-MS, p. 37.](#)



that corrects for the growth factor and adjusts the mcd to the length of the drill string, the approximate in situ depth. Equations for calculating cmcd for any depth in the composite section are provided in Table T2. The equations are defined by four tie points that can be used to transfer, by linear interpolation, mcd into cmcd in three intervals. The intervals are illustrated in Figure F10 and tabulated in Table T2.

LITHOSTRATIGRAPHY

A 360.65-m-thick (hemi)pelagic sequence was recovered at Site 1237, spanning the interval from the early Oligocene to the Holocene. Clay-rich lithologies dominate the uppermost ~100 mcd, whereas nannofossil ooze is present in the lower ~260 mcd.

The sedimentary sequence at Site 1237 was divided into two major lithologic units (I and II), with each unit divided into two subunits (Table T8; Fig. F11). Unit I lithologies are rich in both terrigenous material and siliceous microfossils with various contributions from calcareous microfossils (Fig. F12). Subunit IA primarily consists of diatom- and/or nannofossil-bearing (silty) clay, and Subunit IB contains clayey nannofossil ooze. Unit II is composed of nannofossil ooze; Subunits IIA and IIB differ in micrite abundance. Differences among units and subunits are clearly apparent in color reflectance as well (Fig. F13). Ash layers are present between 0 and 167 mcd, frequently intercalated in Subunits IA through IIA (Fig. F14; Table T9).

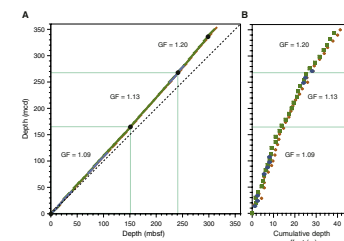
For the upper ~148 mcd of the sedimentary sequence (Unit I through Subunit IIA), preliminary predictive relationships between reflectance and carbonate and total organic carbon (TOC), via a multiple linear regression, are strong for both carbonate and TOC ($r^2 = \sim 0.8$ and ~ 0.9 , respectively). Reflectance spectra show that goethite and hematite are present in Subunit IIB and confer a reddish color to the sediment.

The interval from early Oligocene to early Pliocene (Unit II) is marked by pelagic sedimentation. The transition toward a more hemipelagic environment since the early Pliocene (Unit I) is indicated by the increased siliciclastic component toward recent times and is consistent with the eastward motion of the Nazca plate, which moved Site 1237 to its modern position ~140 km off the coast of Peru (see “Introduction,” p. 1).

Minor siliciclastic components (goethite, hematite, and clay minerals) within the nannofossil ooze may indicate eolian transport of sediments to the site via the southeast trade winds from inferred arid areas of subtropical South America. The iron oxyhydroxides disappear in the upper Miocene (~8 Ma) section, probably as a result of the establishment of a reducing environment in response to an increase in the total organic carbon flux. Nevertheless, a simultaneous increase in the flux of total siliciclastic components suggests enhanced eolian supply since ~8 Ma.

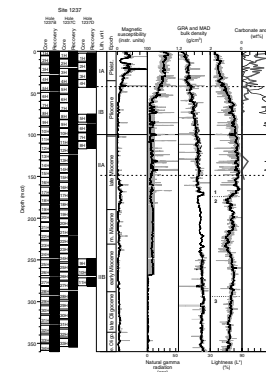
Fifty-five ash layers at Site 1237 record volcanic eruptions from andesitic sources since ~9 Ma (Fig. F14). In the section older than 9 Ma, ash layers are essentially absent. The presence of ash layers since 9 Ma and maxima in ash layer frequency at ~7.5 Ma and between 3 and 1 Ma may reflect major phases of explosive volcanic activity, possibly associated with major phases of Andean uplift. However, variations in ash layer frequency are also influenced by a transport function that is linked to the paleoposition of Site 1237 or to climate-related variations in the strength and direction of atmospheric circulation. Andean up-

F10. A comparison of the mbsf and mcd scales, p. 43.

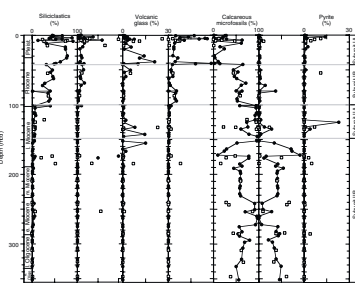


T8. Definition and description of lithologic units and subunits, p. 82.

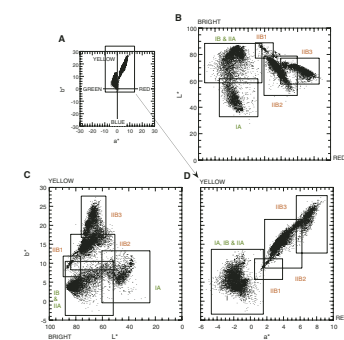
F11. Lithostratigraphic summary, Site 1237, p. 44.



F12. Major components in smear slides, p. 45.



F13. Color measurements, Site 1237 (spliced record), p. 46.



lift, in turn, may have exerted more influence on the regional wind and precipitation patterns, changing the climatic conditions in South America.

Description of Lithologic Units

All lithologic units and subunits are defined by visual description, smear slide analyses, and color reflectance measurements and are further supported by trends in magnetic susceptibility and NGR (Fig. F11). However, lithologic changes between units are gradational. Therefore, we chose to define each of these transitional intervals of unit and sub-unit boundaries at the base of an appropriate ash layer identifiable in all holes (Fig. F15).

Technical problems with the gamma ray attenuation (GRA) bulk density sensor affected the data in the interval between ~170 and 240 mcd in Hole 1237B and in most intervals of Holes 1237C and 1237D. For the intervals in Hole 1237B where GRA bulk density measurements are reliable, they are highly correlated ($r^2 = 0.9$) in a 1:1 relationship to the moisture and density (MAD) bulk density measurements. The smooth exponential downhole increase in both GRA and MAD bulk densities and the associated decrease in porosity are the result of compaction and dehydration (Fig. F11).

Unit I

Unit I is characterized by calcareous and/or siliceous clays and clayey oozes of early Pliocene to Pleistocene age. The dominant lithologies are diatom nannofossil clay and clayey nannofossil ooze. Unit I is divided into two subunits primarily on the basis of visual core description, smear slide analyses, and magnetic susceptibility; trends in NGR and color reflectance are secondary to this classification.

Subunit IA

Intervals: Core 202-1237A-1H; Core 202-1237B-1H through Section 5H-3, 102 cm; Core 202-1237C-1H through Section 5H-1, 61 cm; and Core 202-1237D-1H through Section 4H-6, 25 cm

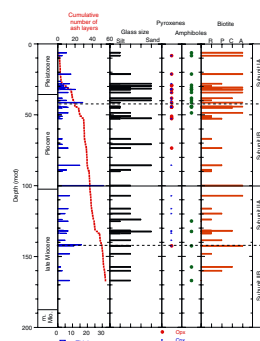
Depths: Hole 1237A: 1.00–10.95 mbsf (1.90–11.85 mcd); Hole 1237B: 0.00–38.05 mbsf (0.00–41.32 mcd); Hole 1237C: 0.00–38.41 mbsf (0.05–41.28 mcd); and Hole 1237D: 2.80–38.93 mbsf (2.30–41.35 mcd)

Age: Holocene to late Pliocene (0 to ~2 Ma)

The main components of Subunit IA are clay minerals, nannofossils, and diatoms. Changes in the relative percentages of components in smear slide samples are often subtle yet result in different lithologic classifications, such as diatom nannofossil clay, silty clayey diatom nannofossil ooze, diatom-bearing clay, and clayey diatom ooze, for almost identical lithologies within this subunit. Sediment color varies between shades of olive and olive gray. Mottling is common to abundant throughout Subunit IA. Trace fossils, often *Zoophycos* (Fig. F16), are common throughout this subunit. Infrequent black spots or smears on the cut surface contain up to 30% pyrite and minor amounts of micrite. Some pyritized burrows are observed. Trace amounts of reworked dis-coasters are also observed in the Pleistocene sediments.

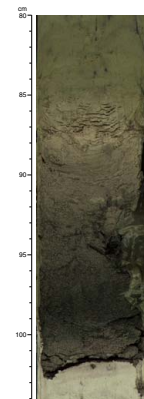
Siliciclastic content ranges from ~90% to 40% (Fig. F12). Higher values of siliciclastics are present near the top of the hole and decrease be-

F14. Ash layers, Site 1237, p. 47.

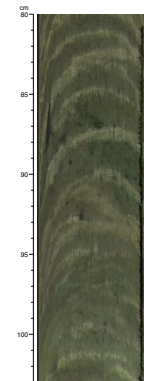


T9. Ash layers, p. 83.

F15. Ash layer at ~41.3 mcd, p. 48.



F16. Zoophycos in Subunit IA, p. 49.



low ~30 mcd. The combined sand and silt content of the siliciclastic fraction is ~10% with no downhole trend within Subunit IA. Away from discrete ash layers, the percentage of disseminated volcanic glass is generally ~10% and increases to ~60% near ash layers (e.g., at ~30 mcd). Siliceous microfossil percentages, including diatoms and sponge spicules, average ~15%, reaching maxima of >75% at ~5 and 40 mcd. Pyrite and micrite are nearly absent in the major lithologies.

Nineteen ash layers or significant ash patches are present within Subunit IA (Table T9). Twelve of them can be correlated between holes. These ash layers range between 2 and 14 cm thick with sharp basal contacts and diffuse upper contacts that grade into the dominant lithology. Ash colors range from light to dark greenish or brownish gray, dark gray, and black. Darker ash layers contain more pyrite.

Magnetic susceptibility values range between 25 and 50 instrument units in Subunit IA, with a broad minimum between 7 and 14 mcd (Fig. F11). After a sharp peak corresponding to a large ash layer just below ~20 mcd, the values decrease steadily to <25 units. NGR remains at 40–45 cps to a depth of ~30 mcd, decreasing slightly through the base of the subunit. NGR peaks mark ash layers. Bulk density, as determined from GRA and MAD measurements, increases steadily with increasing depth from ~1.2 to ~1.5 g/cm³ at the bottom of this subunit. Grain densities vary from 2.5 to 2.9 g/cm³ in Subunit IA and are, on average, lower than in the sequence below, reflecting a lower carbonate content (Fig. F11).

All sediment comprising Subunit IA is generally greenish (i.e., $a^* < 0$) (Figs. F11, F13). Downhole trends in reflectance exhibit a very slight initial decrease in a^* and b^* values (from ~0 to just below 0 and ~15 to 10, respectively), whereas L^* values steadily increase from ~40% to 50% (Fig. F11).

Subunit IB

Intervals: 202-1237B-5H-3, 102 cm, through 10H-7, 9 cm; 202-1237C-5H-1, 61 cm, through 10H-5, 127 cm; and Section 202-1237D-4H-6, 25 cm, through Core 202-1237D-7H

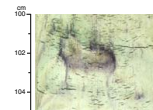
Depths: Hole 1237B: 38.05–90.67 mbsf (41.32–99.89 mcd); Hole 1237C: 38.41–92.57 mbsf (41.28–99.82 mcd); and Hole 1237D: 38.93–91.77 mbsf (41.35–99.79 mcd)

Age: late Pliocene to early Pliocene (~2–5 Ma)

The sediment of Subunit IB is light greenish gray clayey nannofossil ooze that becomes increasingly white downcore. Mottling and other evidence of bioturbation are abundant, and *Zoophycos* burrows are common. Many of the circular burrow traces are very pale brown in color and are surrounded by gray halos (Fig. F17). Below 60 mcd, faint purple and green color bands become apparent in the sediment (Fig. F18) and are more obvious as the sediment becomes lighter downcore. These colored bands exhibit no distinct lithologic difference from the major lithology.

Siliciclastics make up 40% of the sediment for most of Subunit IB (Fig. 12) but decrease significantly at the base of the subunit. Minimal amounts of sand- and silt-sized siliciclastics are present. The percentage of siliceous microfossils is ~10%, whereas calcareous microfossils represent >50% of the sediment and increase to nearly 100% near the base of the subunit. Micrite is generally present in small amounts, except near 70 and 80 mcd, where percentages of up to ~30% are reached.

F17. Trace fossil surrounded by a gray halo, p. 50.



F18. Purple and green color bands, p. 51.



Eighteen ash layers and significant ash concentrations are present in Subunit IB. Nine of them can be correlated between holes (Table T9). In general, the ash layers are ~4–5 cm thick, often display subtle changes in color, and have sharp basal contacts and gradational upper contacts. The ashes are light to dark greenish or brownish gray, dark gray, and black in color. Darker ash layers contain more pyrite. Ash is often dispersed by bioturbation, even in cases where the basal contacts are sharp.

In Subunit IB, magnetic susceptibility values are lower than in Subunit IA and decrease from <10 instrument units to almost 0 by ~65 mcd (Fig. F11). NGR exhibits a similar trend (~40 to 20 cps). NGR peaks mark the presence of ash layers. GRA and MAD bulk density values continue to increase gradually from ~1.5 to 1.65 g/cm³.

All sediment within Subunit IB is generally greenish (i.e., $a^* < 0$) (Figs. F11, F13). Increased variance in a^* and b^* compared to Subunit IA results from the green and purple color banding observed in this sediment. L^* increases from 40% to 75% down to ~65 mcd and then remains steady to the base of the subunit.

Unit II

Unit II contains early Oligocene to early Pliocene nannofossil ooze that changes abruptly from white to pale brown at ~162 mcd. Micrite abundance increases downcore. The ash layer frequency is greatest in the upper section of Unit II. Unit II is divided into two subunits based primarily on visual core description, smear slide analyses, color reflectance, and magnetic susceptibility.

Subunit IIA

Intervals: 202-1237B-10H-7, 9 cm, through 15H-5, 52 cm; 202-1237C-10H-5, 127 cm, through 15H-2, 71 cm; and 202-1237D-7H-2, 46 cm, through 8H-CC, 18 cm

Depths: Hole 1237B: 90.67–135.52 mbsf (99.89–148.11 mcd); Hole 1237C: 92.57–137.01 mbsf (99.82–148.06 mcd); and Hole 1237D: 91.77–108.29 mbsf (99.79–116.36 mcd)

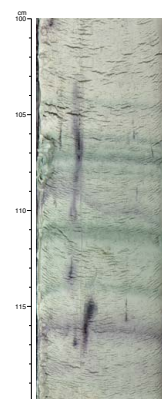
Age: early Pliocene to late Miocene (~5–8 Ma)

Subunit IIA is composed of white bioturbated and mottled nannofossil ooze with abundant green and purple color banding (Fig. F19). Evidence for bioturbation exists in the form of very pale brown and gray mottles, ash patches above and below distinct ash layers, and the abundance of dispersed ash within the dominant lithology. Sulfides are present in the form of small black spots and smears on the exposed core surface (Fig. F19).

The siliciclastic content is only 0%–5% in Subunit IIA, and no sand or silt is noted within this interval (Fig. F12). Siliceous microfossils are absent to rare, whereas calcareous microfossils amount to nearly 100%. The percentage of calcareous microfossils decreases around 135 mcd as the amount of micrite increases. Pyrite is present between 120 and 140 mcd.

Fifteen ash layers and significant ash patches are present within Subunit IIA. Eleven of them can be correlated between holes (Table T9). The thickness of these ash layers varies between <1 and 20 cm. In general, the ash layers have sharp basal contacts. Some ash layers are diffuse, exhibiting signs of bioturbation and disturbance. Ash color is light to dark greenish or brownish gray, dark gray, and black, and grades to

F19. Green and purple color banding, p. 52.



lighter colors toward the top. The upper contact grades into the major lithology. Individual ash layers are occasionally topped with a green band. X-ray diffraction (XRD) analysis shows that this greenish band is characterized by a mineral composition similar to the brownish gray basal part of the ash layer, with major amounts of clear volcanic glass, except the green band contains lesser amounts of biotite and plagioclase (Fig. F20).

Magnetic susceptibility values are ~0 for all of Subunit IIA (Fig. F11). NGR values of this subunit are characterized by a baseline around 12 cps (which is not distinguishable from background) with some variation to 30 cps, mostly from the presence of ash layers. GRA and MAD bulk density values continue to slightly increase downhole from 1.65 to 1.75 g/cm³, a trend continued from Unit I.

Reflectance measurements, a^* , b^* , and L^* , remain generally constant at a greenish color (i.e. $a^* < 0$) throughout this subunit (Figs. F11, F12, F13). Higher-frequency variations in a^* and b^* are the result of thin color bands.

Subunit IIB

Intervals: 202-1237B-15H-5, 52 cm, through 34H-CC, 29 cm; 202-1237C-15H-2, 71 cm, through 33H-CC, 25 cm; and 202-1237D-9H-1, 0 cm, through 11H-CC, 23 cm

Depths: Hole 1237B: 135.52–319.54 mbsf (148.11–360.65 mcd);
 Hole 1237C: 137.01–315.75 mbsf (148.06–354.26 mcd); and
 Hole 1237D: 224.50–253.47 mbsf (248.65–281.48 mcd)

Age: late Miocene to late Oligocene (~8–30 Ma)

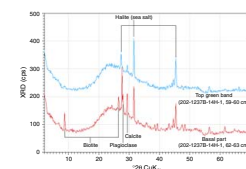
Subunit IIB is composed of nannofossil ooze with micrite. The boundary between Subunits IIA and IIB is characterized by a sharp increase in micrite content and a corresponding decrease in calcareous microfossils (Fig. F12). The pale purple and green banding observed in Subunit IIA is no longer visible. The sediment color changes abruptly from grayish white to a fairly homogeneous pale brown at ~162 mcd (Fig. F21). White mottles, often surrounded by gray halos, and occasional distinct burrows are present within the pale brown sediment, decreasing in abundance downcore. Indurated sediments, partially lithified and composed of micrite and nannofossil ooze, are present in increasing abundance downcore and are especially prevalent at the base of Holes 1237B and 1237C (Fig. F22). Shallower than 250 mcd, these indurated sediment layers are usually associated with a white color. Below this depth, they match the color of the major lithology.

Siliciclastics are minimal to absent in Subunit IIB. Minor amounts of silt to very fine sand-sized grains and volcanic glass are observed at 170–180 and ~250 mcd (Fig. F22). Calcareous microfossils and micrite each represent ~50% of the lithology. A notable increase in micrite content to nearly 100% and a proportional decrease in calcareous microfossils occurs at ~170 mcd, followed by a decrease in micrite abundance to almost 0 (and increase in calcareous microfossils). A second interval of decreased micrite content is present between ~235 and 275 mcd.

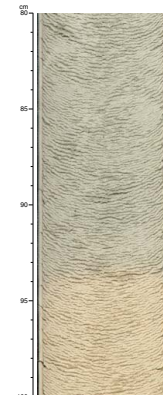
Three ash layers are present in Subunit IIB. They are light to dark brownish gray and range from 2 to 8 cm in thickness. All of them can be correlated between holes. The deepest ash layer is present at ~167 mcd (Table T9).

Magnetic susceptibility is generally low, increasing slightly between ~150 and 180 mcd, 210 and 250 mcd, and 280 and 360 mcd, apparently unrelated to changes in major lithology (Fig. F11). NGR is con-

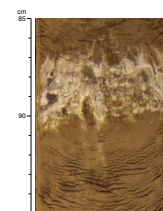
F20. XRD diffractograms of a green band and an ash layer, p. 53.



F21. Sharp color change at ~162 mcd, p. 54.



F22. Firmground in Subunit IIB, p. 55.



stant at a very low level. GRA and MAD bulk density have relatively constant values near ~1.8 g/cm³.

Subunit IIB is characterized by a reddish hue (i.e., $a^* > 0$), increased chromaticity (i.e., a^* and b^* higher than in the sediments above), and variable luminance (L^*) (Fig. F11). Within the reddish sediment, the less chromatic parts (i.e., low a^* and low b^*) are also the brightest (i.e., highest L^*). Three separate populations of reddish sediment are distinguishable in the $L^*-a^*-b^*$ color space (Fig. F13), and a different population characterizes each of the upper, middle, and lower parts of this subunit (Fig. F11).

Interpretation and Depositional History

Volcanism

A total of 55 ash layers and significant patches are present between 6 and 167 mcd. Thirty-five of them can be correlated among holes (Table T9). These ash layers primarily consist of clear silt- to sand-sized volcanic glass associated with minor amounts of plagioclase (oligoclase to labradorite), biotite, quartz, amphibole, and pyroxene (based on preliminary smear slide observations).

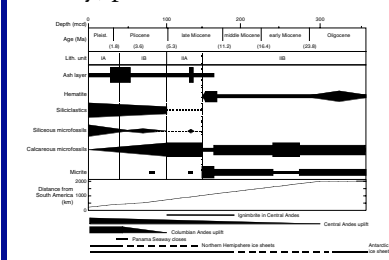
Volcanic ash deposition substantially began in the early late Miocene (~9 Ma), although minor amounts of volcanic glass are present at ~180 mcd (~11 Ma) and ~250 mcd (~17 Ma) (Fig. F12). Volcanic events, as represented by the presence of ash layers, were most frequent at ~7.5 Ma and 1–3 Ma (Fig. F14). The composition of ash layers suggests an andesitic source. Pouclet et al. (1990) reported from the nearshore sedimentary sequences (90°–14°S) collected off the coast of Peru during ODP Leg 112 that intense volcanic activity occurred between 17 and 16 Ma, 13 and 12 Ma, 10 and 8 Ma, and 5–0 Ma. In addition, ignimbrite eruption intensified in the central volcanic zone of the Andes (15° and 28°S) between 12 and 5 Ma (Gregory-Wodzicki, 2000).

Andesitic ash is nearly absent at Site 1236 (~21°S); thus, two possibilities exist for ash layer deposition beginning at ~9 Ma at Site 1237. One possibility is that Site 1237 was closer to the volcanic source than Site 1236. This is supported by the paleoposition of Site 1237 at 81°W at ~9 Ma, the same as the present position of Site 1236 (see “Introduction,” p. 1). Alternatively, zonal easterly winds able to transport volcanic materials were mostly restricted to north of Site 1236 at 21°S.

The increasing frequency of ash layer deposition at ~7.5 Ma indicates either a change in the position or intensity of zonal wind favorable for ash transport to Site 1237 or a change in the volcanic activity of the central volcanic zone of the Andes. If the southeast trades were enhanced, they would also promote intense coastal upwelling. Coincidence of maxima of siliceous fossils and organic carbon (see “Geochemistry,” p. 22) with volcanic ash layer frequency may reflect this situation (Fig. F23). Increases in siliceous microfossils and organic carbon since ~7.5 Ma could also be explained by eastward motion of the Nazca plate, bringing Site 1237 closer to the upwelling zone off Peru (Fig. F23).

On the other hand, ash layer deposition may be related to Andean uplift (Kono et al., 1986). From the late Oligocene to middle Miocene, the central Andes rose but probably did not yet impede subtropical wind circulation (Gregory-Wodzicki, 2000). The lack of an Andean barrier to subtropical wind circulation could potentially promote eolian transport into the subtropical southeast Pacific via the southeast trades. The progressive uplift is thought to have changed the direction in trade

F23. Simplified depositional history, p. 56.



winds from a more zonal flow prior to the uplift toward a more meridional flow in response to the uplift as indicated by results of modeling studies (e.g., Hay and Brock, 1992). Enhancement of the meridional flow would promote coastal upwelling and higher productivity at Site 1237, which is possibly indicated by maxima in mass accumulation rates in both carbonate and organic carbon from ~8 to 5 Ma (see “**Age Model and Mass Accumulation Rates**,” p. 25, and “**Geochemistry**,” p. 22).

Frequent ash layers between 1 and 3 Ma may suggest enhanced tectonic events. Frequent volcanic activities during this period are also reported from Sites 502 and 503 near Central America (Ledbetter, 1982), suggesting that volcanic activity could reflect regional-scale tectonic events in the eastern equatorial to south Pacific margin, possibly associated with the major uplift phase of the northern Andes during the Pliocene.

Color Reflectance–Composition Relationships

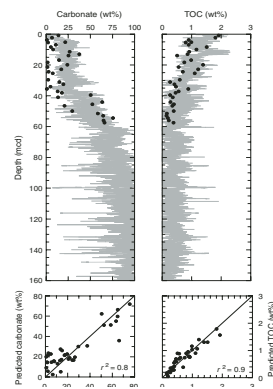
Color reflectance measurements plot in two main regions in the a^* - b^* color plane: the generally greenish sediments of Unit I and Subunit IIA group in the second quadrant, whereas the reddish sediments of the Subunit IIB cluster more tightly in the first quadrant (Fig. F13), suggesting that multiple chromophores are responsible for the general sediment color.

Preliminary predictive relationships between reflectance, carbonate, and TOC developed via a multiple linear regression reveal high correlation coefficients for carbonate ($r^2 = \sim 0.8$) and for TOC ($r^2 = \sim 0.9$) in the upper ~148 mcd of the pelagic sequence drilled at Site 1237 (Unit I and Subunit IIA) (Fig. F24). No prediction for these components was attempted in Subunit IIB, where carbonate values are close to 100 wt% and TOC contents are below shipboard detection limits. The predicted TOC exhibits strong ~8-m cycles in the first 160 mcd (spanning the last ~8 m.y. based on the shipboard age model), suggesting a ~400-k.y. cyclicity.

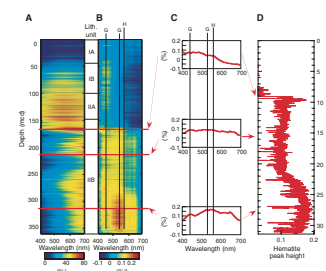
Reflectance spectra of Subunit IIB were examined to identify the chromophore(s) responsible for the pervasive red color of the sediment (Fig. F25). A sequential plot of raw spectra shows that Subunit IIB differs from those of the overlying units by exhibiting repetitive trends toward the red part of the visual domain (i.e., 600–700 nm) (Fig. F25A). First derivatives of the reflectance (Fig. F25B) show that peaks typical of goethite (i.e., ~535 nm for the principal peak and ~435 nm for the secondary peak) and hematite (i.e., ~465 nm) are present in Subunit IIB components (Fig. F25C). Q-mode factor analysis of the first derivatives confirmed that all spectra collected below 149.2 mcd are similar; therefore, the sediment contains both hematite and goethite. However, VARIMAX-rotated R-mode factor analysis failed to extract individual factors for hematite and goethite, suggesting they covary in the depth-time domain.

Extraction of a quantitative goethite estimate was precluded by the anomalously large amplitude of the secondary goethite peak, sometimes stronger than the principal peak, as well as the proximity of this secondary peak to the peak characteristic of hematite. Nevertheless, preliminary uncalibrated estimations of hematite variation using the peak height at 565 nm show stepwise increases at 163.7 and 168.3 mcd, an abrupt decrease between 169 and 171 mcd, a gradual increase be-

F24. Measured and predicted carbonate and TOC, p. 57.



F25. Derivatives of reflectance spectra, p. 58.



tween 273 and 343 mcd, and, again, a slight decrease between 343 and 360 mcd (Fig. F25D).

Eolian Input

The nearly homogeneous nannofossil ooze of Subunit IIB shows no significant lithologic variation during the late Oligocene to late Miocene. The siliciclastic fraction, mainly clay minerals, is low with little variability from 3% to 5%, whereas color variations result from changing concentrations of goethite and hematite (Fig. F25). Authigenic formation of goethite and other more disordered oxyhydroxides in marine sediments can occur in the oxic zone (e.g., Haese et al., 1998, and references therein), but dehydration of goethite to hematite is unlikely in subaqueous conditions. The iron oxyhydroxides are mobilized in the form of Fe^{2+} as the sediments experience reduction with increasing depth below the oxic zone. At Site 1237, goethite and hematite contents increase with depth, suggesting a terrigenous rather than authigenic origin (Fig. F25). Both goethite and hematite can be formed as weathering products in soils and can be transported by winds as flakes or coatings on other mineral particles. Goethite is favored over hematite in conditions of increased precipitation and/or decreasing temperature (Kampf and Schwertmann, 1983). The presence of iron oxyhydroxides implies that the sediment of Subunit IIB contains a far-field eolian component (Pye, 1987).

Today, Site 1237 lies in a zone that extends off the coasts of Peru, Ecuador, and Colombia, receiving dust transported by the southeast trade winds from the deserts of Peru and Chile (Prospero and Bonatti, 1969). Prior to the major uplift of the Andes, the trade winds probably had a more zonal distribution and the zone of eolian hematite and goethite deposition extended over both Sites 1236 and 1237. Coarse-grained material such as volcanic ash did not usually reach Site 1236 because of its southern marginal position within the trade winds belt. Iron hydroxides are detectable at Site 1237 between ~31 and ~8 Ma; however, during that time interval, siliciclastic mass accumulation rates were an order of magnitude lower than at present. These low rates, together with the fine grain size of the terrigenous component, reflect the distant position of the site relative to the continent (i.e., ~1800 to 100 km) (Fig. F23).

The persistence of iron oxyhydroxides in sediments younger than the early late Miocene at Site 1236 indicates that diagenesis is the likely cause of their abrupt disappearance at ~8 Ma at Site 1237. Dissolution of iron oxides may have occurred following an increase in the organic carbon flux around that time (see “**Age Model and Mass Accumulation Rates**,” p. 25, and “**Geochemistry**,” p. 22). A period of reducing conditions might be indicated by the presence of green and purple-black banding (Lind et al., 1993; Giosan, 2001), which is ubiquitous in the sediments above Subunit IIB. Nevertheless, the siliciclastic mass accumulation rate also increased at ~8 Ma (see “**Age Model and Mass Accumulation Rates**,” p. 25), suggesting an increased supply in the eolian dust, even though the iron hydroxide component is gone. An increase in the amount of siliciclastic materials at ~3 Ma, some yielding small amounts of reworked discoasters, possibly supplied from the Tertiary outcrops in the Peru coastal region, suggests the presence of a hemipelagic component. However, eolian dust was also a likely contributor to the siliciclastic fraction as suggested by the increase in iron oxides at Site 1236 during the late Pliocene–Pleistocene.

The presence of eolian material at Site 1237 strengthens the hypothesis put forward at Site 1236 that arid and semiarid conditions existed in subtropical South America from the late Oligocene to early Miocene. Aridity in this region could have been the result of loss of humidity by the southeast trade winds along their continental path across South America and the presence of the adjacent cool Peru-Chile Current (Frakes, 1979). Variability in the dust deposition at Site 1237 may have resulted from changes in the wind strength and/or from changes in continental aridity in the source area in response to climatic fluctuations. Hematite maxima during the late Oligocene and early late Miocene seem to coincide with Antarctic ice sheet maxima (Zachos et al., 2001, and references therein) (Fig. F23), suggesting that the aridity in the source area might have been affected by these major climatic events. Peak micrite abundance also coincides with the hematite maxima, indicating a potential linkage between the marine environment, diagenesis, and climate.

BIOSTRATIGRAPHY

Calcareous nannofossil and planktonic foraminifer biostratigraphies indicate that a complete upper Pleistocene to upper Oligocene succession was recovered at Site 1237 (Table T10; Fig. F26). Most of the standard nannofossil and planktonic foraminiferal zonal markers as well as some nonstandard nannofossil markers can be used to reconstruct the biostratigraphic succession (Fig. F38). Calcareous nannofossils at the base of the hole suggest an age younger than 31.5 Ma. Diatoms provide additional biostratigraphic control down to ~136.7 mcd.

Calcareous nannofossils and foraminifers are generally abundant or common and well to moderately well preserved throughout. Diatoms are abundant and well preserved down to ~60 mcd, but abundance decreases and preservation deteriorates below ~69 mcd, and diatoms are absent below ~174 mcd.

Marked changes in the relative proportions of benthic foraminiferal species within the Pleistocene–late Pliocene assemblage indicate variations in carbon fluxes at the seafloor that are probably related to temporal and spatial fluctuations of the coastal upwelling system and/or shifts in subsurface water masses. In contrast, the early Pliocene to late Oligocene benthic foraminiferal assemblage characterizes an oligotrophic, pelagic environment. The diatom assemblage down to 59 mcd is typical of a coastal upwelling zone on a continental margin. Below this depth, typical upwelling forms occur only occasionally with some oceanic forms.

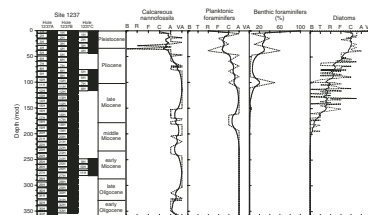
Calcareous Nannofossils

Calcareous nannofossils are generally very abundant and well to moderately preserved at Site 1237 (Table T11; Fig. F26). Most of the standard nannofossil zonal markers between late Pleistocene and late Oligocene time, as well as some nonstandard markers, have been recognized in the recovered cores. A relatively complete and detailed nannofossil biostratigraphy has been established for Site 1237. Given a similarly detailed magnetostratigraphy (see “**Paleomagnetism**,” p. 20), this site will serve as a much-needed reference in the southeast Pacific.

The mudline sample (202-1237B-1H-1, 0 cm) is barren of calcareous nannofossils, presumably because of strong dissolution of carbonate at

T10. Age-depth control points, p. 85.

F26. Calcareous nannofossils and planktonic and benthic foraminifers, p. 59.



T11. Distribution of calcareous nannofossils, p. 87.

or near the surface of sediments during the Holocene. The first occurrence (FO) of *Emiliania huxleyi* was recognized between Samples 202-1237B-1H-4, 75 cm (5.26 mcd), and 1H-CC, 9 cm (5.51 mcd), and thus, the base of the nannofossil Zone NN21 (0.26 Ma) can be drawn between these two samples. *Pseudoemiliania lacunosa* is present from Sample 202-1237B-2H-7, 40 cm (14.09 mcd), downhole, and the base of Zone NN20 (0.46 Ma), as defined by the last occurrence (LO) of this species, is placed between Samples 2H-5, 75 cm (11.43 mcd), and 2H-7, 40 cm (14.94 mcd). Additional datums have been identified in Zone NN19: *Reticulofenestra asanoi* is present from Sample 202-1237B-3H-4, 60 cm, to 3H-CC (22.74–26.1 mcd), representing the time interval 0.88 to 1.08 Ma, and *Gephyrocapsa* spp. large (>5.5 µm) is present in Sample 4H-2, 75 cm (31.06 mcd), indicating an age of 1.24–1.45 Ma for this sample. The LO of *Calcidiscus macintyrei* occurs between Samples 202-1237B-4H-1, 75 cm, and 4H-2, 75 cm (29.55–31.06 mcd), indicating an age of 1.59 Ma, the base of Zone NN19.

The Pleistocene/Pliocene boundary, coinciding with the top of Zone NN18, is placed by the FO of *Discoaster brouweri* (1.96 Ma), between Samples 202-1237B-4H-CC and 5H-1, 75 cm (38.85–38.02 mcd). The LOs of *Discoaster pentaradiatus* and *Discoaster surculus*, markers of the tops of Zones NN17 and NN18, respectively, occur between Samples 202-1237B-5H-6, 75 cm, and 5H-CC (45.57–47.29 mcd). Current sampling resolution precludes separation of the two zonal boundaries. However, the LO of *Discoaster tamalis* (2.76 Ma), between Samples 202-1237B-6H-1, 75 cm, and 6H-2, 75 cm (49.97–51.48 mcd), provides an additional marker in Zone NN16. The boundary between the upper and lower Pliocene (top of Zone NN15) corresponds to the LO of *Reticulofenestra pseudoumbilicus* (>7 µm) (3.8 Ma). This event is identified between Samples 202-1237B-8H-1, 75 cm, and 8H-2, 75 cm (68.97–70.51 mcd). Slightly deeper, between Samples 202-1237B-8H-4, 75 cm, and 8H-5, 75 cm (73.5–75.01 mcd), both the FO of *P. lacunosa* (4.0 Ma) and the LO of *Sphenolithus* spp. occur. The LO of *Sphenolithus* spp. is slightly younger in the equatorial Pacific (ODP Leg 138) according to Raffi and Flores (1995).

The top of Zone NN18 is marked by the LO of *Discoaster quinqueramus* (5.56 Ma) and is used here to approximate the Miocene/Pliocene boundary because of the scarcity of other species traditionally used to characterize this boundary, such as *Triquetrorhabdulus rugosus* or *Ceratolithus* spp. The LO of *D. quinqueramus* is identified between Samples 202-1237B-11H-4, 75 cm, and 11H-5, 75 cm (105.95 and 107.46 mcd). This species and other five-rayed discoasters were absent at Site 1236 for the age-equivalent interval, confirming an anomalous biogeographic pattern of these taxa in the southeast Pacific.

The base of Subzone NN11b (FO of *Amaurolithus primus*; 7.24 Ma) is identified between Samples 202-1237B-15H-2, 75 cm, and 15H-3, 75 cm (143.81–145.32 mcd). The base of the Subzone NN11a is inferred by the FO of *D. quinqueramus* in the interval between Samples 202-1237B-16H-CC and 17H-1, 75 cm (163.55–160.91 mcd). The interval between Samples 202-1237B-15H-1, 75 cm (142.3 mcd), and 17H-1, 75 cm (163.55 mcd), is characterized by the absence of *R. pseudoumbilicus* (>7 µm), representing a time interval from 6.8 to 8.85 Ma.

Discoaster hamatus is scarce, but some specimens are present in Sample 202-1237B-17H-6, 76 cm (171.08 mcd), allowing identification of Zone NN9. Although markers for Zones NN8 to NN6 are not present at Hole 1237B, the LO of *Coccolithus miopelagicus* (10.4 Ma), between Samples 202-1237B-18H-4, 75 cm, and 18H-5, 75 cm (178.16–179.67 mcd),

is useful to approximate the middle/late Miocene boundary. The LO of *Sphenolithus heteromorphus*, between Samples 202-1237B-20H-7, 40 cm, and 20H-CC (204.1–204.56 mcd), marks the top of Zone NN9.

In the interval corresponding with Zone NN6, other alternative events, such as the LO of *Calcidiscus premacintyrei*, the LO of *Coronocyclus nitescens*, and the FO of *T. rugosus*, provide additional and useful datums (Table T11). A significant increase in the number of specimens of *Cyclicargolithus floridanus* is observed in Sample 202-1237-19H-6, 75 cm (192.65 mcd); this event has an assigned age of ~11–13 Ma but needs to be recalibrated in this region. The FO of *S. heteromorphus* (18.2 Ma) and the LO of *Sphenolithus belemnos* (18.3 Ma) occur in the same interval, from Sample 202-1237B-23H-CC through 24H-1, 75 cm (236.82–238.6 mcd). Zone NN3 is defined by the range of *S. belemnos*, which is observed between Samples 202-1237B-24H-6, 75 cm, and 24H-7, 40 cm (246.16–247.31 mcd).

Four datums are present in the interval between Samples 202-1237B-29H-4, 75 cm, and 29H-5, 75 cm (298.88 and 300.39 mcd): the FO of *Sphenolithus disbelemnos* (base of Zone NN2) and the LOs of *Reticulofenestra bisecta* (top of Zone NN1), *Zygrhabdolithus bijugatus*, and *Sphenolithus ciperoensis* (top of NP25). This could be interpreted as a hiatus of ~1 m.y., including the Miocene/Oligocene boundary. The assemblage identified below 300.39 mcd corresponds to upper Oligocene Zone NP25. Four additional events permit higher-resolution stratigraphy in this upper Oligocene interval: the LO of *Sphenolithus distentus* (27.5 Ma), between Samples 202-1237B-31H-7, 40 cm, and 31H-CC (325.88–326.47 mcd); the LO of *Sphenolithus predistentus* (27.5 Ma), between 31H-CC and 31H-1, 75 cm (326.47–329.06 mcd); the LO of *Sphenolithus pseudoradians* (29.1 Ma); and the FO of *S. ciperoensis* (29.1 Ma), between Samples 33H-5, 75 cm, and 33H-6, 75 cm (346.64–348.15 mcd). The deepest sample (202-1237B-34H-CC; 360.60 mcd) contains *S. distentus* but no *Reticulofenestra umbilicus*, suggesting a basal age younger than 31.5 Ma at the site.

Planktonic Foraminifers

The abundance of planktonic and benthic foraminifers varies markedly in the upper part of Hole 1237B (mudline to Sample 202-1237B-4H-CC; 0–38.85 mcd). Below this depth, foraminifers are common to abundant in Hole 1237B (Table T12; Fig. F26). The percentage of benthic foraminifers relative to total foraminifers shows significant variations in the upper part of Hole 1237B (mudline to Sample 202-1237B-5H-CC; 0–47.29 mcd), reaching up to 60% in Sample 4H-CC (38.85 mcd). Sample 202-1237B-10H-CC (100.51 mcd), from an ash layer, contains a high proportion of benthic foraminifers (50%). Preservation is generally moderate or good but deteriorates in two distinct intervals (Cores 202-1237B-6H through 8H [59.23–73.38 mcd] and Cores 15H through 20H [151.21–204.56 mcd]), where planktonic foraminiferal tests show increasing evidence of dissolution and are frequently fragmented. Standard marker species are present throughout the succession and can be used to establish a relatively detailed preliminary biostratigraphy for the whole of the Pleistocene–Oligocene interval recovered at this site.

The well-preserved Pleistocene planktonic foraminiferal assemblage includes *Globigerina bulloides*, *Globigerina falconensis*, *Globigerina quinqueloba*, *Globigerinoides ruber*, *Globigerinita glutinata*, *Globorotalia scitula*, *Globorotalia tosaensis*, *Globorotalia truncatulinoides*, *Globorotalia tumida*,

T12. Distribution of planktonic foraminifers, p. 90.

Orbulina universa, *Neogloboquadrina dutertrei*, and *Sphaeroidinellina dehisces*. An age younger than 0.45 Ma can be assigned to Sample 202-1237B-1H-CC (5.51 mcd), and the overlying section, based on the presence of *Globorotalia hirsuta* (upper Pleistocene Subzone Pt1b of Berggren et al. [1995]) (Fig. F12, p. 63, in the “Explanatory Notes” chapter). The LO of *G. tosaensis* with an age of 0.65 Ma, marking the boundary between the upper and lower Pleistocene (Subzones Pt1b and Pt1a), can be placed between Samples 202-1237B-1H-CC and 2H-CC (5.51–14.62 mcd).

The LOs of *Globigerinoides extremus* (1.77 Ma) and *Neogloboquadrina acostaensis* (1.58 Ma) occur between Samples 202-1237B-2H-CC and 3H-CC (14.62–26.10 mcd). The LO of *Globorotalia puncticulata* (2.41 Ma; Zone Pl5) can be placed between Samples 202-1237B-3H-CC and 4H-CC (26.10–38.85 mcd). Two useful datums can be identified between Samples 202-1237B-5H-CC and 6H-CC (47.29–59.23 mcd), the LO of *Sphaeroidinellopsis seminula* (3.12 Ma) and the LO of *Dentoglobigerina altispira* (3.09 Ma), which define the base of upper Pliocene Zones Pl4 and Pl5, respectively. The FO of *Sphaeroidinella dehiscens* (3.25 Ma) occurs between Samples 202-1237B-6H-CC and 7H-CC (59.23–68.37 mcd). The LO of *Globorotalia plesiotumida* (3.77 Ma) can be placed between Samples 202-1237B-7H-CC and 8H-CC (68.37–78.38 mcd). The LO of *Globoturborotalia nepenthes* (4.20 Ma), between Samples 202-1237B-8H-CC and 9H-CC (78.38–89.23 mcd), characterizes the base of lower Pliocene Zone Pl2. The FO of *G. tumida*, between Samples 202-1237B-10H-CC and 11H-CC (100.51–110.77 mcd), indicates an age younger than 5.82 Ma, but shipboard sampling resolution does not define the Pliocene/Miocene boundary with precision.

The FO of *Globorotalia margaritae* (6.09 Ma), which indicates the upper part of upper Miocene Zone M13, occurs between Samples 202-1237B-11H-CC and 12H-CC (110.77–120.58 mcd). Other useful markers for Zone M13 are the FOs of *Globigerinoides conglobatus* (6.20 Ma) and *Pulleniatina primalis* (6.40 Ma), between Samples 202-1237B-12H-CC and 13H-CC (120.58–130.80 mcd), the FO of *Globorotalia conomiozea* (7.12 Ma), between Samples 13H-CC and 14H-CC (130.80–141.15 mcd), and the FO of *G. plesiotumida* (8.58 Ma), between Samples 15H-CC and 16H-CC (151.21–160.91 mcd). The FO of *N. acostaensis* (9.82 Ma), between Samples 1237B-17H-1, 98–99 cm, and 17H-CC (163.79–172.80 mcd), corresponds to the base of Zone M13.

The FO of *G. nepenthes* (11.19 Ma), between Samples 202-1237B-18H-CC and 19H-CC (182.62–194.16 mcd), defines the base of middle Miocene Zone M11. The LO of *Globorotalia foehsi* s.l. (11.68 Ma), between Samples 202-1237B-18H-CC and 19H-CC (182.62–194.16 mcd), and the FO of *G. foehsi* s.l. (13.42 Ma), between Samples 19H-CC and 20H-CC (194.16–204.56 mcd), allow identification of the middle Miocene Zone M9.

The LO of *Globorotalia archeomenardii* (14.2 Ma), between Samples 202-1237B-19H-CC and 20H-CC (94.16–204.56 mcd), indicates Zone M7. Another useful marker for Zone M7 is the LO of *Globorotalia peripheronora* (14.6 Ma), between Samples 202-1237B-20H-CC and 21H-CC (204.56–214.99 mcd). The FO of *Globorotalia peripheroacuta* (14.8 Ma), between Samples 202-1237B-21H-CC and 22H-CC (214.99–225.79 mcd), marks the base of Zone M7.

The FO of *Globorotalia praemenardii* (14.9 Ma), indicating Zone M6, can be placed between Samples 202-1237B-21H-CC and 22H-CC (214.99–225.79 mcd). The FO of *Globigerinoides diminutus* (16.1 Ma), between Samples 202-1237B-22H-CC and 23H-CC (225.79–236.82 mcd),

the LO of *Globorotalia miozea* (15.9 Ma), between Samples 21H-CC and 22H-CC (214.99–225.79 mcd), and the FO of *Globorotalia birnagaea* (16.7 Ma), between Samples 23H-CC and 24H-CC (236.82–247.52 mcd), all indicate Zone M5.

The LOs of *Globorotalia semivera* (17.3 Ma) and *Catapsydrax dissimilis* (17.3 Ma), between Samples 202-1237B-23H-CC and 24H-CC (236.82–247.52 mcd), are useful markers for lower Miocene Zone M3. The LO of *Globoquadrina binaensis* (19.1 Ma) occurs between Samples 202-1237B-24H-CC and 25H-CC (247.52–259.48 mcd). The LO of *Globoturborotalia angulisutularis* (21.6 Ma) can be placed between Samples 202-1237B-25H-CC and 26H-CC (259.48–269.13 mcd). Other useful datums for the early Miocene are the FOs of *G. binaensis* (22.1 Ma) and *Globoquadrina dehiscens* (23.2 Ma), between Samples 202-1237B-27H-CC and 28H-CC (281.26–291.54 mcd), and the FO of *Globigerinoides trilobus* (23.4 Ma), between Samples 28H-CC and 29H-CC (291.54–303.56 mcd).

The Miocene/Oligocene boundary is located in Core 202-1237B-29H but could not be determined with precision because of low-resolution shipboard sampling. The FO of *Globigerinoides primordius* common (24.3 Ma), between Samples 202-1237B-29H-CC and 30H-CC (303.56–314.85 mcd), and the FO of *G. primordius* (26.7 Ma), between Samples 30H-CC and 31H-CC (314.85–326.47 mcd), indicate upper Oligocene Zone P22. The FO of *G. angulisutularis* (29.4 Ma), between Samples 202-1237B-31H-CC and 32H-CC (326.47–338.35 mcd), marks the base of Zone P21. The LO of *Subbotina angiporoides* (30 Ma) and the LO of *Turborotalia ampliapertura*, (30.30 Ma), which corresponds to the base of Zone P20, both occur between Samples 202-1237B-32H-CC and 33H-CC (338.35–349.95 mcd).

Benthic Foraminifers

The abundance of benthic foraminifers varies markedly in Hole 1237B. The higher proportion of benthic foraminifers in the upper part of the hole (mudline to Sample 202-1237B-5H-CC; 0–47.29 mcd) probably reflects the location of the site within an upwelling zone. Below this depth, the proportion of benthic foraminifers decreases significantly (except for Sample 202-1237B-10H-CC, from an ash layer; 100.51 mcd), and a marked change in assemblage composition occurs, which indicates changing food resources (Fig. F26). Preservation is generally good to moderate throughout. To evaluate assemblage composition and variability downhole, ~200 specimens from the >150- μ m fraction were picked from the mudline and selected core catcher samples (Samples 202-1237B-1H-CC through 12H-CC [5.51–120.58 mcd], 21H [214.99 mcd], and 33H [349.95 mcd]) and counted. A total of 59 taxa were identified (Table T13).

The Pleistocene–late Pliocene assemblage in Cores 202-1237B-1H through 5H (5.51–47.29 mcd) is relatively diverse. However, the proportion of high carbon-flux indicators, such as *Globobulimina affinis*, *Globobulimina pyrula*, *Uvigerina peregrina*, and, in particular, *Epistominella exigua* (a species that rapidly exploits pulsed phytodetritus inputs (cf. Smart et al., 1994; Gooday, 1996), varies markedly. These variations in assemblage composition point to marked changes in carbon flux at the seafloor, probably related to fluctuations in upwelling regime. The Pliocene–Miocene assemblage below Core 202-1237B-5H (47.29 mcd), which generally reflects a lower food supply, is characterized by *Chrysalogonium* spp., *Cibicidoides mundulus*, *Globocassidulina subglobosa*, *Gyroidinoides soldanii*, *Gyroidinoides orbicularis*, *Laticarinina pauperata*, *Melonis*

T13. Distribution of benthic foraminifers, p. 92.

affinis, *Oridorsalis umbonatus*, *Planulina wuellerstorfi*, *Pullenia bulloides*, *Pyrgo murrhina*, *Rectuvigerina striata*, *Siphonina tenuicarinata*, *Stilostomella abyssorum*, *Stilostomella subspinosa*, and *Vulvulina spinosa*.

Diatoms

Acid-cleaned slides of all core catcher samples from Hole 1237B were analyzed, as well as smear slides of some additional layers from the split cores. Most samples from Core 202-1237B-1H through 18H (166.9 mcd) contain diatoms (Table T14) even though preservation and abundance decrease below Core 202-1237A-7H (68.4 mcd). Diatoms are absent from Core 202-1237A-19H (194.2 mcd) to the bottom of the hole (360.6 mcd). Preservation of diatoms varies from good to poor.

The Holocene diatom assemblage is characterized by the dominance of coastal upwelling taxa, such as *Thalassionema nitzschioides* and resting spores of the genus *Chaetoceros*, the common occurrence of large *Coscinodiscus* (*Coscinodiscus gigas* and *Coscinodiscus oculus-iridus*), and the presence of neritic and benthic species such as *Actinocyclus senarius*, *Paralia sulcata*, and *Cocconeis* spp. The Pleistocene diatom assemblage consists of a mixture of oceanic (e.g., *Azpeitia nodulifera*, *Rhizosolenia* spp., *Pseudoeunotia doliolus*, *Nitzschia fossilis*, *Nitzschia reinholdii*, and *Hemidiscus cuneiformis*) and nearshore coastal upwelling forms.

The presence of neritic and benthic diatoms and Miocene taxa (*Crucicula* spp., *Denticulopsis* spp., and *Thalassiosira plicata*) indicates reworking of nearshore sediment material to this site. An indication supported also by the observed increase in clay content (see “[Lithostratigraphy](#),” p. 6). Displaced shallow-water benthic and freshwater diatoms are found irregularly down to Core 202-1237B-8H (78.4 mcd) but more consistently between Cores 1H and 3H (0–26.1 mcd).

A noticeable change in diatom assemblage occurs in Sample 202-1237B-7H-2, 40 cm (60.5 mcd), below which the typical coastal upwelling forms are intermittently present.

The Pliocene diatom assemblage is characterized by heavily silicified diatoms, such as *Thalassiosira convexa*, *Nitzschia jouseae*, and *Stephanopyxis* spp.

Late Miocene diatoms are rare, and assemblages are characterized by the presence of *Azpeitia nodulifera*, *Thalassiothrix* spp., and *T. nitzschioides*. The species *Nitzschia marina*, *N. fossilis*, *N. miocenica*, *N. cylindrica*, *N. porteri*, *T. convexa*, and *Rhizosolenia barboi* are observed occasionally when diatom abundance increases.

On the basis of primary zonal markers and/or secondary markers, it is possible to identify the following diatom zones:

1. The base of the *Fragilariopsis doliolus* Zone is defined by the FO of this species (2.00 Ma), between Sample 202-1237B-4H-5, 40 cm, and 4H-3, 40 cm (32.2–35.3 mcd). The presence of *Rhizosolenia matuyamai* in Samples 202-1237B-3H-5, 75 cm, and 3H-CC (22.9–26.1 mcd) places these samples within 1.05–1.18 Ma. However, the sporadic and rare presence of zonal boundary index species, such as *N. reinholdii* and *Rhizosolenia praebergonii* var. *robusta*, in the Quaternary section prevents a more detailed zonal assessment. The zonal boundary of the *F. doliolus/N. reinholdii* Zones, defined by the last continuous occurrence of *N. fossilis*, is tentatively placed between Samples 202-1237B-3H-1, 75 cm, and 3H-3, 75 cm (16.9–19.9 mcd).

T14. Distribution of diatoms,
p. 94.

2. The absence of *F. doliolus* and *N. jouseae* in Samples 202-1237B-4H-1, 22 cm, and 6H-1, 75 cm (29.2–49.9 mcd), places this interval into the *Nitzschia marina* Zone (2.00–2.77 Ma). Subzone division is not possible because of the scarcity of *T. convexa*.
3. The presence of *N. jouseae* in Samples 202-1237B-6H-2, 22 cm, and 9H-CC (50.9–89.2 mcd) places these samples into the *N. jouseae* Zone (2.77–5.12 Ma). The presence of *R. paebergonii* s.l. within the upper portion of this zone, above Sample 202-1237B-7H-1, 110 cm (59.6 mcd), suggests that the top part of this interval is younger than the FO of *R. paebergonii* (i.e., <3.17 Ma).
4. The oldest identifiable diatom zone in Hole 1237B is the *Nitzschia miocenica* Zone (6.57–7.30 Ma), which is defined by the concurrent presence of *N. miocenica* and absence of *T. convexa* in Samples 202-1237B-13H-CC and 14H-4, 95 cm (130.8–136.7 mcd).

Below these samples, no age-diagnostic diatom species are observed, but diatoms are found again in Core 202-1237B-19H, where a mono-specific *Stephanopyxis* spp. assemblage and abundant girdle bands are present in Sample 202-1237B-19H-1, 3 cm (184.4 mcd). The presence of the late Miocene–Pliocene species *N. marina* and *N. reinholdii* and the lack of middle Miocene diatom species within this sample suggests contamination. The late Quaternary diatom assemblage found in the surrounding olive-colored sediments (Sample 202-1237B-19H-1, 5 cm) also points to downhole contamination. No such level was found in the corresponding cores at Hole 1237C.

Abundant girdle bands are also observed within the late Pliocene *N. marina* Zone. Fragments of *Hemiaulus* spp. were found in Sample 202-1237B-6H-5, 70 cm (50.2 mcd) and are considered to be reworked from Eocene and Oligocene sediments.

PALEOMAGNETISM

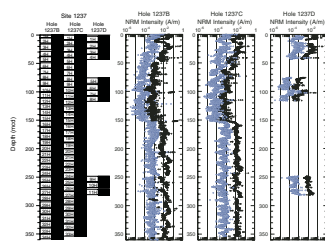
Natural Remanent Magnetization

The natural remanent magnetization (NRM) of the archive half of each core section was initially measured then remeasured after alternating-field (AF) demagnetization at selected levels. Hole 1237A sections were AF demagnetized at 10, 15, 20, and 25 mT. Sections from Holes 1237B, 1237C, and 1237D were demagnetized at 20 and 25 mT. Sections obviously affected by drilling disturbance were not measured.

The NRM intensity before and after demagnetization shows the same general downhole trend with about 1.5 orders of magnitude less intensity after 25-mT AF demagnetization than before (Fig. F27). NRM intensities after AF demagnetization are in the 10^{-3} A/m range at the top of each hole. These intensities decrease by an order of magnitude through the upper 60 mcd, below which values range from $\sim 3 \times 10^{-4}$ to low as 1×10^{-5} A/m. At ~ 150 mcd, just below the transition from lithologic Subunit IIA to IIB (see “[Lithostratigraphy](#),” p. 6), intensity increases by an order of magnitude over just a few meters. NRM intensities from ~ 150 mcd to the base of the cored section are consistently within the middle 10^{-4} to low 10^{-3} A/m range (Fig. F27). The overall trend in NRM intensity is similar in pattern to the magnetic susceptibility profile.

Steep positive inclinations observed prior to demagnetization and resulting from the drill string magnetic overprint are mostly removed af-

F27. NRM intensity before and after AF demagnetization, p. 60.



ter 25-mT AF demagnetization. If unremoved, these would hamper polarity interpretations, as they are of the same sign as reversed polarity. The resulting downhole inclination pattern for Holes 1237C, 1237B, and 1237D shows clear alternations of negative and positive inclinations throughout (Fig. F28).

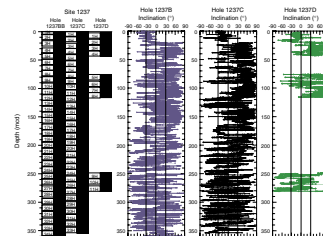
For the upper 100 mcd, the inclination pattern can be correlated between Holes 1237B and 1237C and with the overlapping part of Hole 1237D (Fig. F28). Clear interpretation of polarity chronos and subchrons, based on inclination, can be made to the base of the Gilbert Chron 3n (5.32 Ma). The Matuyama (2r)/Brunhes (1n) boundary, as well as the boundaries of the Jaramillo (1r.1n) Subchron, Olduvai (2n) Chron, and the Reunion (2r.1n) Subchron are all clearly identifiable in at least one and often two holes. The Gauss (2An)/Matuyama (2r) boundary is found in Hole 1237C, and the Kaena (2An.1r) and Mammoth (2An.2r) Subchrons are observed in Hole 1237B. The subchrons of the Gilbert (Cochiti, 3n.1n; Nunivak, 3n.2n; Sidufjall, 3n.3n; and Thvera, 3n.4n) are easily identifiable in Hole 1237B cores and in the overlapping cores of Hole 1237D, which were cored using the nonmagnetic barrel. The normal polarity Cochiti and Thvera Subchrons are not observed in Hole 1237C, where the mcd equivalent depths (Cores 202–1237C-8H and 10H) were cored with the normal steel (magnetic) core barrel. These cores have steeper than expected positive inclinations that suggest these normal polarity subchrons may have been overprinted by the core barrel's magnetization (Fig. F29). The interpretation of the magnetic stratigraphy for the interval 0–100 mcd and the resulting correlation to the geomagnetic polarity timescale (GPTS) (Cande and Kent, 1995) (Fig. F29; Tables T15, T16) produce age estimates that are consistent with the biostratigraphic datums (see “[Biostratigraphy](#),” p. 14) and significantly augment the shipboard age models (see “[Age Model and Mass Accumulation Rates](#),” p. 25).

From 100 to ~160 mcd, the correlation of the inclination pattern between holes, the interpretation of the magnetic stratigraphy from these, and its correlation to the GPTS are less clear (Fig. F30). Normal (negative) polarities are likely present but not clearly recorded. The combined effects of low NRM intensities (Fig. F27), drilling overprints, and intermittent reducing conditions in these sediments are probably at least partially responsible. To reduce the noise in this part of the record, we stacked and smoothed (10-point running mean) the inclination data from Holes 1237B, 1237C, and 1237D based on the mcd scale (Fig. F30). This procedure is similar to that used at Site 1236 (see “[Paleomagnetism](#),” p. 15, in the “Site 1236” chapter; also see Fig. F29).

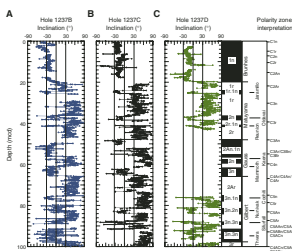
The stacked record allows an interpretation of the polarity to be made (Fig. F30; Table T16) that, when correlated to the GPTS (Cande and Kent 1995), provides ages consistent with the biostratigraphic datums (see “[Biostratigraphy](#),” p. 14). Below ~160 mcd, the increase in NRM intensity (Fig. F27) also results in a clearly defined inclination pattern that is correlative from Hole 1237B to 1237C (Fig. F30). The polarity within this interval is easily interpreted and correlated to the GPTS. The predominant normal polarity interval between ~175 and 181 mcd is correlated to Chron 5n. Not only are the polarity chronos identifiable, but a consistent pattern of polarity transitions is observed between Chron 4r (~162 mcd) and Chron 5Ar (~199 mcd). All polarity chronos and subchrons are identifiable within this interval (Table T15), providing exceptional stratigraphic control (Table T16).

Below 200 mcd the inclination data are not obviously correlative between Holes 1237B and 1237C (Fig. F31). Therefore caution must be

F28. NRM inclination after demagnetization, p. 61.



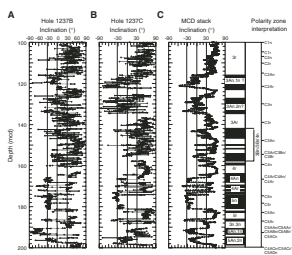
F29. NRM Inclination after demagnetization, upper 100 mcd, p. 62.



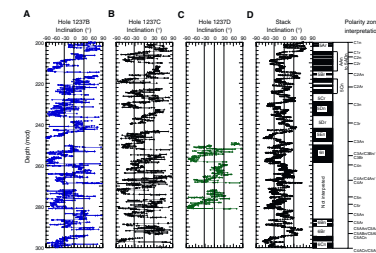
T15. Determination of polarity chron boundaries, p. 98.

T16. Paleomagnetic age control points, p. 100.

F30. Inclination after demagnetization, 100–200 mcd, p. 63.



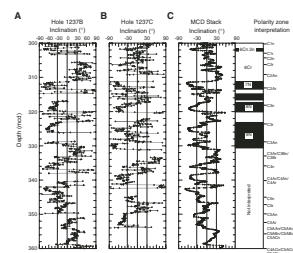
F31. Inclination after demagnetization, 200–300 mcd, p. 64.



employed with any polarity interpretation made. An interpretation is made based on the stacked inclination record (Fig. F31) that is generally consistent with the biostratigraphic datums (see “**Biostratigraphy**,” p. 14) down to a depth of ~250 mcd. However, within this interval, alternative interpretations are possible and the placement of polarity boundaries is equivocal. From ~250 to 280 mcd, the inclination records between Holes 1237B and 1237C are discrepant. The stacked record does not result in a record that resembles the GPTS within the interval as defined by the biostratigraphic datums. It is possible that a reevaluation of the mcd scale may be required. Inclination data for Holes 1237B and 1237D are similar on the mcd scale, whereas data from Hole 1237C are not, further suggesting that the composite depth correlation between Holes 1237B, 1237C, and 1237D may need reevaluation.

Below ~280 mcd, inclination can be correlated between Holes 1237B and 1237C, and the stacked record can be used for polarity interpretation to ~330 mcd, which is suggested to be the base of Chron 9n (27.972 Ma) (Fig. F32). Shore-based work will allow significant refinement of these interpretations. Much of the ambiguity could result from the low level of AF demagnetization used, which has not fully removed the drill string overprint, especially in intervals where the steel core barrel was used.

F32. Inclination after demagnetization, 300–360 mcd, p. 65.

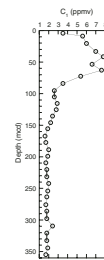


GEOCHEMISTRY

Sediment Gases

Concentrations of headspace gases were routinely monitored in Hole 1237B sediments according to shipboard safety and pollution prevention considerations. Little gas was found at Site 1237 (Fig. F33; Table T17). Very low amounts of methane were detected in the shallowest headspace gas sample at 4.5 mcd. Below this depth, methane gradually increased, reaching a maximum of ≥ 7 ppmv between 33.3 and 63.1 mcd. Then methane concentrations decreased to concentrations near the laboratory air concentrations (~2–3 ppmv at 95.3 mcd) and remained at this level to the bottom of the hole. The interval where methane is detected corresponds to the interval where significant concentrations of organic matter were measured (see “**Sedimentary Inorganic Carbon, Organic Carbon, and Nitrogen Concentrations**,” p. 24). At depths ≥ 95 mcd, both methane and organic carbon are near detection limits. Methane probably originates from in situ fermentation (methanogenesis) of the organic matter buried in the sediments (Claypool and Kvenvolden, 1983). In addition, the low amounts of methane together with the high organic matter contents suggest that only a small amount of organic material is converted to gas. No higher molecular weight hydrocarbons were detected.

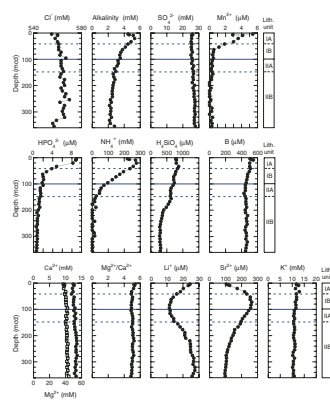
F33. Headspace methane vs. depth, p. 66.



T17. Headspace methane concentrations, p. 101.

T18. Interstitial water geochemical data, p. 102.

F34. Interstitial water geochemical data, p. 67.



Interstitial Water Geochemistry

We collected 35 interstitial water samples from Site 1237, 1 from Hole 1237A and 34 from Hole 1237B. These are treated as constituting a single mcd profile. Chemical gradients at this site (Table T18; Fig. F34) reflect minor influence in the uppermost sediments of organic matter diagenesis by microbially mediated oxidation reactions, a limited degree of biogenic opal dissolution, and a minor signature of calcite diagenesis. For many elements, interstitial water geochemistry does not

vary with lithologic unit (see “[Description of Lithologic Units](#),” p. 7, in “Lithostratigraphy”) or with the significant color change observed at ~170 mcd (Fig. [F34](#)).

Chlorinity generally increases with depth to 566 mM at 320.9 mcd, with slightly lower values in the deepest three samples (Fig. [F34](#)). Salinity, measured refractively as total dissolved solids, ranges from 34 to 36 (Table [T18](#)). Sodium concentrations measured by inductively coupled plasma–atomic emission spectrophotometry averaged 2% lower than those estimated by charge balance reported here (Table [T18](#)). Sodium concentrations parallel chlorinity, with a total range from 482 to 490 mM.

Organic matter diagenesis, driven by microbial oxidation reactions, has a relatively minor influence on interstitial water composition. Sulfate undergoes a limited degree of reduction primarily in the uppermost sediments, by no more than 4 mM from typical seawater values of ~29 mM. Alkalinity has a shallow maximum of >5 mM from 9.1 to 20.6 mcd, declines to <3.5 mM by the Unit I/II boundary, and then declines more slowly to ~2.2 mM from 332.7 to 344.3 mcd.

Dissolved manganese decreases rapidly from 5.4 µM at 4.5 mcd to low values in Subunit IB and persists at low values (near or below the detection limit of 0.1 µM) throughout the drilled interval. The marked color change at ~170 mcd has no corresponding signature in manganese redox chemistry in interstitial water. Dissolved iron is generally below the detection limit (<1.1 µM), reflecting the low content of terrigenous material in this site.

Phosphate concentrations decrease steeply in Subunit IA and more slowly in Subunit IB, from 8.9 µM at 4.5 mcd to <2 µM throughout Unit II. Ammonium concentrations increase from 220 µM at 4.5 mcd to peak values >250 µM from 9.1 to 33.3 mcd, then decline in Subunits IB and IIA to values near or below the detection limit (11 µM) in Subunit IIB. The shallow peaks in alkalinity, manganese, phosphate, and ammonium, along with minor sulfate reduction, result from degradation of organic matter in the upper ~100 mcd.

Dissolved silicate has highest values in the depth range where diatoms are reported to have the best preservation and abundance (see “[Diatoms](#),” p. 19, in “Biostratigraphy”), averaging ~800 µM from 4.5 to 63.0 mcd. Silicate concentrations decline to 543 µM at 177.3 mcd and average 325 µM in the depth interval observed to be barren of diatoms (≥ 194.2 mcd). The interstitial waters are undersaturated with respect to biogenic opal (saturation value = >1000 µM). Barium concentrations are below the detection limit (<0.03 µM) throughout. Boron concentrations, initially greater than seawater concentrations, decrease with increasing depth, from >500 µM from 4.5 to 41.8 mcd to 450 µM at 355.0 mcd.

Calcium and magnesium concentrations increase slightly with increasing depth, with a larger relative increase in calcium resulting in decreasing magnesium/calcium ratios with depth from 5.3 at 4.5 mcd to 4.8 at 355.0 mcd (Fig. [F34](#)). Authigenic mineralization reactions have a limited influence on interstitial water geochemistry at this site, with no signatures of intense calcite precipitation or dolomite formation. Lithium concentrations decrease from 24 µM at 4.5 mcd to a broad minimum of <14 µM from 63.0 to 125.5 mcd, then increase again with depth to 26–27 µM from 275.9 to 355.0 mcd. Strontium concentrations are greater than seawater values in the shallowest samples, increasing to a maximum of >200 µM from 33.3 to 135.7 mcd. The strontium profile is similar in character, although with a smaller maximum value, to

those in calcium carbonate-rich, equatorial sites, with the strontium maximum resulting from the recrystallization of biogenic calcite to authigenic calcite (e.g., Delaney et al., 1991). Potassium concentrations decrease slightly with depth (Fig. F34).

Sedimentary Inorganic Carbon, Organic Carbon, and Nitrogen Concentrations

Inorganic carbon (IC), total carbon (TC), and total nitrogen (TN) concentrations were determined on sediment samples from Hole 1237B (Table T19). Organic matter carbon/nitrogen ratios and Rock-Eval pyrolysis were employed to characterize the organic matter.

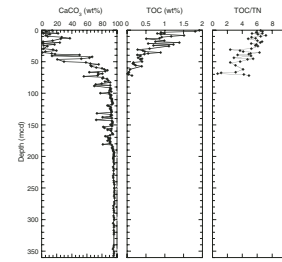
Calcium carbonate concentrations range between 0.9 and 96.9 wt% (Table T19; Fig. F35). In samples from the uppermost 38 mcd, calcium carbonate contents are low, averaging 12.2 wt%, and vary between 1.0 and 37.6 wt%. Between 38 and ~80 mcd, calcium carbonate contents increase to ~90 wt%. From ~80 to 182 mcd, calcium carbonate contents vary between 70 and 96 wt%. Some intervals with lower calcium carbonate are likely due to the presence of volcanic ash (see “[Description of Lithologic Units](#),” p. 7, in “[Lithostratigraphy](#)”). From ~182 to 357 mcd, calcium carbonate contents are consistently >94 wt% (average = 95.7 wt%). A significant change in calcium carbonate characterizes the interval from 38 to 80 mcd and may reflect the combined influence of the tectonic backtrack path of the site toward more coastal conditions with a greater delivery of terrigenous material and biogenic silicate (opal) to the site (see Fig. F12).

TOC contents range between 0.3 and 1.9 wt% in the uppermost 38 mcd and from 0.4 wt% to below detection limit at greater depth (Table T19; Fig. F35). The two uppermost samples show the highest values. The TOC profile shows a gradual and long-term decrease from the top to values <0.1 wt% by 59.3 mcd, associated with large-amplitude variations of ~1 wt%, especially in the uppermost 40 mcd. Variations in TOC and calcium carbonate contents cannot be attributed to dilution alone, as the relationship between TOC and calcium carbonate is not linear (Fig. F36). Besides, these variations cannot be explained by a dissolution effect of carbonate resulting from organic matter degradation since microfossils are generally well preserved (see “[Biostratigraphy](#),” p. 14). The change in TOC concentrations is most likely the result of greater biological production resulting from enhanced nutrient supply via upwelling of nutrient-rich waters. This would be consistent with the tectonic backtrack path exposing Site 1237 to more coastal conditions during the last 5 m.y. In addition, the role of the Andean uplift by forcing coastal winds to blow parallel to the coastline may have been one of the forcing parameters allowing the establishment and/or the intensification of the coastal upwelling during this period. At greater depths, in the sediments where calcium carbonate contents are very high, total organic carbon content could not be determined with confidence by shipboard techniques and is probably <0.1–0.2 wt% (Romankevitch, 1984).

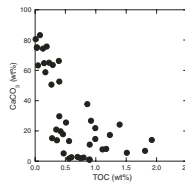
In order to characterize the organic matter in the sediments and to explain its steep gradient with depth, TOC/TN ratios and Rock-Eval results were used. Site 1237 TOC/TN ratios vary from 7 to <2 (Table T19; Fig. F35). The TOC/TN ratios average 4.9, a value which is typical of unaltered algal material (5–8) (Bordovskiy, 1965; Emerson and Hedges, 1988; Meyers, 1997). The TOC and TOC/TN changes are most likely driven by the change in the supply of terrigenous organic matter.

T19. IC, CaCO_3 , TC, TOC, and TN concentrations, and TOC/TN ratios, p. 103.

F35. Calcium carbonate, TOC, and TOC/TN vs. depth, p. 68.



F36. TOC vs. CaCO_3 , p. 69.



Ten samples that span the interval of the downhole decrease in TOC concentrations in the uppermost 26 mcd were selected for Rock-Eval measurements (Table T20). The low T_{max} values indicate that organic matter is thermally immature. The relationship between S_2 and TOC (Fig. F37) shows that the organic matter is between Type II (i.e., marine algal organic matter) and Type III (i.e., land-derived organic matter) (Tissot and Welte, 1984; Langford and Blanc-Valleron, 1990). This is not consistent with TOC/TN ratios that indicate that the organic matter is of marine origin. Fresh marine plankton has a relatively high lipid content and thus high H/C ratios. Therefore, well-preserved organic matter of marine algal origin yields high hydrogen index (HI) values when subjected to pyrolysis. The HI values measured in these samples, which range from 114 to 227 (Table T16), indicate that the organic matter is significantly degraded. A subtle change in the supply of land-derived organic matter cannot explain alone the HI and TOC/TN values. Therefore, one reason for the downhole decrease in TOC contents, together with TOC/TN ratios and HI values, could be an increase in the degradation of the organic matter with burial time. Another reason could be a downhole decrease in the preservation of the organic matter buried in the sediments because of a decrease in export productivity in the past. Such a change in export productivity is also suggested by a parallel change in diatom, benthic foraminifer, and organic matter abundance (see “**Biostratigraphy**,” p. 14). This downhole change toward more eutrophic conditions would be consistent with the tectonic backtrack path of the site and may be consistent with the establishment or intensification of coastal upwelling due to Andean uplift.

AGE MODEL AND MASS ACCUMULATION RATES

A 360.6-mcd-thick (317.4 mbsf) Oligocene (~31 Ma) to Holocene pelagic sediment sequence was recovered at Site 1237. Biostratigraphic and magnetostratigraphic datums (see Tables T10, T16) were used to construct of an age-depth model for this site (Table T21; Fig. F38). Linear sedimentation rates (LSRs), total mass accumulation rates (MARs), and carbonate MARs were calculated at 1-m.y. intervals (see “**Age Models and Mass Accumulation Rates**,” p. 41, in the “Explanatory Notes” chapter).

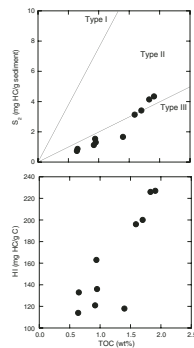
Age-Depth Model

Both biostratigraphic and magnetic reversal datums are well constrained and in general agreement for the upper 200 mcd (Fig. F38). Here, the age-depth model relies primarily on paleomagnetic data. Below 200 mcd (~12 Ma), the agreement between biostratigraphic datums becomes less certain, presumably because biostratigraphic datums are no longer astronomically tuned, and magnetic data are no longer available. For the interval deeper than 200 mcd, we relied primarily (although not exclusively) upon calcareous nannofossil datums to define the age-depth model. Had we chosen to emphasize the planktonic foraminifer datums, a significantly different age model would have resulted for this interval.

Determining the age-depth trend was particularly difficult from ~250 to 300 mcd, where few nannofossil datums exist. At ~300 mcd, calcareous nannofossil biostratigraphy (see “**Biostratigraphy**,” p. 14) indicates the potential presence of a 1-m.y. hiatus, an event not noted in the

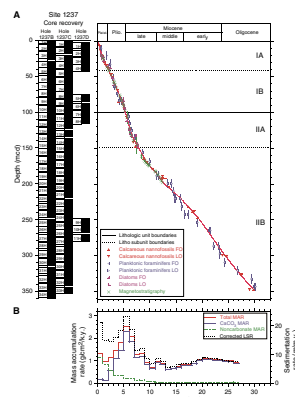
T20. Results of Rock-Eval pyrolysis, p. 106.

F37. S_2 vs. TOC and HI vs. TOC, p. 70.



T21. Age-depth model, LSRs, and MARs, p. 107.

F38. Biostratigraphic and magnetostratigraphic datums and age-depth model, p. 71.



other microfossil groups or in lithologic or physical properties data. A straight line was therefore fit for this interval. The presence of a hiatus at this depth would slightly steepen the curves above and below this interval, and result in slightly higher LSRs and MARs.

Linear Sedimentation and Mass Accumulation Rates

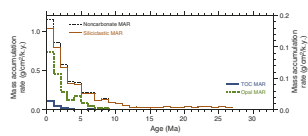
LSRs range between ~5 and 23 m/m.y., and total MARs range from ~0.6 to 2.4 g/cm²/k.y. LSRs, total MARs, and carbonate MARs are low before 8 Ma, rise to their peaks at 5–6 Ma, and decline from 5 to 2 Ma. All rates have closely similar trends from 30 to ~15 Ma. Relatively constant LSR and MAR values in this interval result from the smooth age model chosen because the coarse time resolution and large uncertainties of the biostratigraphic datums did not allow a more detailed definition. Significant fluctuations might have occurred in reality.

From 15 Ma to the present, the LSR, total MAR, and carbonate MAR trends diverge. The divergence of carbonate MAR from total MAR reflects continually increasing amounts of noncarbonate components during a period of increasing carbonate MAR (15–5 Ma) as well as the subsequent period of declining carbonate MAR (5–1 Ma). Diatoms are absent below 195 mcd (>12 Ma), and abundance increases from barren to common at ages <9 Ma (<170 mcd) (Fig. F26). Siliciclastic material increases from ~5% to ~80% at ages <12 Ma (<190 mcd), and TOC increases from 0 to ~2% after 3 Ma (<60 mcd) (Fig. F35). The gradually increasing divergence of LSR from MARs at ages <15 Ma can be explained by changing mineral proportions and sediment fabric (more opal and clay and less carbonate), decreasing overburden, and the associated increase in porosity and decrease in dry density. The interval of slightly elevated rates from 13 to 11 Ma might represent effects of the middle Miocene climatic changes, but the present age model is too simplistic to yield detailed interpretations.

Peak carbonate MARs in the interval 5–7 Ma likely represent enhanced productivity of calcareous organisms, because a similar peak in carbonate MAR is present within the records of other Leg 202 sites (see Figs. F20, p. 95, and F34, p. 109, in the “Leg 202 Summary” chapter) as well as elsewhere in the equatorial Pacific (Farrell et al., 1995; Pisias et al., 1995), where it is interpreted as a production signal. The substantial reduction in carbonate MAR from 5 Ma to the present is not associated with visual evidence for dissolution of calcareous microfossils (see “[Biostratigraphy](#),” p. 14) and is interpreted as primarily related to a decrease in the productivity of calcareous organisms.

A general increase in the accumulation of both biogenic and terrigenous components toward the younger portion of the record would be expected as a result of the gradual tectonic drift of Site 1237 toward South America. This backtrack path shows that Site 1237 moved out of the oligotrophic subtropical gyre close to the highly productive coastal upwelling regions of Peru (see “[Introduction](#),” p. 1) and into the dust distribution areas of the northern Chile deserts (see “[Lithostratigraphy](#),” p. 6). The general increases in biogenic opal after 15 Ma, increase in terrigenous input after ~5 Ma, and the abundance of TOC and a further increase of opal after 3 Ma (Fig. F39) are therefore most likely the result of increasing proximity to South America. However, regional oceanographic changes that are expressed as a so-called “opal shift” in the equatorial Pacific (Farrell et al., 1995) may also be expressed at Site 1237.

F39. Noncarbonate MARs and the three major components, p. 72.



REFERENCES

- Barker, P.F., and Burrell, J., 1977. The opening of the Drake Passage. *Mar. Geol.*, 25:15–34.
- Behrenfeld, M.J., Randerson, J.T., McClain, C.R., Feldman, G.C., Los, S.O., Tucker, C.J., Falkowski, P.G., Field, C.B., Frouin, R., Esaias, W.E., Kolber, D.D., and Pollack, N.H., 2001. Biospheric primary production during and ENSO transition. *Science*, 291:2594–2597.
- Berggren, W.A., Kent, D.V., Swisher, C.C., III, and Aubry, M.-P., 1995. A revised Cenozoic geochronology and chronostratigraphy. In Berggren, W.A., Kent, D.V., Aubry, M.-P., and Hardenbol, J. (Eds.), *Geochronology, Time Scales and Global Stratigraphic Correlation*. Spec. Publ.—SEPM, 54:129–212.
- Bordovskiy, O.K., 1965. Accumulation and transformation of organic substances in marine sediment, 2. Sources of organic matter in marine basins. *Mar. Geol.*, 3:5–31.
- Cande, S.C., and Haxby, W.F., 1991. Eocene propagating rifts in the southwest Pacific and their conjugate features on the Nazca plate. *J. Geophys. Res.*, 96:19609–19622.
- Cande, S.C., and Kent, D.V., 1995. Revised calibration of the geomagnetic polarity timescale for the Late Cretaceous and Cenozoic. *J. Geophys. Res.*, 100:6093–6095.
- Claypool, G.E., and Kvenvolden, K.A., 1983. Methane and other hydrocarbon gases in marine sediment. *Annu. Rev. Earth Planet. Sci.*, 11:299–327.
- Delaney, M.L., and Shipboard Scientific Party, 1991. Inorganic geochemistry summary. In Kroenke, L.W., Berger, W.H., Janecek, T.R., et al., *Proc. ODP, Init. Repts.*, 130: College Station, TX (Ocean Drilling Program), 549–551.
- Duncan, R.A., and Hargraves, R.B., 1984. Plate tectonic evolution of the Caribbean region in the mantle reference frame. In Bonini, W.E., Hargraves, R.B., and Shagam, R. (Eds.), *The Caribbean-South American Plate Boundary and Regional Tectonics*. Mem.—Geol. Soc. Am., 162:81–94.
- Emerson, S., and Hedges, J.I., 1988. Processes controlling the organic carbon content of open ocean sediments. *Paleoceanography*, 3:621–634.
- Farrell, J.W., Raffi, I., Janecek, T.C., Murray, D.W., Levitan, M., Dadey, K.A., Emeis, K.-C., Lyle, M., Flores, J.-A., and Hovan, S., 1995. Late Neogene sedimentation patterns in the eastern equatorial Pacific. In Pisias, N.G., Mayer, L.A., Janecek, T.R., Palmer-Julson, A., and van Andel, T.H. (Eds.), *Proc. ODP, Sci. Results*, 138: College Station, TX (Ocean Drilling Program), 717–756.
- Frakes, L.A., 1979. *Climate Throughout Geological Time*: New York (Elsevier).
- Giosan, L., 2001. The use of sediment color in paleoceanography: Pliocene–Pleistocene sedimentation in the western North Atlantic [Ph.D. dissert.]. State Univ. of New York, Stony Brook.
- Gooday, A.J., 1996. Epifaunal and shallow infaunal foraminiferal communities at three abyssal NE Atlantic sites subject to differing phytodetritus input regimes. *Deep-Sea Res.*, 43:1395–1421.
- Gregory-Wodzicki, K.M., 2000. Uplift history of the central and northern Andes: a review. *Geol. Soc. Am. Bull.*, 112:1091–1105.
- Haese, R.R., Peteremann, H., Dittert, L., and Schulz, H.D., 1998. The early diagenesis of iron in pelagic sediments: a multidisciplinary approach. *Earth Planet. Sci. Lett.*, 157:233–248.
- Haug, G.H., and Tiedemann, R., 1998. Effect of the formation of the Isthmus of Panama on Atlantic Ocean thermohaline circulation. *Nature*, 393:673–676.
- Hay, W.W., and Brock, J.C., 1992. Temporal variation in intensity of upwelling off southwest Africa. In Summerhayes, C.P., Prell, W.L., and Emeis, K.C. (Eds.), *Upwelling Systems: Evolution Since the Early Miocene*. Spec. Publ.—Geol. Soc. London, 64:463–497.
- Kampf, N., and Schwertmann, U., 1983. Goethite and hematite in a climo-sequence in southern Brazil and their application in classification of kaolinitic soils. *Geoderma*, 29:27–39.

- Kono, M., Fukao, Y., and Yamamoto, A., 1986. Mountain building in the central Andes (in Japanese with English abstract). In Kono, M., *Report of the Geophysical Studies of the Central Andes (Second Phase)*: Tokyo (Tokyo Inst. Tech.), 125–136.
- Langford, F.F., and Blanc-Valleron, M.M., 1990. Interpreting Rock-Eval pyrolysis data using graphs of pyrolyzable hydrocarbons vs. total organic carbon. *AAPG Bull.*, 74:799–804.
- Ledbetter, M.T., 1982. Tephrochronology at Sites 502 and 503. In Prell, W., Gardner, J.V., et al., *Init. Rept. DSDP*, 68: Washington (U.S. Govt. Printing Office), 403–408.
- Lind, I.L., Janecek, T.R., Krissek, L.A., Prentice, M.L., and Stax, R., 1993. Color bands in Ontong Java Plateau carbonate oozes and chalks. In Berger, W.H., Kroenke, L.W., Mayer, L.A., et al., *Proc. ODP, Sci. Results*, 130: College Station, TX (Ocean Drilling Program), 453–470.
- Lonsdale, P., 1976. Abyssal circulation of the southeastern Pacific and some geological implications. *J. Geophys. Res.*, 81:1163–1176.
- Meyers, P.A., 1997. Organic geochemical proxies of paleoceanographic, paleolimnologic, and paleoclimatic processes. *Org. Geochem.*, 27:213–250.
- Mix, A.C., Pisias, N.G., Goldfinger, C., West, B., Mayer, L.A., and Bloomer, S.F., 1997. *Southeast Pacific Paleoceanographic Transects, Site Survey Data Package 2: Genesis Leg III, R/V Roger Revelle, Feb.–Apr. 1997*: Corvallis (Oregon State Univ.)
- Ocean Climate Laboratory, 1999. *World Ocean Atlas 1998 (WOA98)* [CD-ROM]. Available from: National Climatic Data Center, Asheville NC 28801-5001, USA.
- Pisias, N.G., Mayer, L.A., and Mix, A.C., 1995. Paleoceanography of the eastern equatorial Pacific during the Neogene: synthesis of Leg 138 drilling results. In Pisias, N.G., Mayer, L.A., Janecek, T.R., Palmer-Julson, A., and van Andel, T.H. (Eds.), *Proc. ODP, Sci. Results*, 138: College Station, TX (Ocean Drilling Program), 5–21.
- Pouclet, A., Cambray, H., Cadet, J.-P., Bourgois, J., and De Wever, P., 1990. Volcanic ash from Leg 112 off Peru. In Suess, E., von Huene, R., et al., *Proc. ODP, Sci. Results*, 112: College Station, TX (Ocean Drilling Program), 465–480.
- Prospero, J.M., and Bonatti, E., 1969. Continental dust in the atmosphere of the eastern equatorial Pacific. *J. Geophys. Res.*, 74:3362–3371.
- Pye, K., 1987. *Aeolian Dust and Dust Deposits*: London (Academic Press).
- Raffi, I., and Flores, J.-A., 1995. Pleistocene through Miocene calcareous nannofossils from eastern equatorial Pacific Ocean. In Pisias, N.G., Mayer, L.A., Janecek, T.R., Palmer-Julson, A., and van Andel, T.H. (Eds.), *Proc. ODP, Sci. Results*, 138: College Station, TX (Ocean Drilling Program), 233–286.
- Romankevich, E.A., 1984. *Geochemistry of Organic Matter in the Ocean*: New York (Springer-Verlag).
- Smart, C.W., King, S.C., Gooday, A.J., Murray, J.W., and Thomas, E., 1994. A benthic foraminiferal proxy of pulsed organic matter paleofluxes. *Mar. Micropaleontol.*, 23:89–99.
- Strub, P.T., Mesias, J.M., Montecino, V., Rutllant, J., and Salinas, S., 1998. Coastal ocean circulation off western South America. In Robinson, A.R., and Brink, K.H. (Eds.), *The Sea* (Vol. 11): *Coastal Oceans*: New York (Wiley), 273–313.
- Tissot, B.P., and Welte, D.H., 1984. *Petroleum Formation and Occurrence* (2nd ed.): Heidelberg (Springer-Verlag).
- Tsuchiya, M., and Talley, L.D., 1998. A Pacific hydrographic section at 88°W: water-property distribution. *J. Geophys. Res.*, 103:12899–12918.
- Zachos, J.C., Pagani, M., Sloan, L., Thomas, E., and Billups, K., 2001. Trends, rhythms, and aberrations in global climate 65 Ma to present. *Science*, 292:686–693.

Figure F1. A. Locations of Sites 1236 and 1237 and bathymetry. B. Site locations and oceanographic features off Peru and northern Chile (CC = Coastal Current, PCCC = Peru-Chile Countercurrent, PCC = Peru-Chile Current), after Strub et al. (1998). Modern mean annual sea-surface temperatures (SSTs) (contours are in degrees Celsius, after Ocean Climate Laboratory, 1999).

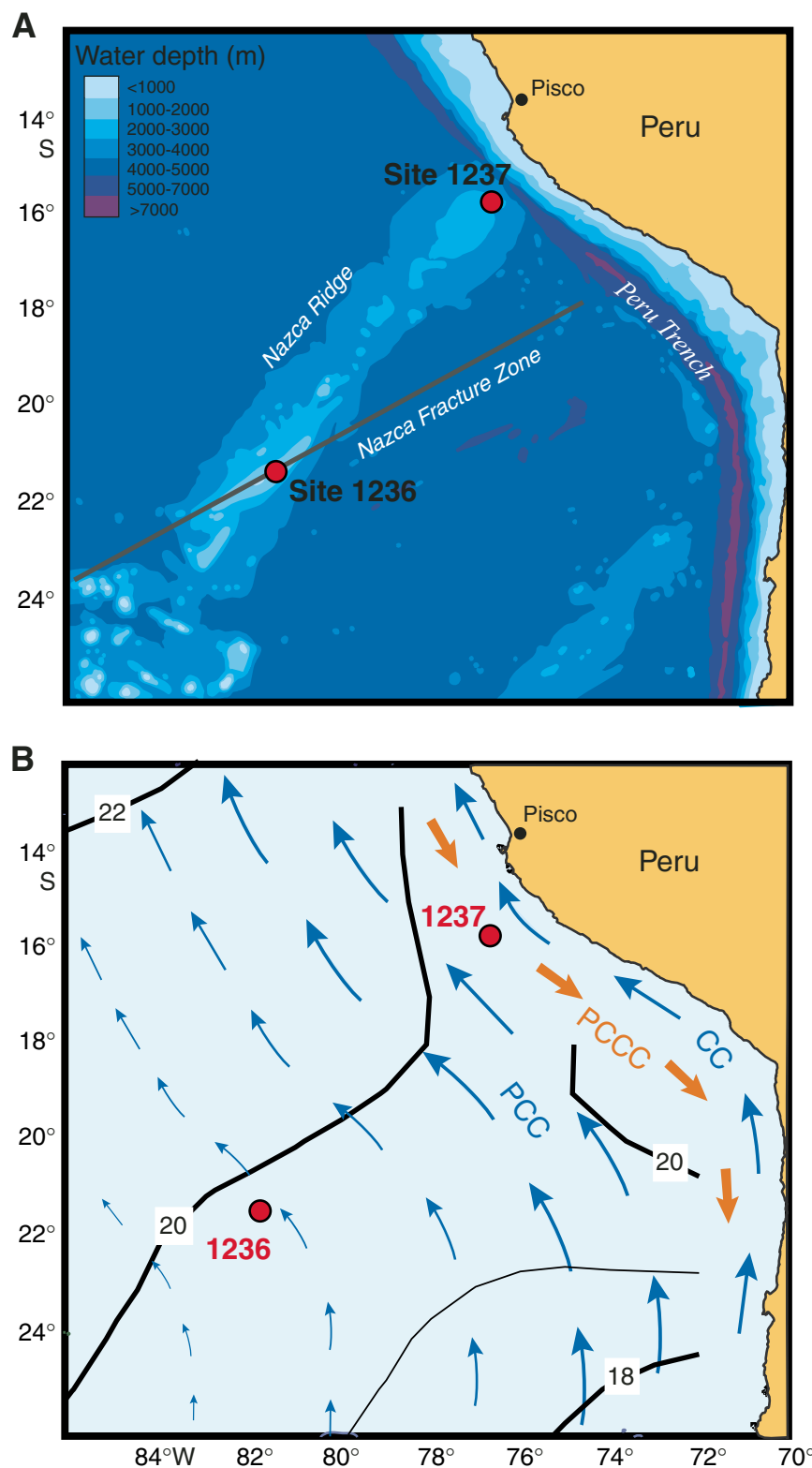


Figure F2. High-resolution swath bathymetry at Site 1237 (Mix et al., 1997).

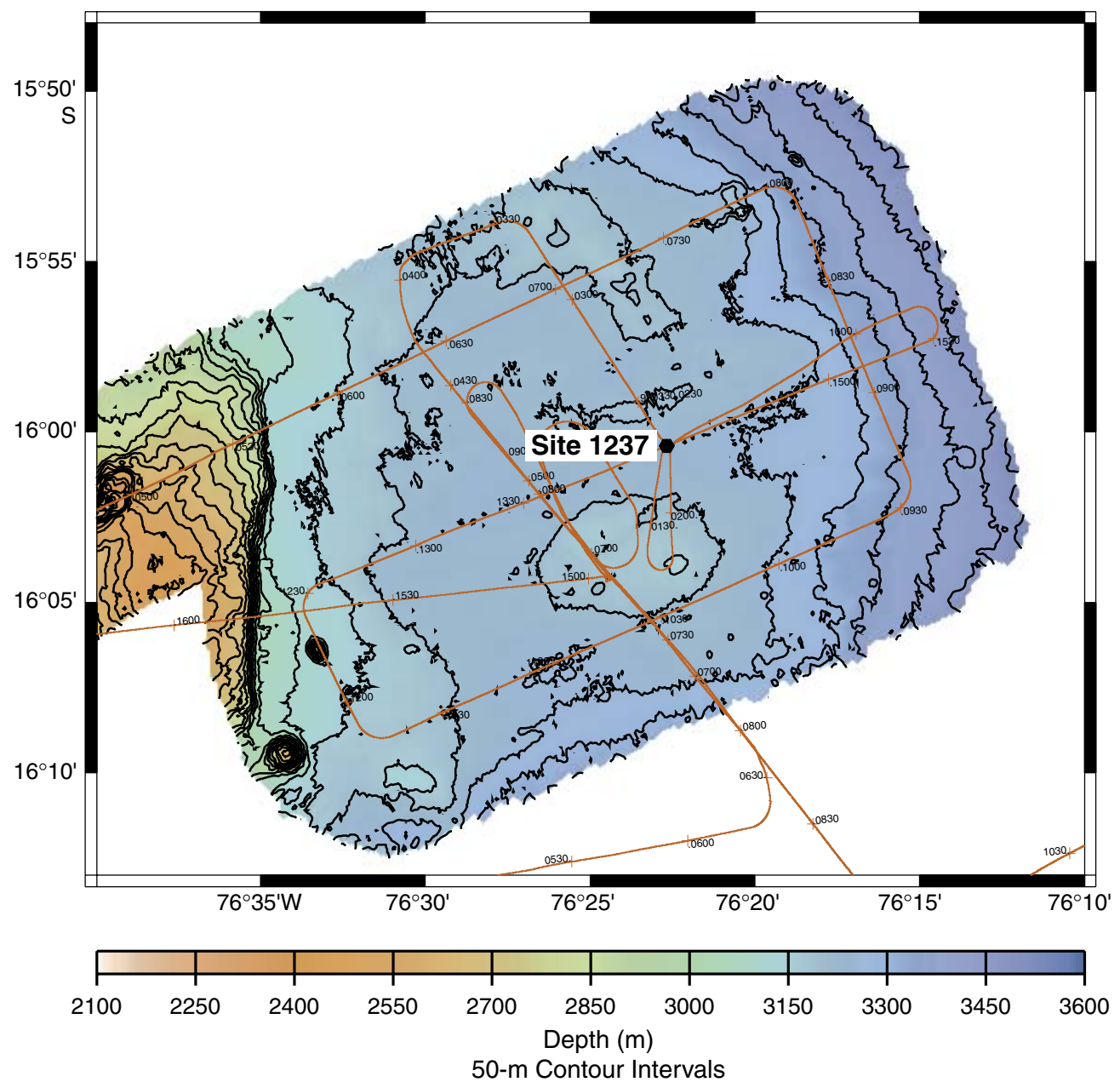


Figure F3. Seismic profile at Site 1237 (line 970329, *Revelle*, NAZ-3B-4, Shotpoint 589, 1412z, 80-in³ water gun at 30–400 Hz, notch filter at 60 Hz; Mix et al., 1997).

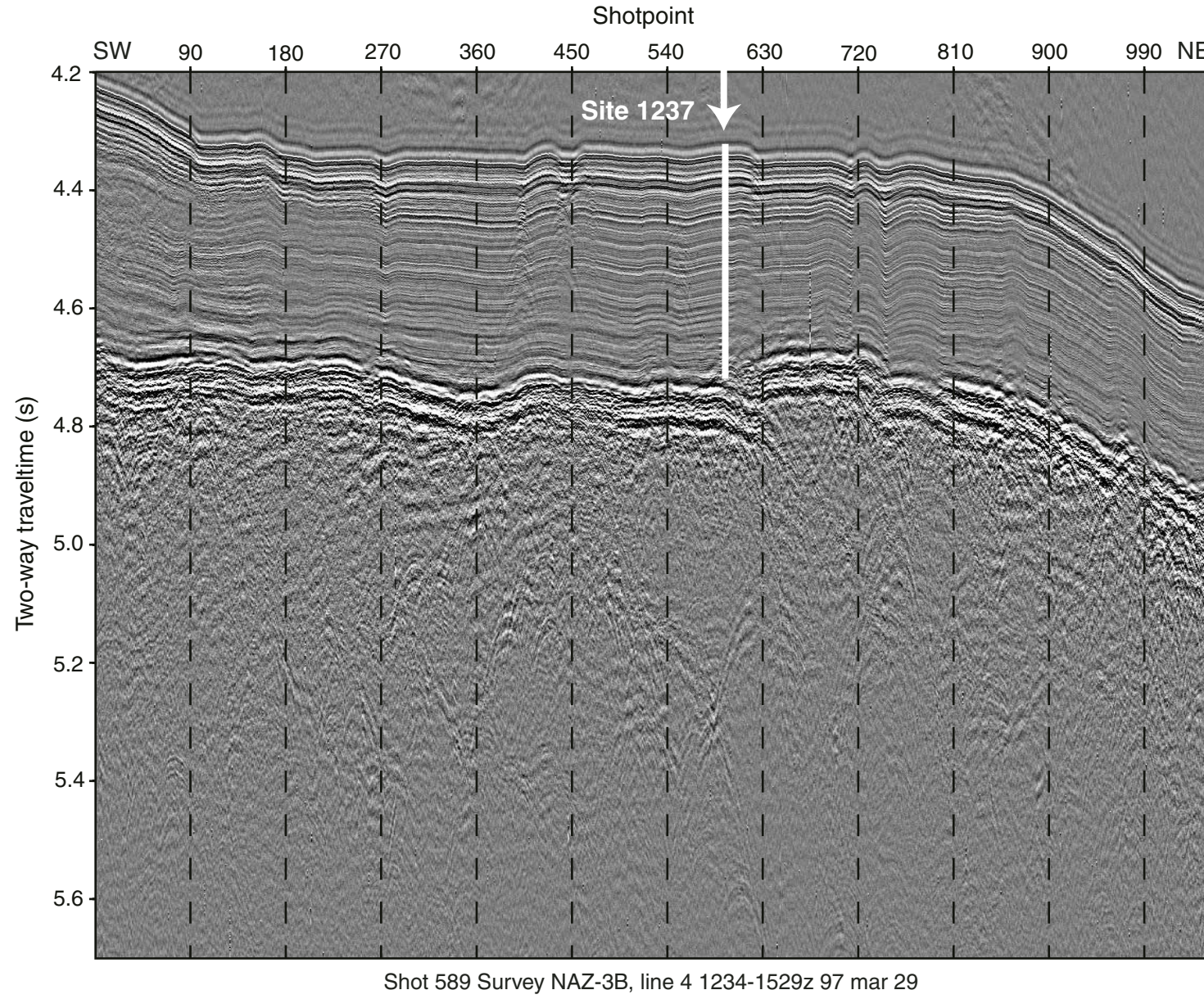


Figure F4. Tectonic backtrack of Site 1237, relative to a fixed South America. Poles of rotation are from Duncan and Hargraves (1984) and Pisias et al. (1995). The dotted path represents positions in million-year increments. Numbers note ages (in millions of years) of changes in rate or direction of drift. Contours of modern mean annual sea-surface temperature are superimposed. PCC = Peru-Chile Current, SEC = South Equatorial Current).

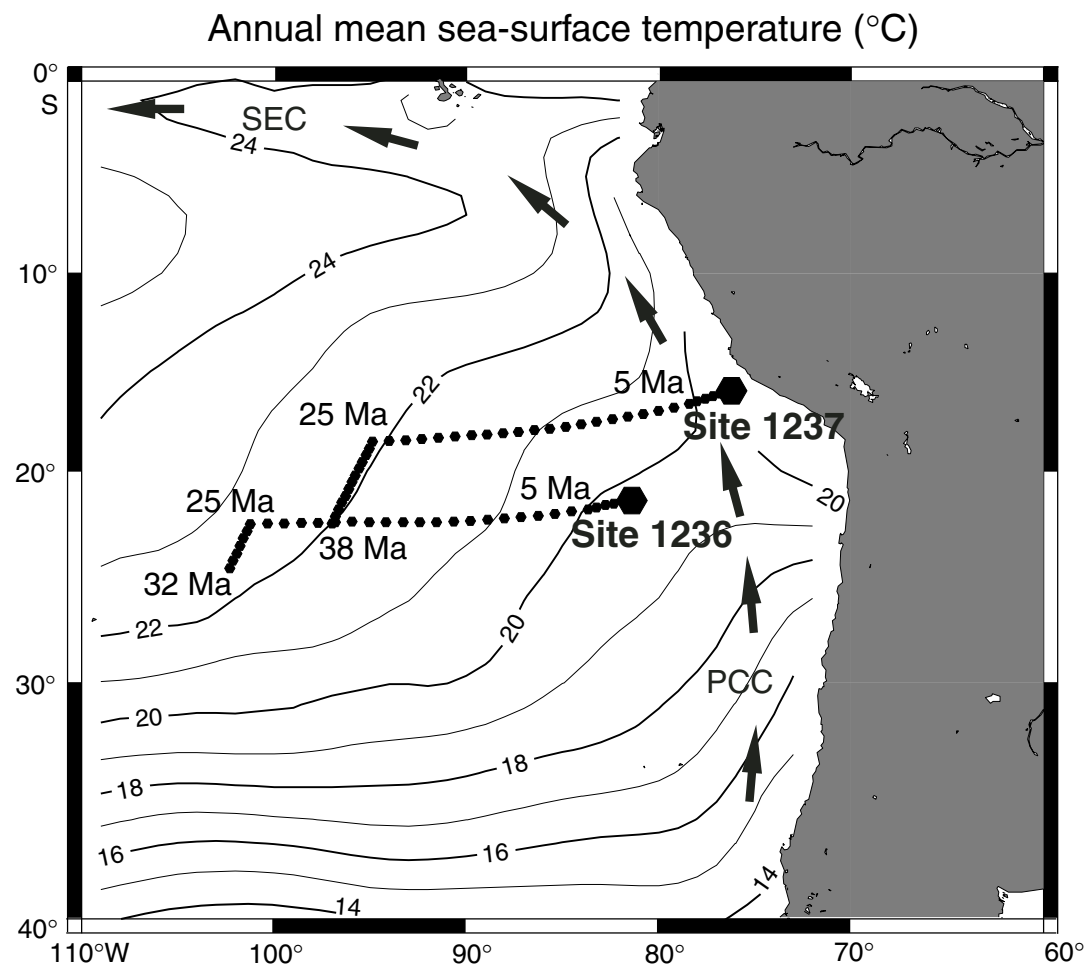


Figure F5. Chlorophyll distributions in surface waters of the southeast Pacific, based on satellite color data, reveal that Site 1237 is now near the edge of the highly productive upwelling systems of the Peru margin.

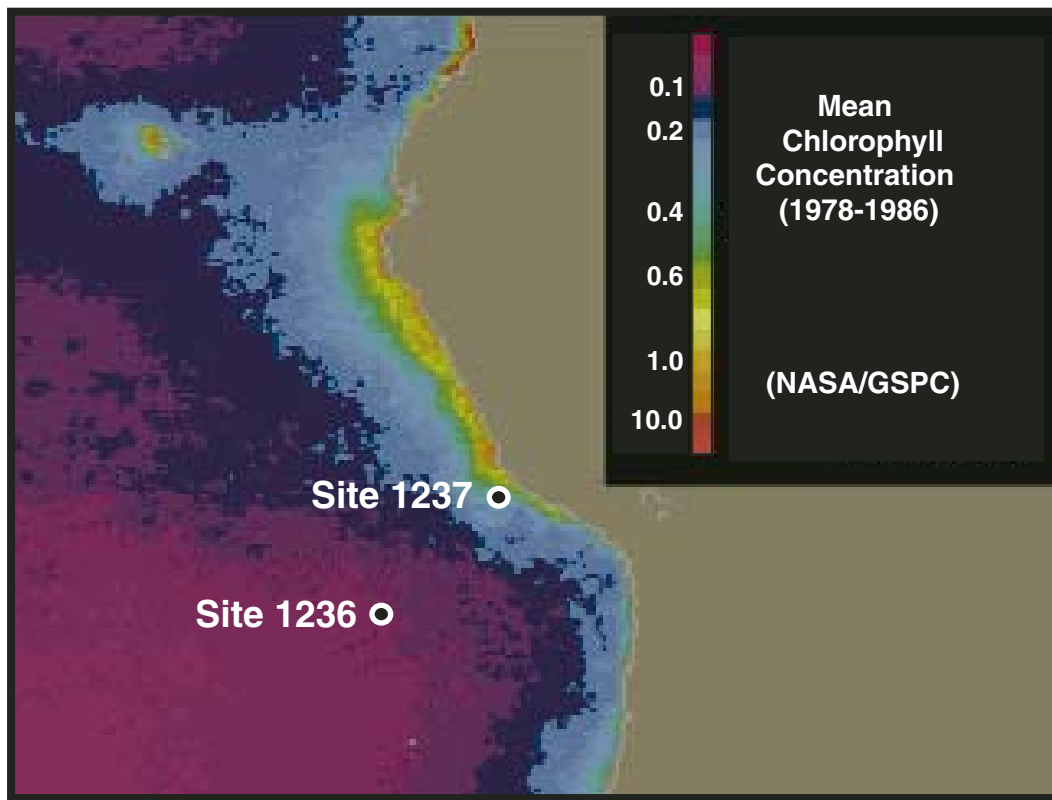


Figure F6. Modern annual-average properties of the upper ocean at paleolocations of Site 1237, based on plate tectonic backtracking and an assumption of no temporal changes in regional oceanic properties. Atlas data on physical and chemical properties are from WOA98 (Ocean Climate Laboratory, 1999). Primary productivity (PP) is from satellite measurements of sea-surface color (Behrenfeld et al., 2001). Pycnocline depth is calculated to the nearest 5 m, based on the shallowest maximum in the vertical density gradient. Symbols are average values extracted from the nearest 1° latitude-longitude box in each atlas. Lines = smoothed trends of each property along the backtrack path. SST = sea-surface temperature, SSS = sea-surface salinity.

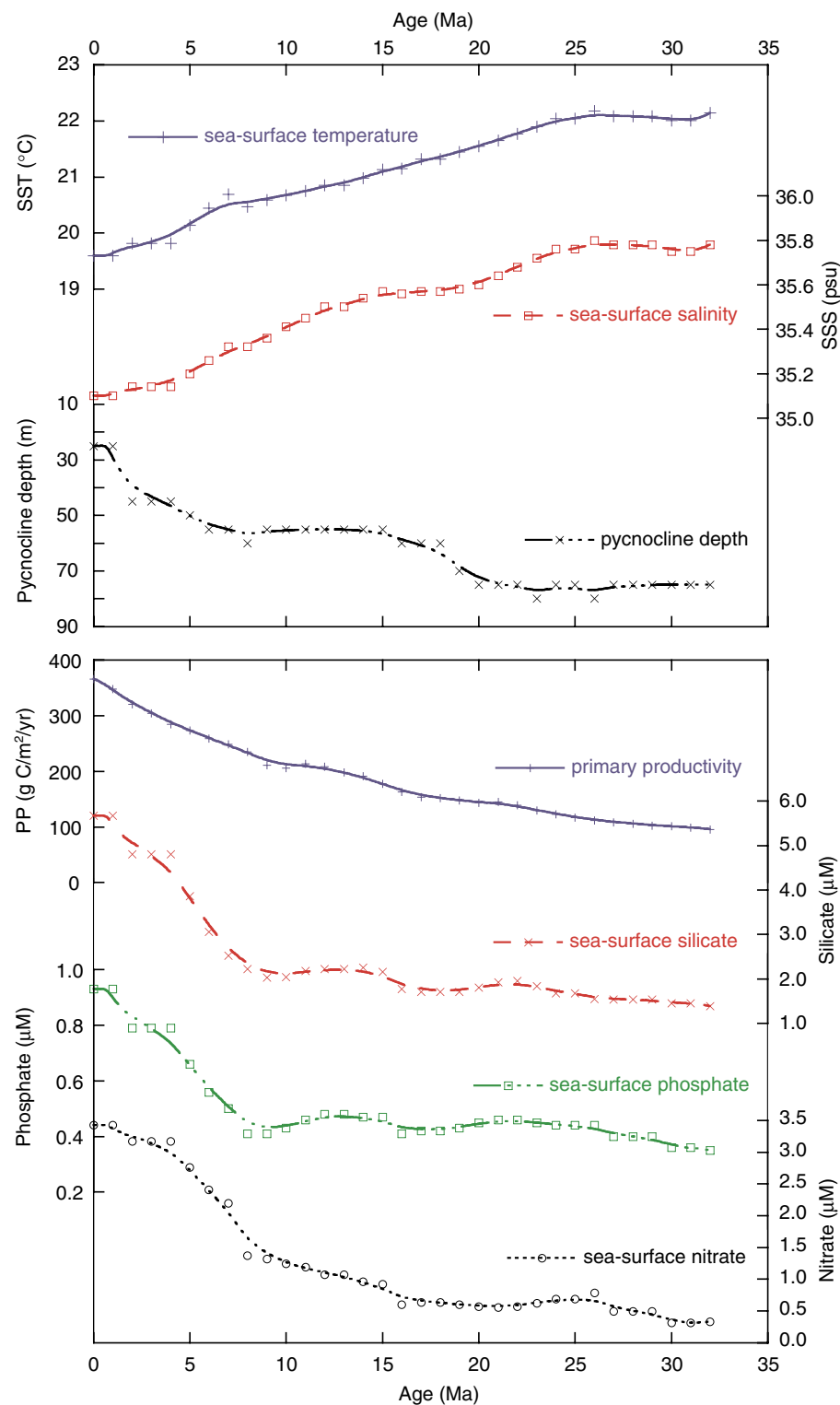


Figure F7. Meridional cross section of water masses, characterized by dissolved oxygen concentrations in the southeast Pacific (Ocean Climate Laboratory, 1999). Southward-spreading middepth waters (PCW = Pacific Central Water) are characterized by relatively low oxygen and salinity and high nutrients. Northward-flowing bottom water, below ~3 km depth, starts as relatively oxygen-rich Antarctic Circumpolar Deep Water (CPDW). Northward-spreading Antarctic Intermediate Water (AAIW), above 1 km depth, is high in oxygen but is low in both salinity and nutrients. The Gunther Undercurrent (GU) flows southward between 100 and 400 m water depth and is characterized by relatively low oxygen, high nutrients, and high salinity.]

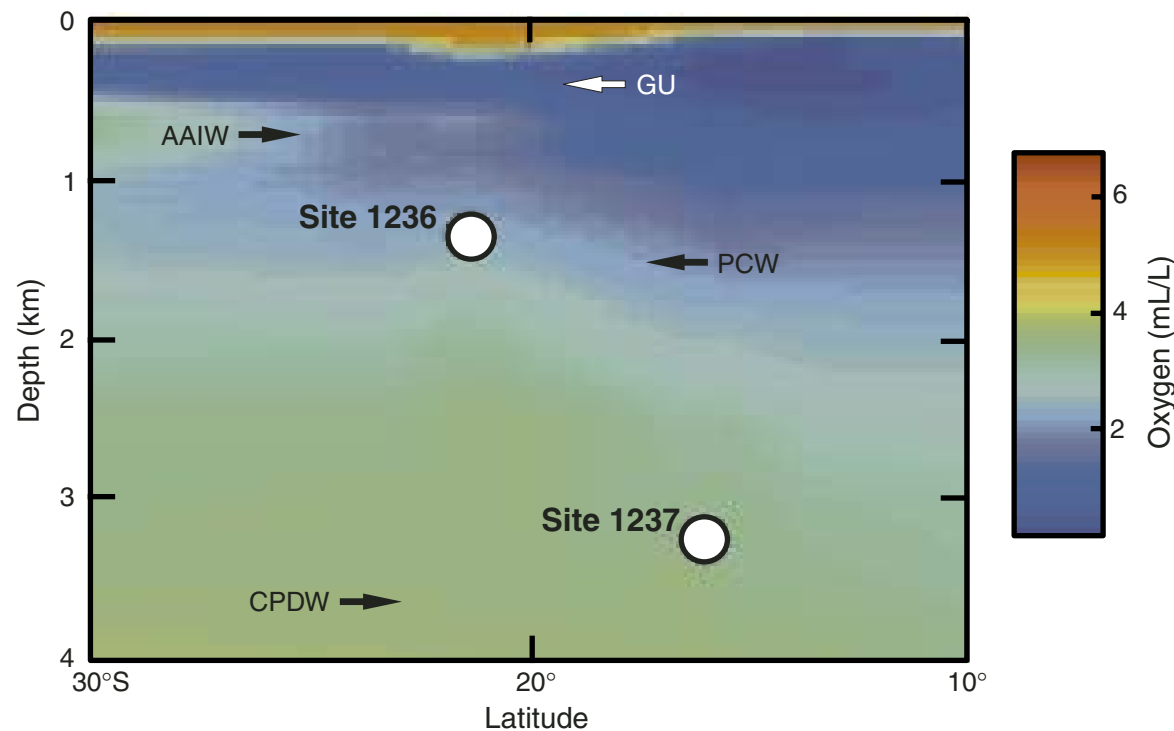


Figure F8. Spliced records of reflectance L* (blue), a* (green), and b* (orange) and magnetic susceptibility (MST-MS) (purple) from Site 1237.

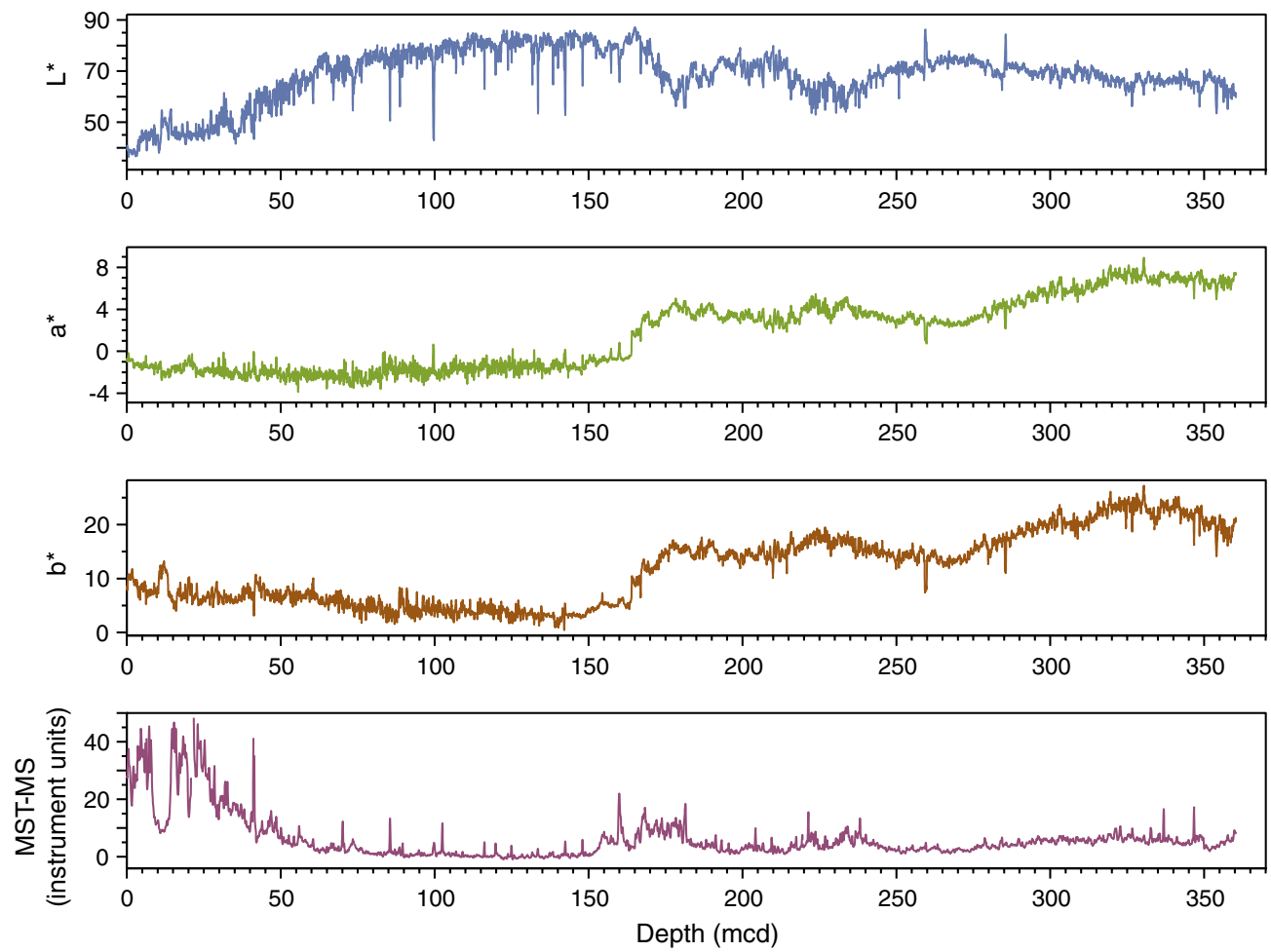


Figure F9. OSU Fast Track magnetic susceptibility data (OSUS-MS) vs. mcd for the spliced record and Holes 1237A (black), 1237B (red), 1237C (green), and 1237D (blue). Gray boxes indicate the portions of cores that are in the splice. Pink boxes indicate areas of uncertainty in the splice. A. 0–40 mcd. B. 30–70 mcd. (Continued on next five pages.)

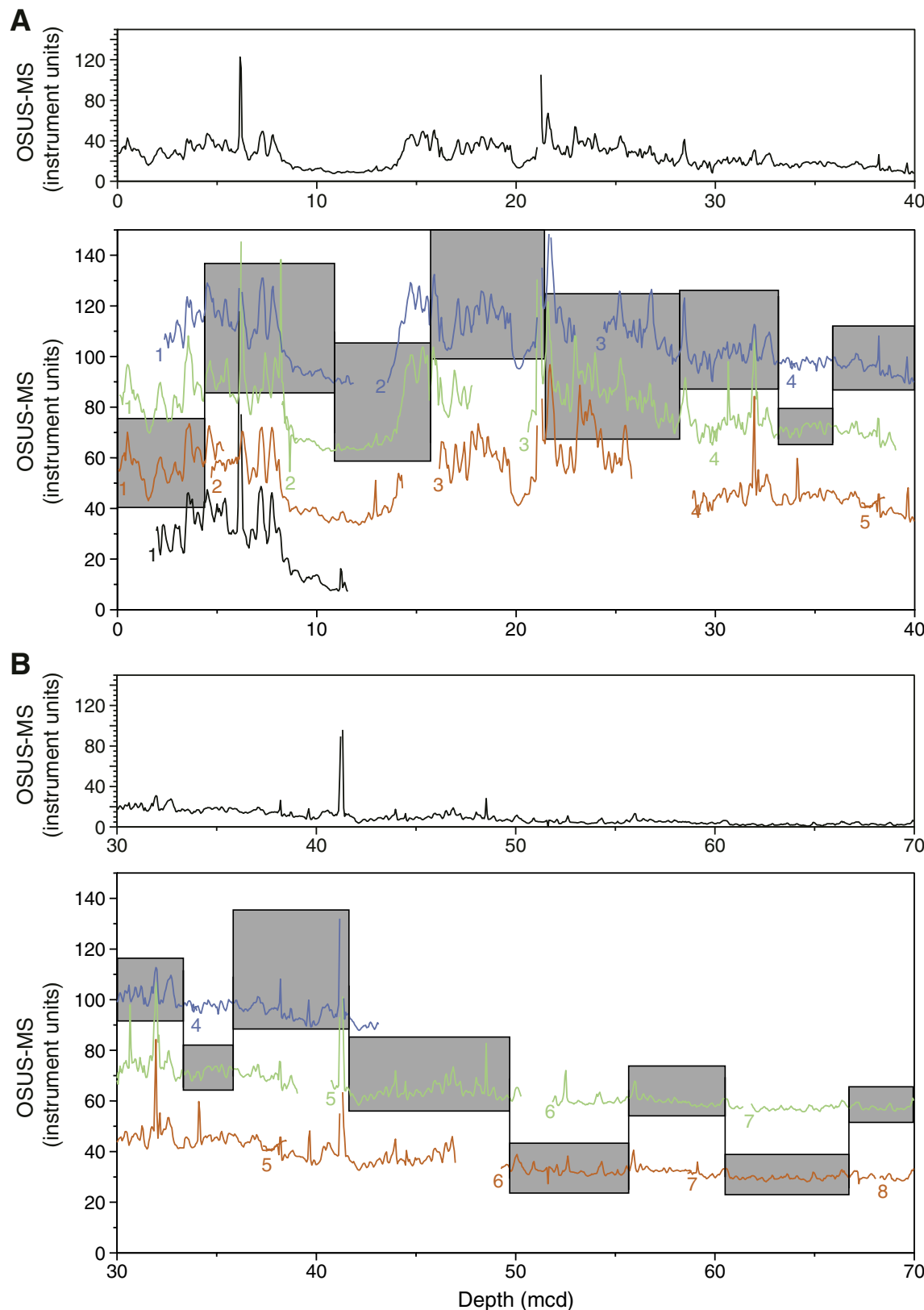


Figure F9 (continued). C. 60–100 mcd. D. 90–130 mcd.

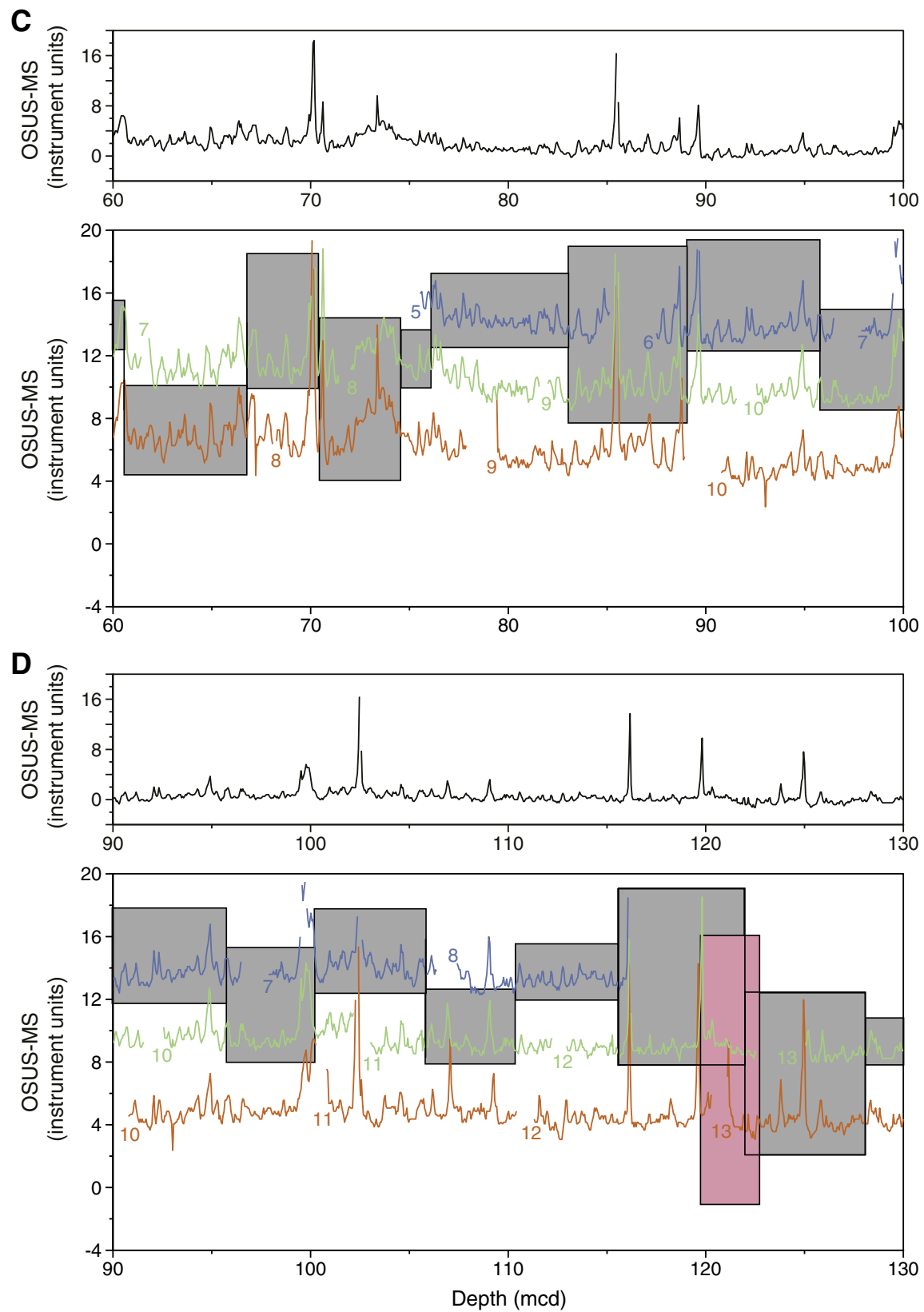


Figure F9 (continued). E. 120–160 mcd. F. 150–190 mcd.

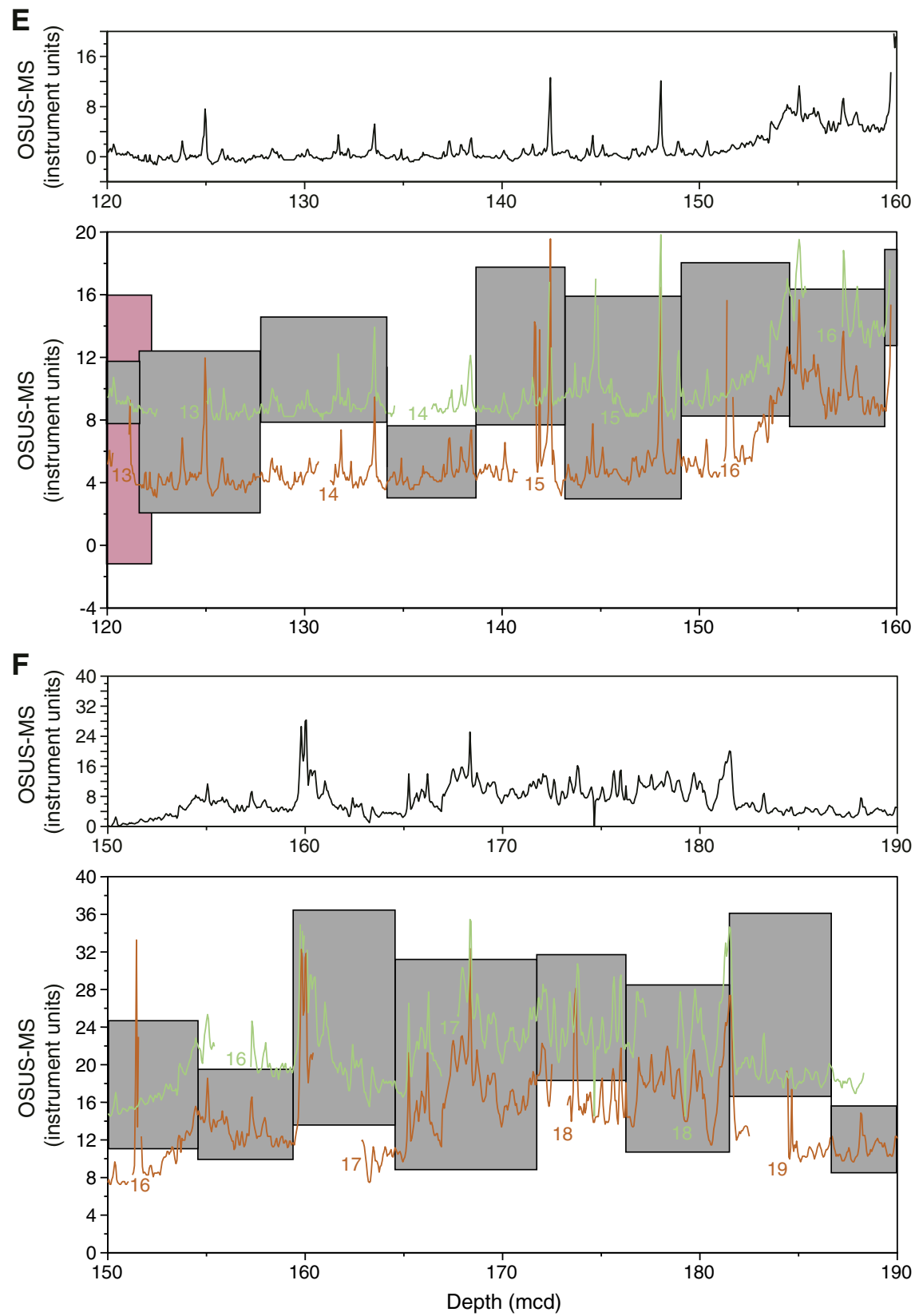


Figure F9 (continued). G. 180–220 mcd. H. 210–250 mcd.

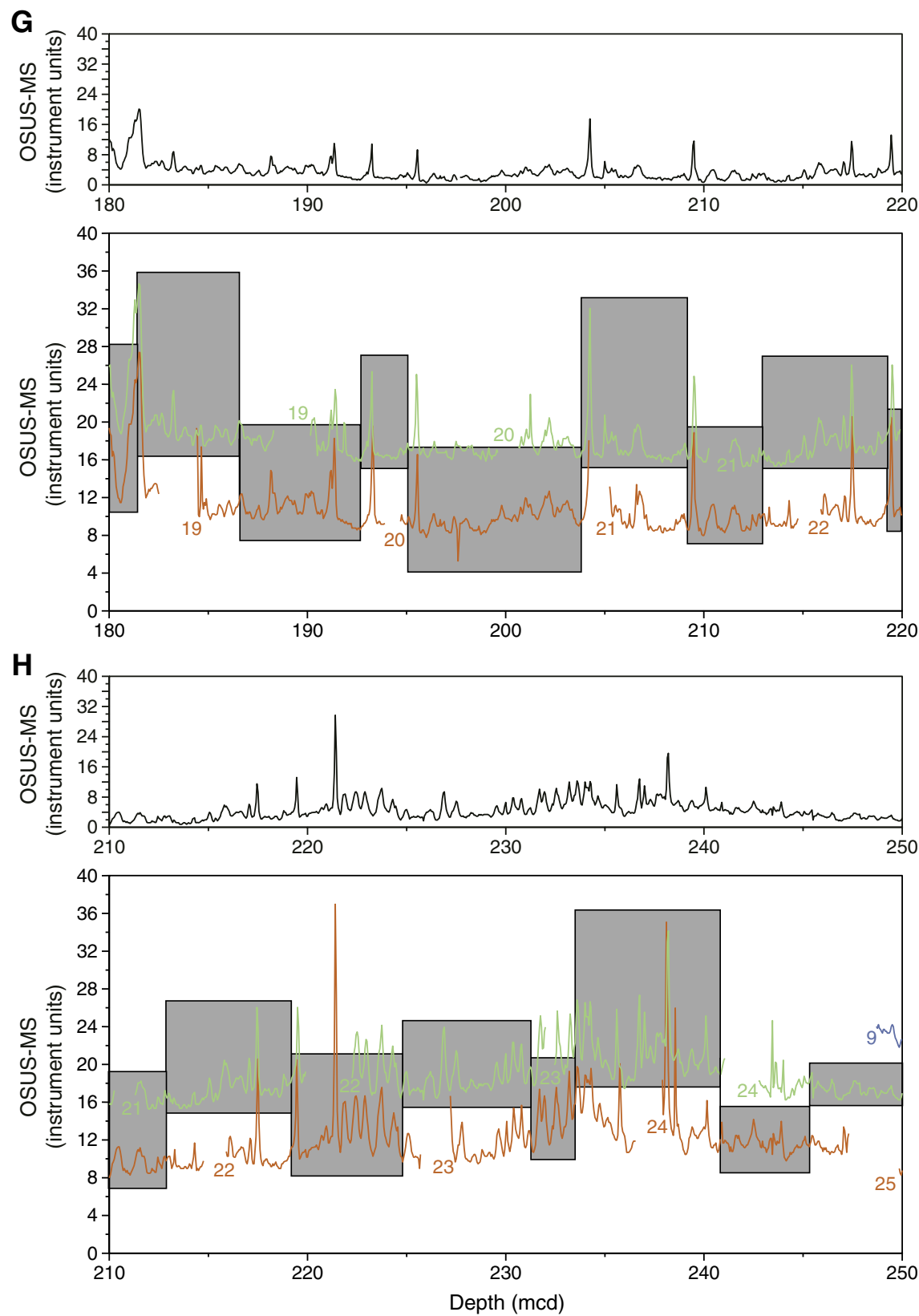


Figure F9 (continued). I. 240–280 mcd. J. 270–310 mcd.

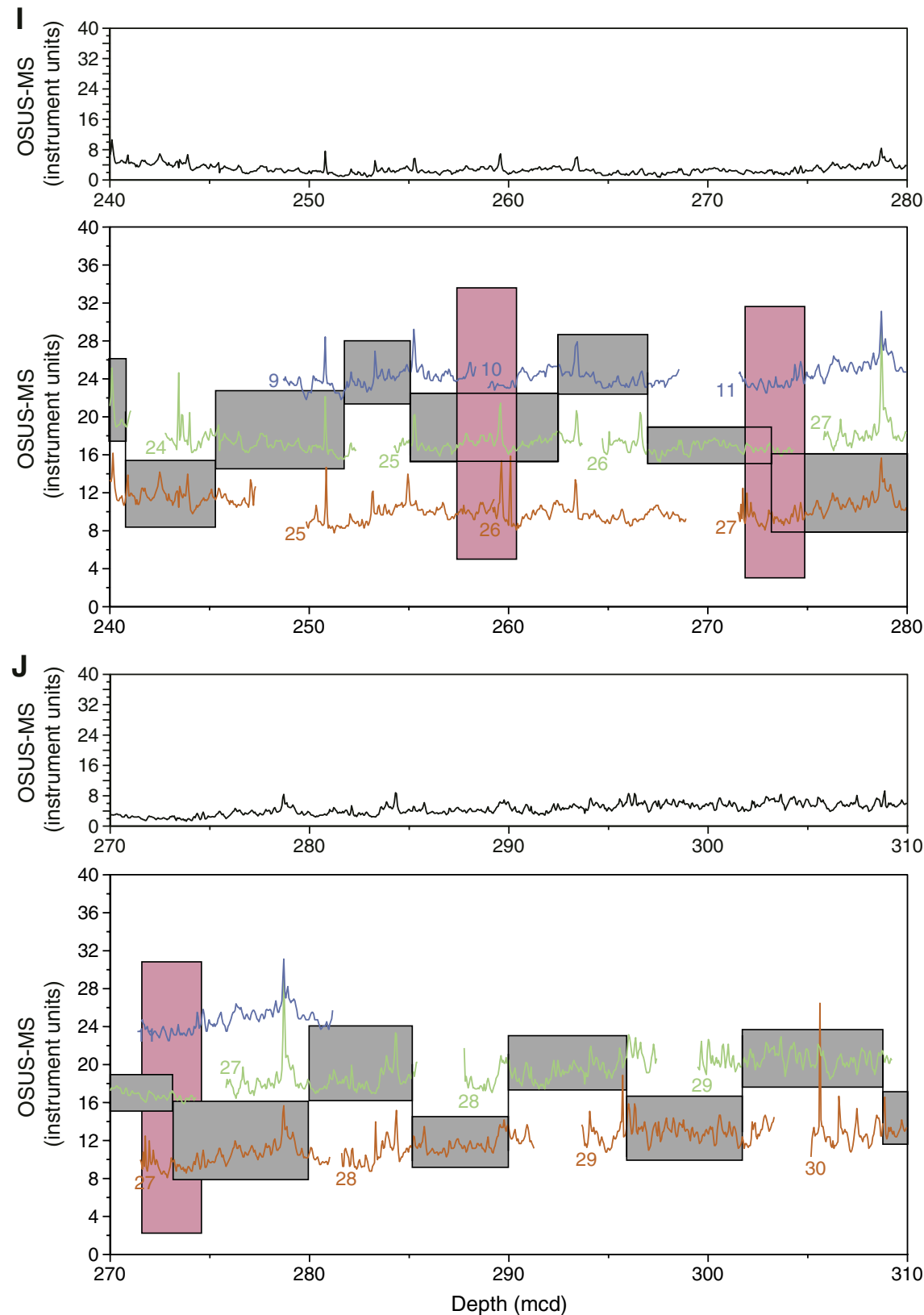


Figure F9 (continued). K. 300–340 mcd. L. 330–370 mcd.

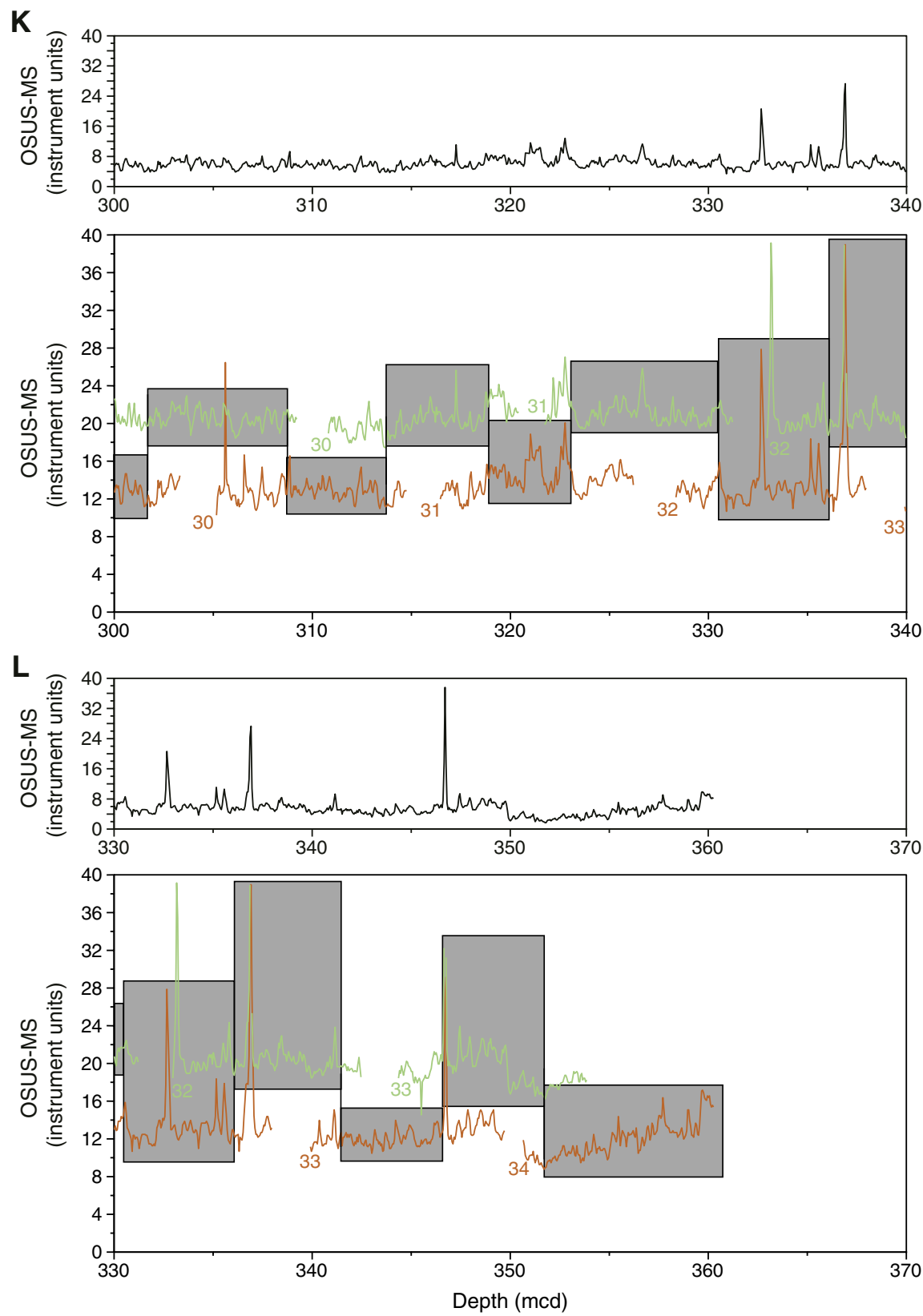


Figure F10. A. A comparison of the drillers depth (mbsf) and meters composite depth (mcd) scales in Holes 1237B through 1237D. B. A comparison of the growth of cumulative depth offset and mcd in the splice for Holes 1237B (red diamonds), 1237C (green squares), and 1237D (blue circles). The blue lines separate intervals of the splice that have different growth factors (GFs). The cores with tops in the interval from 0.00 to 157.10 mcd have a GF of 1.09. The cores with tops in the interval from 162.80 to 254.20 mcd have a GF of 1.13. The cores with tops in the interval from 258.90 to 350.61 mcd have a GF of 1.20. The 1:1 (mbsf:mcd) line is also shown for comparison. The solid black dots are the tie points used to calculate cmcd. Equations are given in Table T2, p. 75.

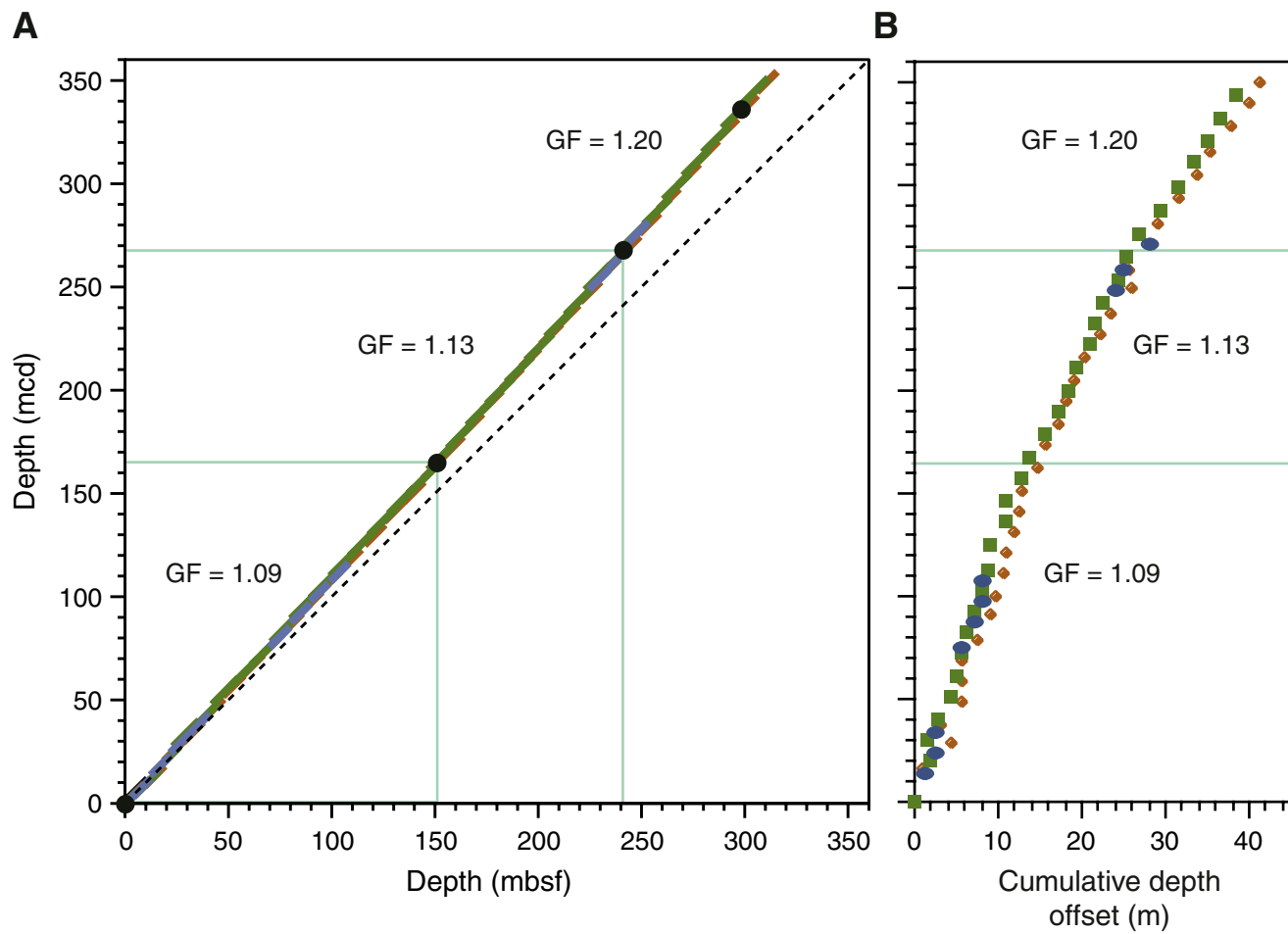


Figure F11. Core recovery, lithostratigraphy, epoch, magnetic susceptibility, natural gamma radiation (Hole 1237B only), gamma ray attenuation (GRA) and moisture and density (MAD; dots), bulk density (Hole 1237B only), grain density, L^* , and calcium carbonate and total organic carbon (TOC) (Hole 1237B only) of recovered sediments from Site 1237. For MS, NGR, GRA, and L^* , gray curves represent the original measured data and black curves indicate a 50-point running average of the original data. Interpolated bulk densities from MAD measurements are provided between ~170 and 240 mcd on the GRA density curve. Dashed lines across the a^* , b^* , and L^* profiles indicate boundaries between three color populations shown in Fig. F13, p. 46. At right, CaCO_3 is the black line and TOC is the gray line. Lines = GRA density, dots = MAD density.

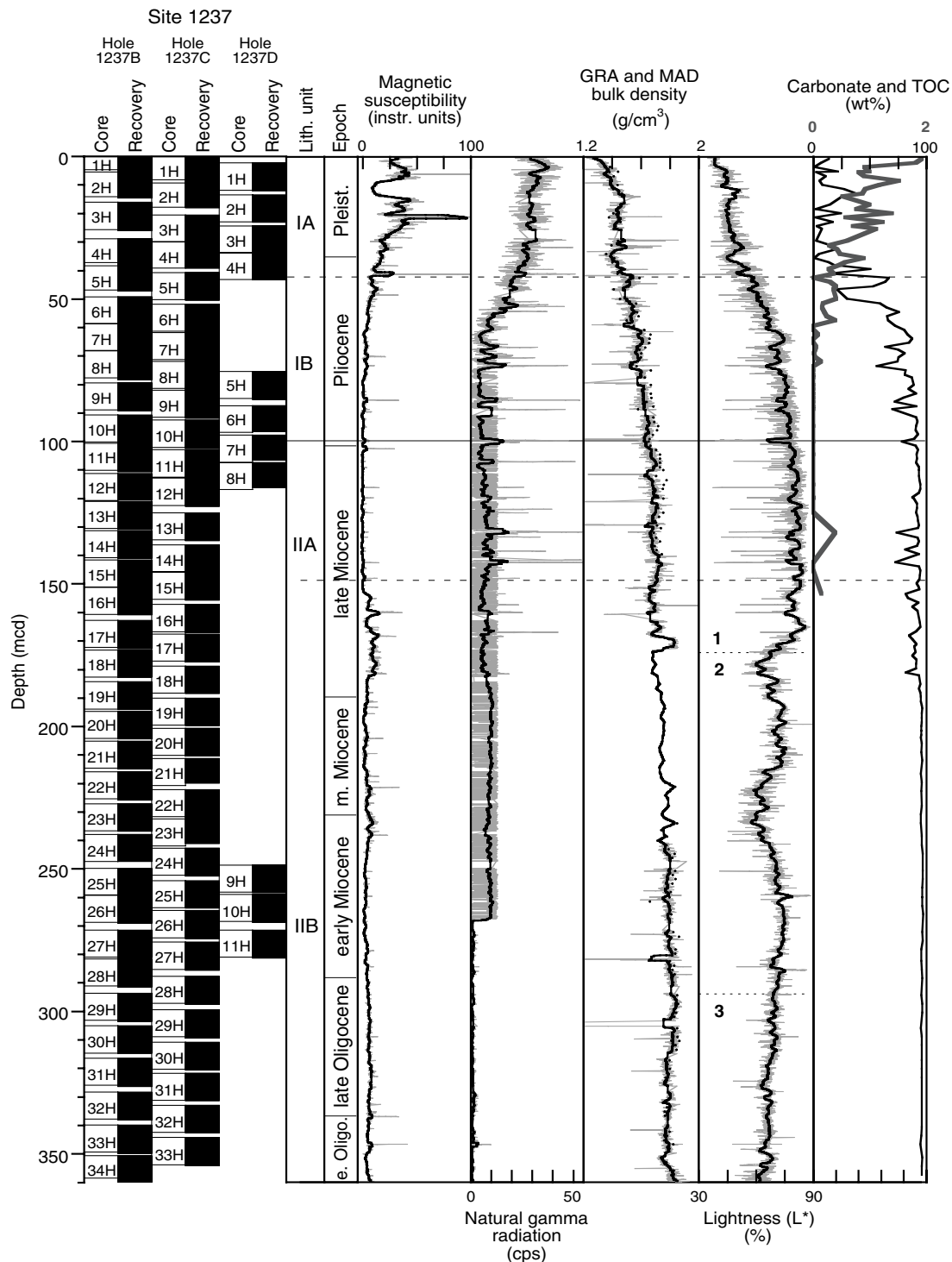


Figure F12. Major components observed in smear slides. Solid circles = dominant lithologies, open squares = minor lithologies.

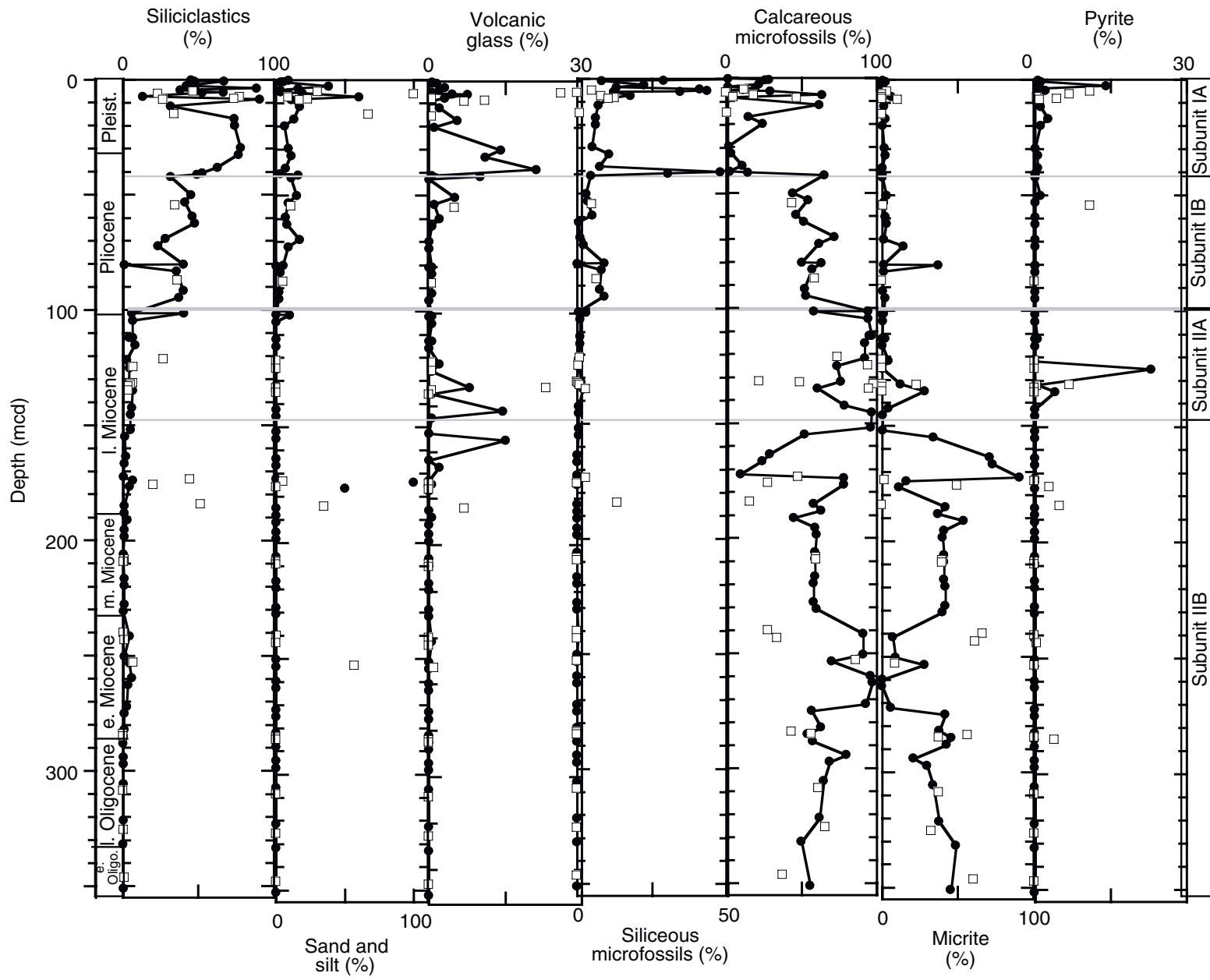


Figure F13. Site 1237 color measurements (spliced record). A. Color measurements plotted in the a^* - b^* plane. B. Close up of the L^* - a^* plane. C. Close-up of the L^* - b^* plane. D. Close-up of the a^* - b^* plane. Measurements plot in two main regions in the a^* - b^* color plane: the generally greenish sediments of Unit I and Subunit IIA group in the first quadrant, whereas the reddish sediments of the Subunit IIB cluster more tightly in the second quadrant. Three populations (IIB1, IIB2, and IIB3) can be distinguished within the red part of the color space.

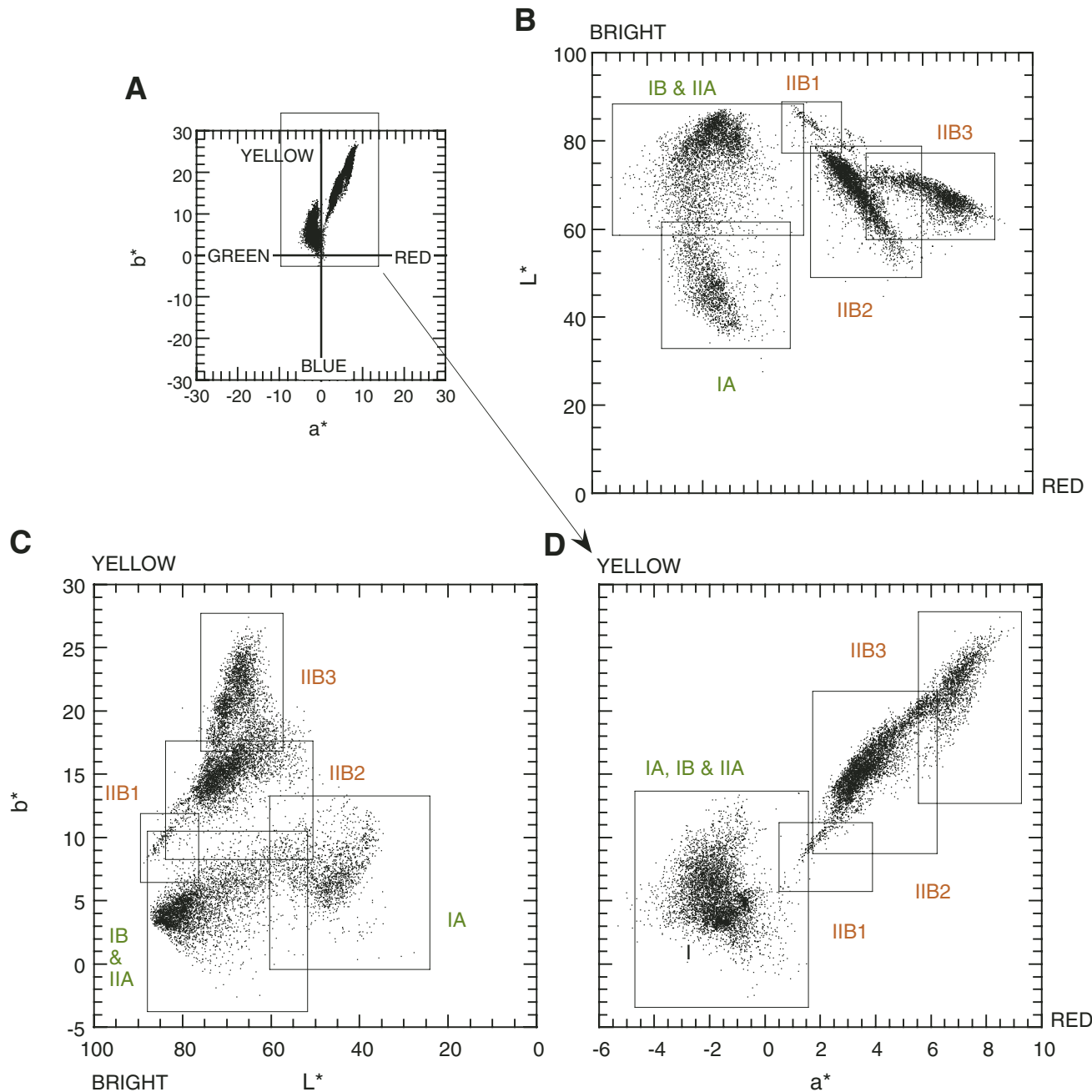


Figure F14. Ash layers from Site 1237. The figure shows (from left) the cumulative number of ash layers and layer thickness, volcanic glass size, the presence of pyroxenes, the presence of amphiboles, and the abundance of biotite. Opx = orthopyroxene, cpx = clinopyroxene.

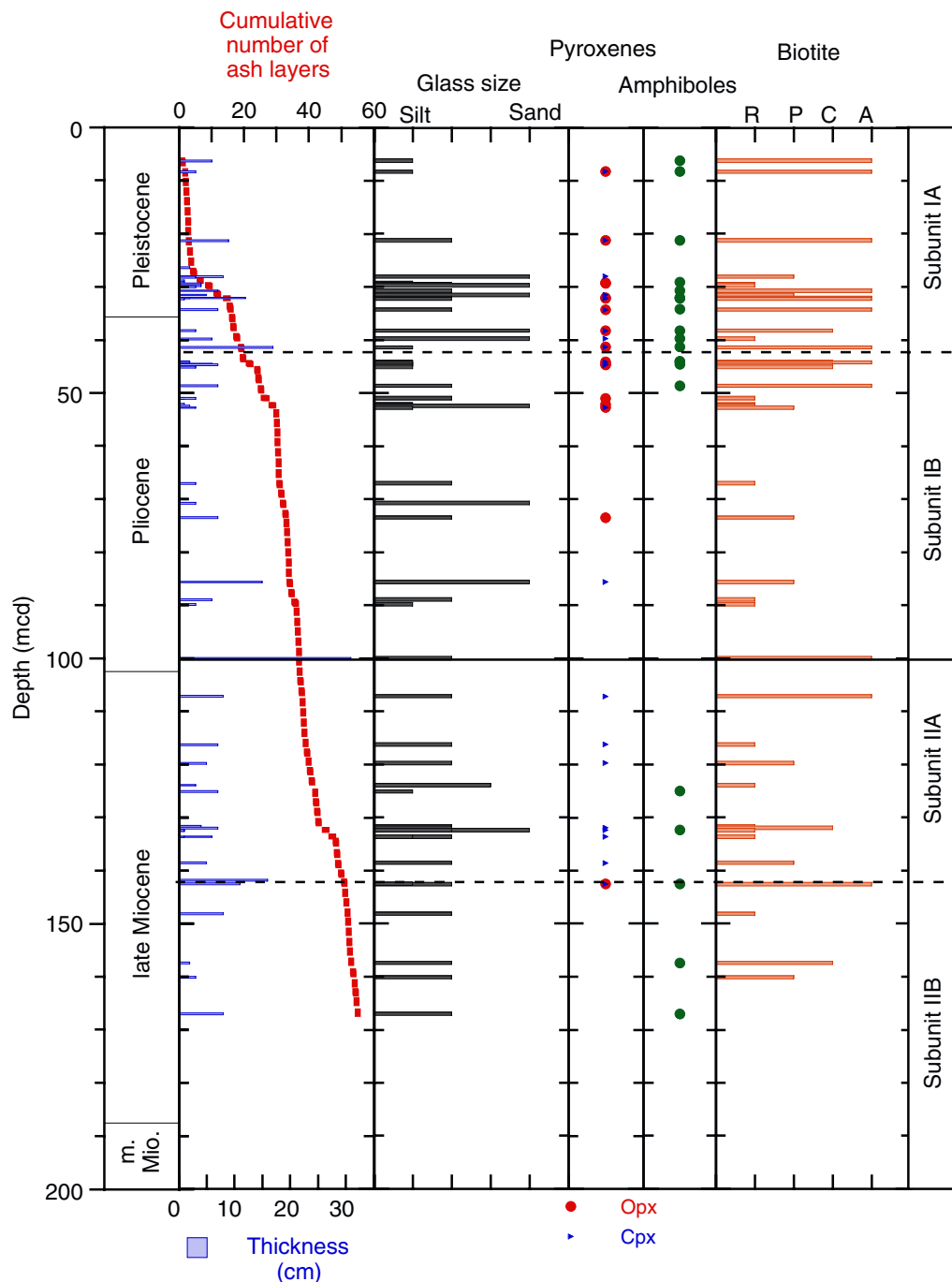


Figure F15. Digital close-up photograph of an ash layer at ~41.3 mcd (interval 202-1237B-5H-3, 80–104 cm). The base of this ash layer defines the boundary between Subunits IA and IB.

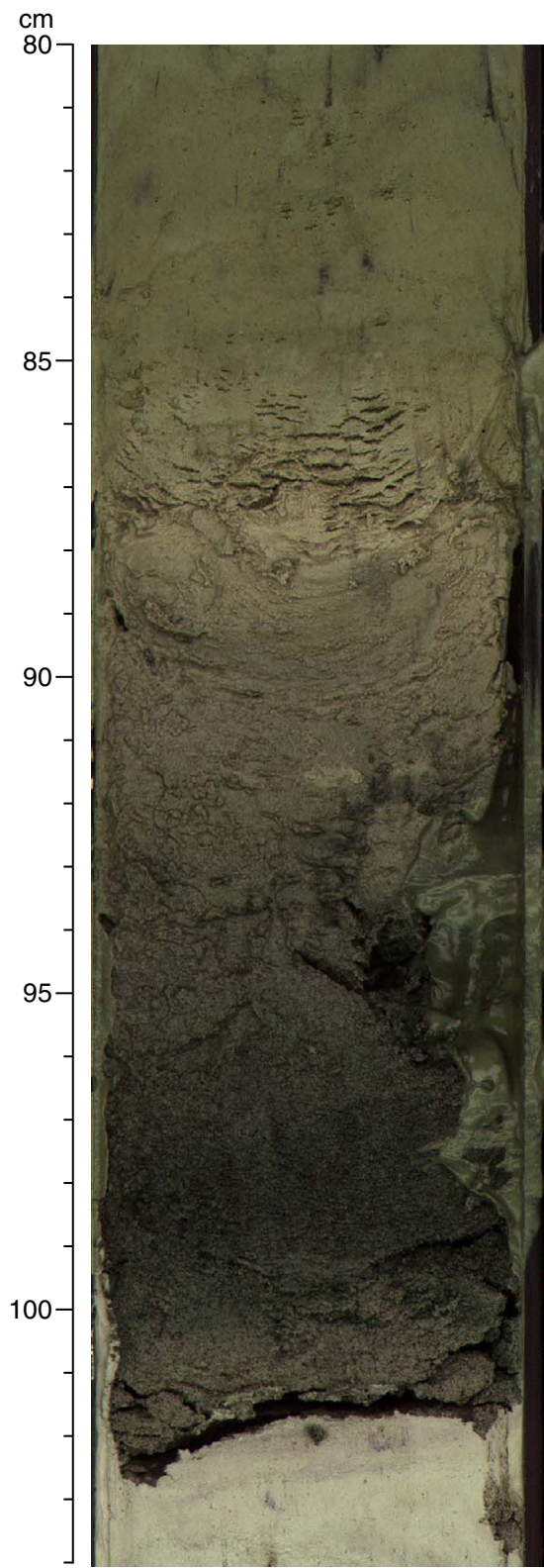


Figure F16. Digital close-up photograph of *Zoophycos* in Subunit IA (interval 202-1237B-4H-3, 80–103 cm).

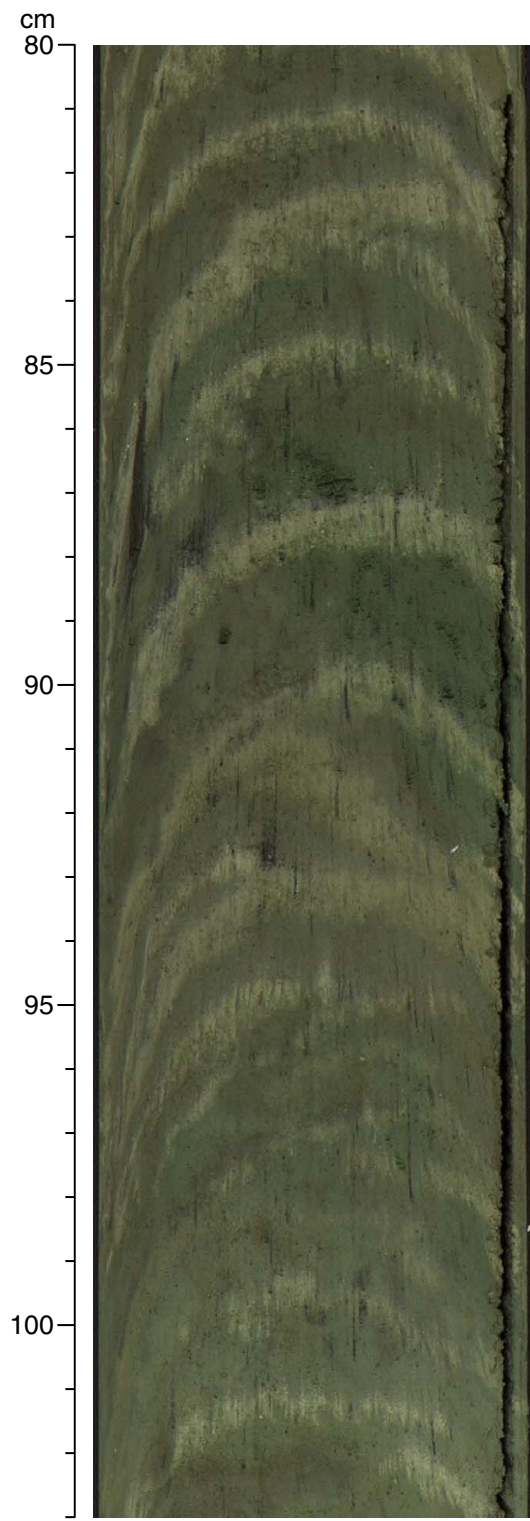


Figure F17. Digital close-up photograph of a trace fossil surrounded by a gray halo in Subunit IB (interval 202-1237B-6H-4, 100–105 cm).



Figure F18. Digital close-up photograph of purple and green color bands in Subunit IB (interval 202-1237B-6H-4, 70-95 cm).

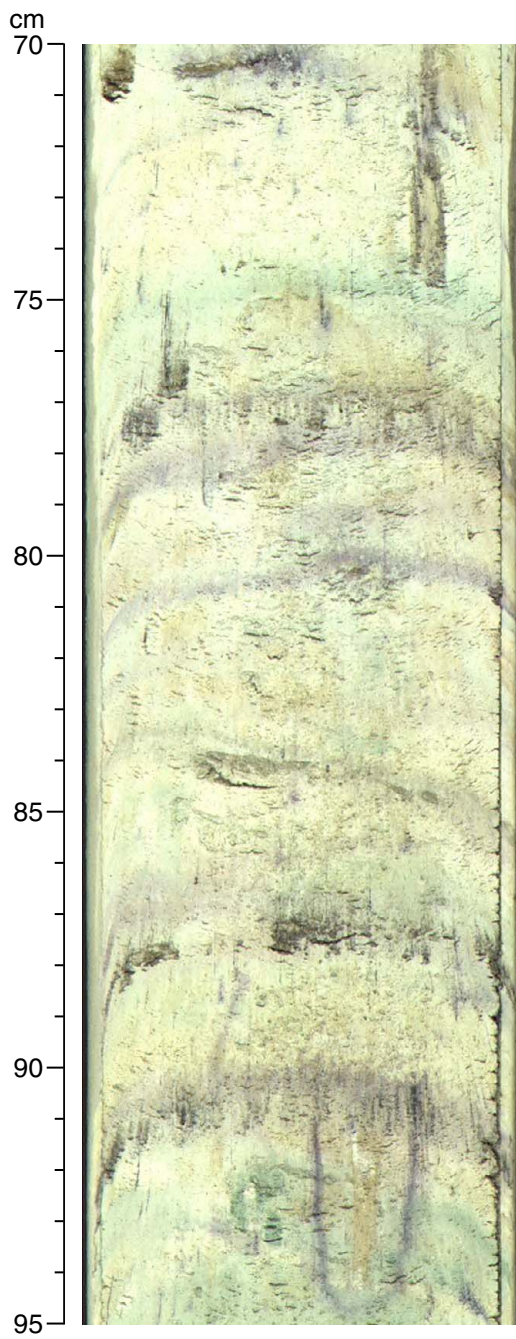


Figure F19. Digital close-up photograph of green and purple color banding in Subunit IIA (interval 202-1237B-12H-1, 100–120 cm). Small sulfidic black spots are also observed.

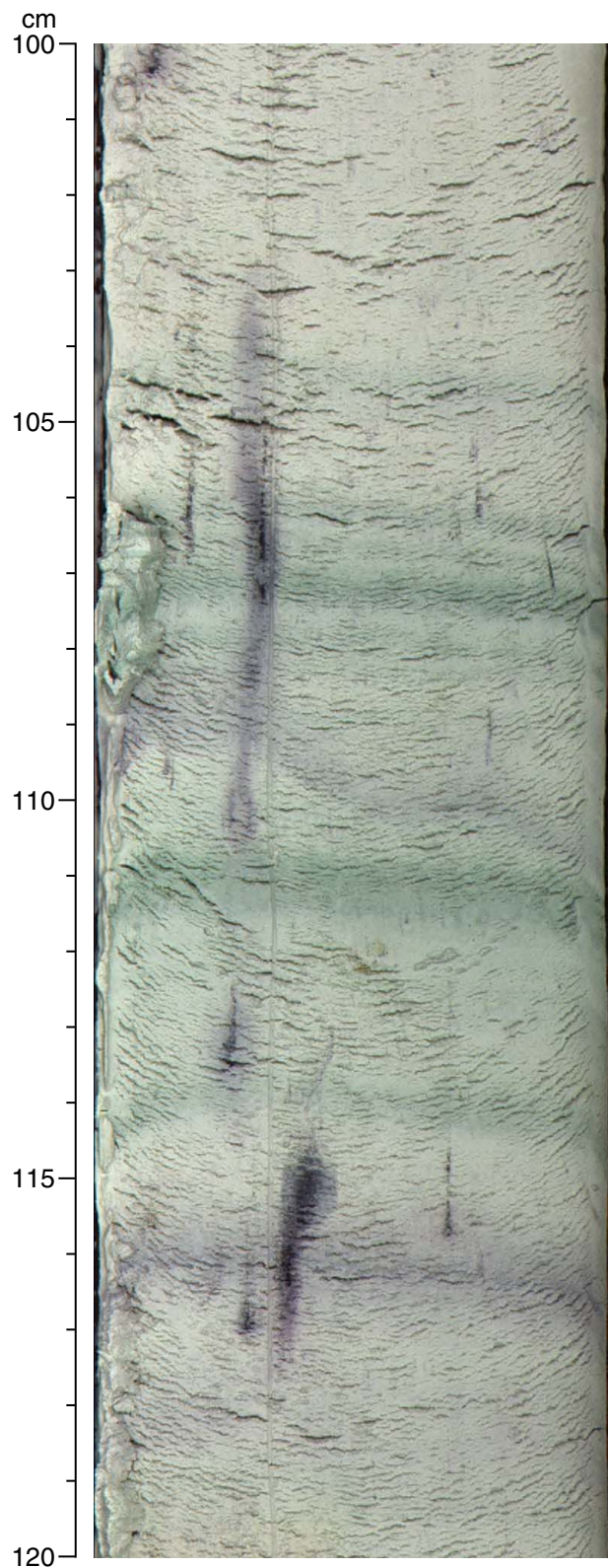


Figure F20. X-ray diffraction (XRD) diffractograms of a green band (interval 202-1237B-14H-1, 59–60 cm) and the basal part of an ash layer (interval 202-1237B-14H-1, 62–63 cm).

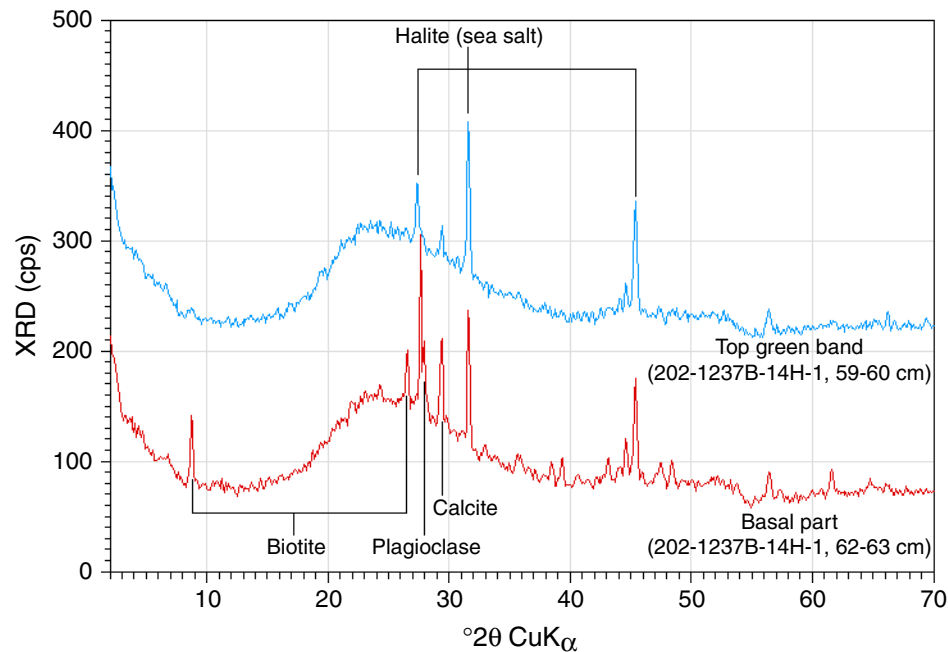


Figure F21. Digital close-up photograph of sharp color change at ~162 mcd in Subunit IIB (interval 202-1237B-17H-1, 80–100 cm).

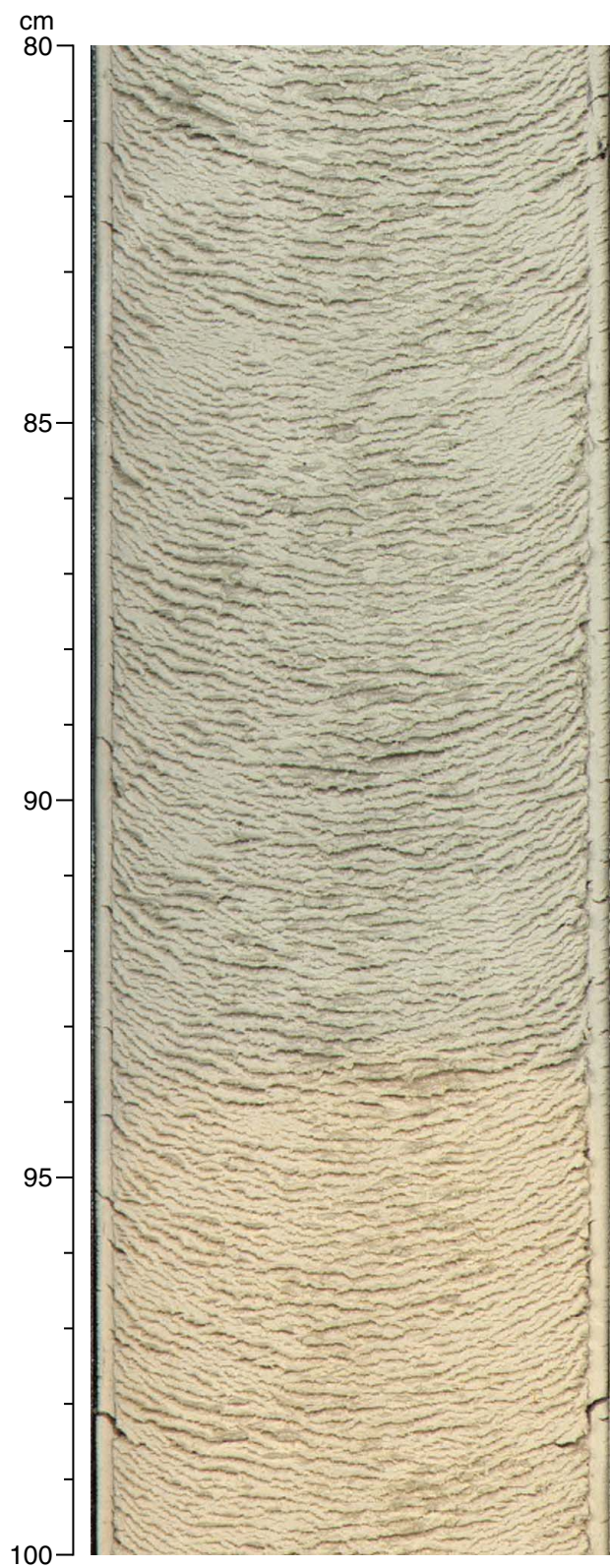


Figure F22. Digital close-up photograph of a firmground in Subunit IIB (interval 202-1237B-33H-5, 85–95 cm). The light-colored sediment is partially lithified and rich in micrite.

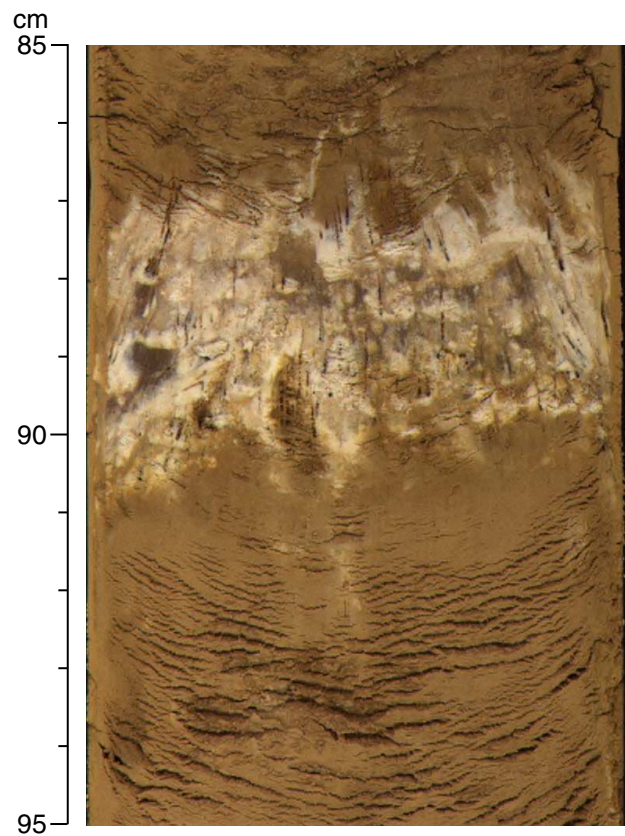


Figure F23. Simplified depositional history of sediment components. Approximate position of Site 1237 relative to South America (see “[Introduction](#),” p. 1), timing of tectonic events (Gregory-Wodzicki, 2000), and ice sheet events (Zachos et al., 2001) are also shown for comparison.

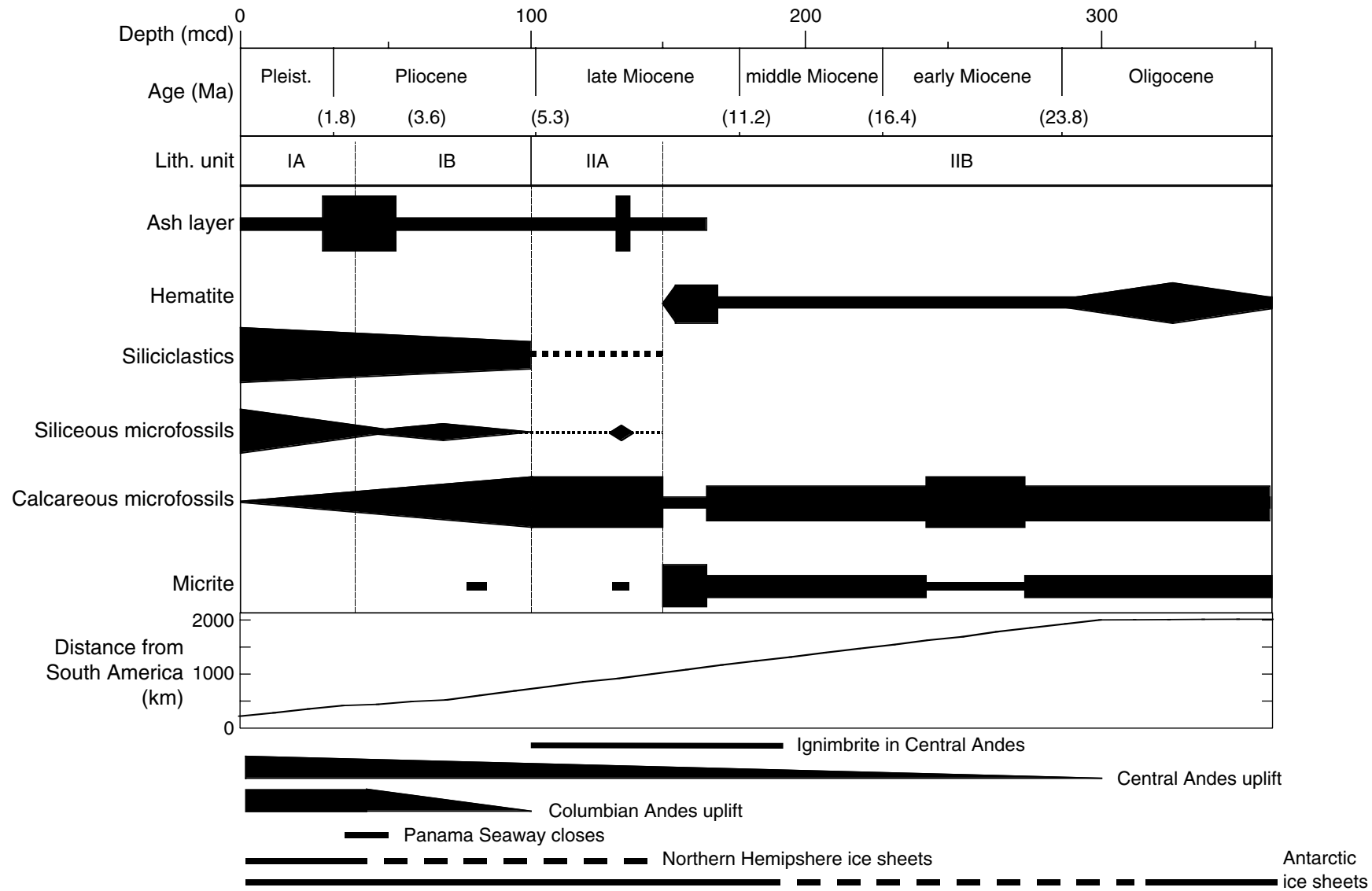


Figure F24. Measured (solid circles) and predicted (gray lines) shipboard carbonate and total organic carbon (TOC). Predicted values are calculated by multiple linear regression of shipboard reflectance data and geochemical measurements.

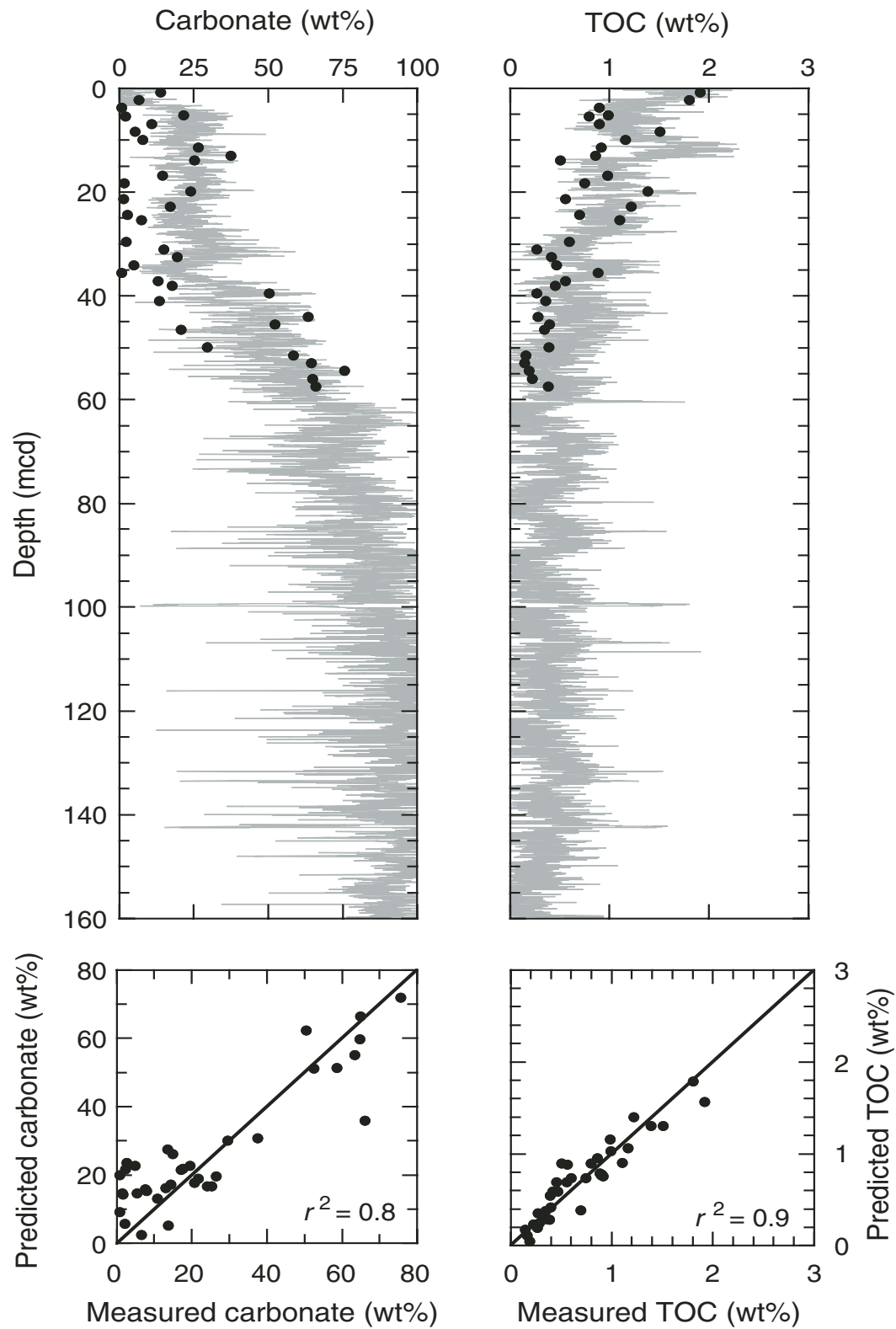


Figure F25. Sequential depth plots of (A) raw reflectance data, (B) their first derivatives, (C) typical first derivatives at various levels within sediments, and (D) a preliminary uncalibrated hematite record (i.e., hematite peak height) vs. age for the spliced record at Site 1237. Characteristic peaks for goethite (G) and hematite (H) are indicated. %' = the first derivative of % with respect to wavelength.

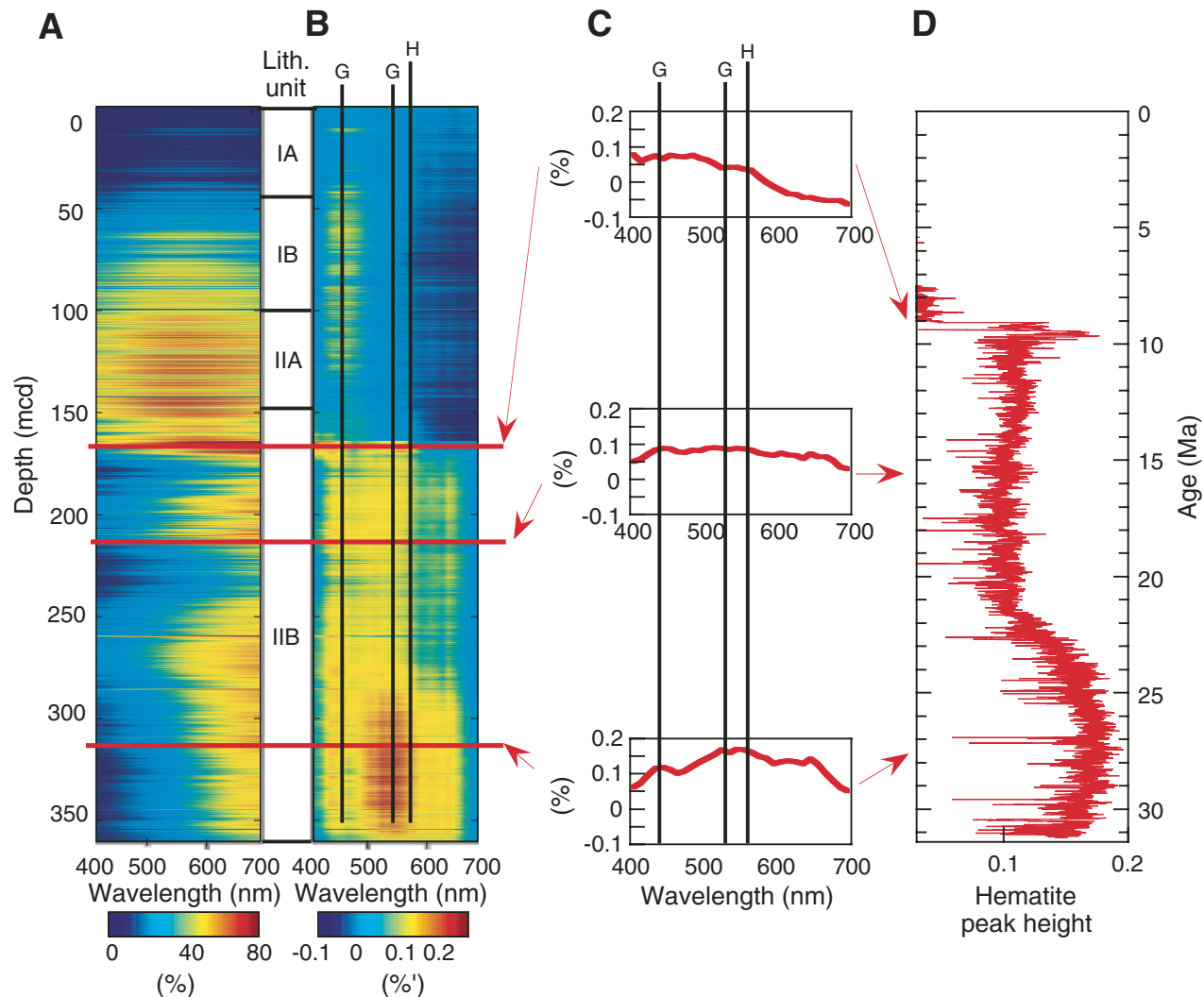


Figure F26. Core recovery, calcareous nannofossil and foraminifer abundance, benthic foraminifer percentage of total foraminifers, and diatom abundance in Hole 1237B (smoothed lines). B = barren, R = rare, F = few, C = common, A = abundant, VA = very abundant.

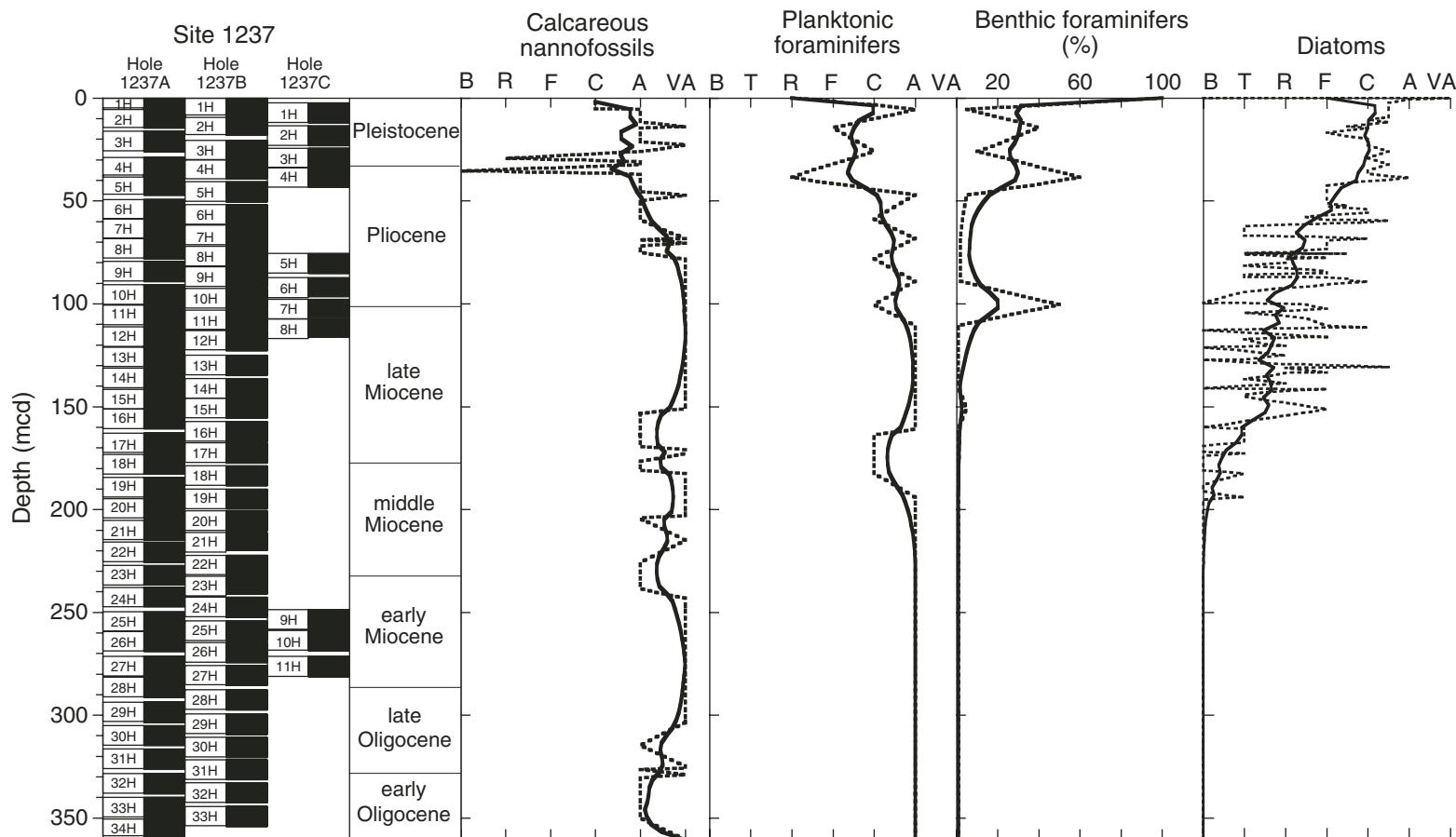


Figure F27. Site 1237 natural remanent magnetization (NRM) intensity before and after AF demagnetization at peak fields of 25 mT vs. depth. Core recovery is shown for reference.

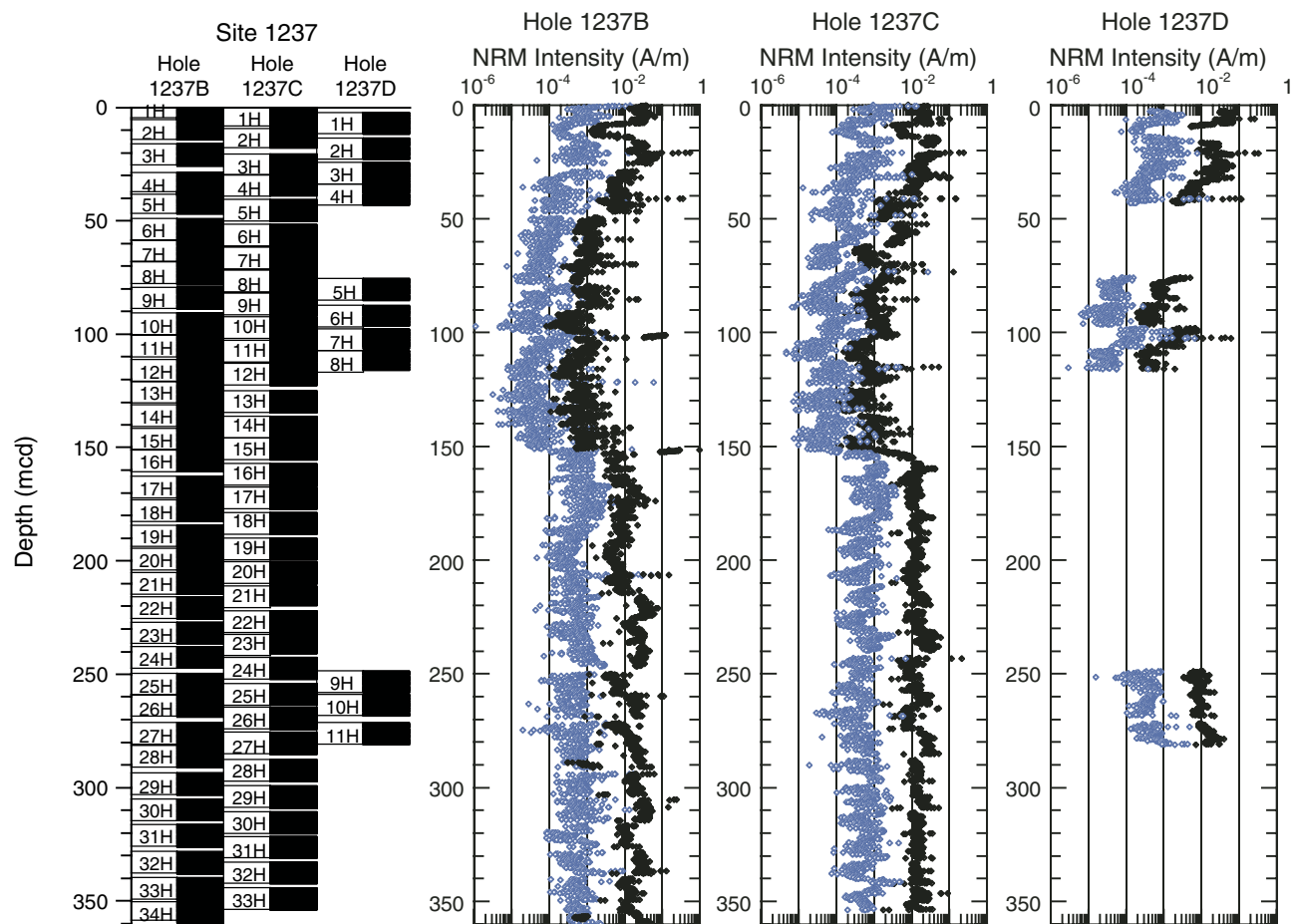


Figure F28. Site 1237 inclination after demagnetization at peak alternating fields of 25 mT vs. depth. Core recovery is shown for reference.

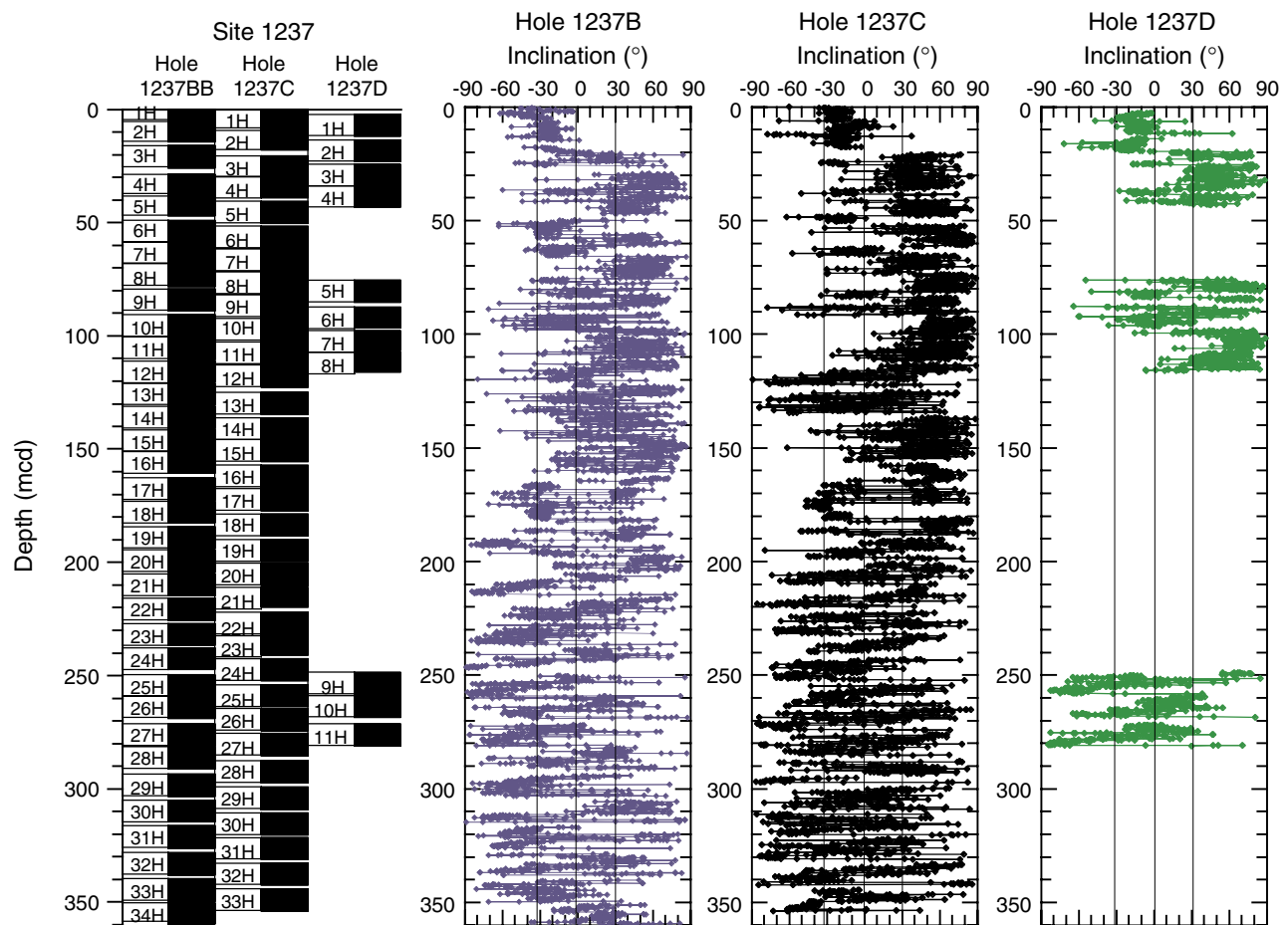


Figure F29. Inclination after demagnetization at peak alternating fields of 25 mT for the upper 100 mcd of (A) Hole 1237B, (B) Hole 1237C, and (C) Hole 1237D with the accompanying polarity interpretations.

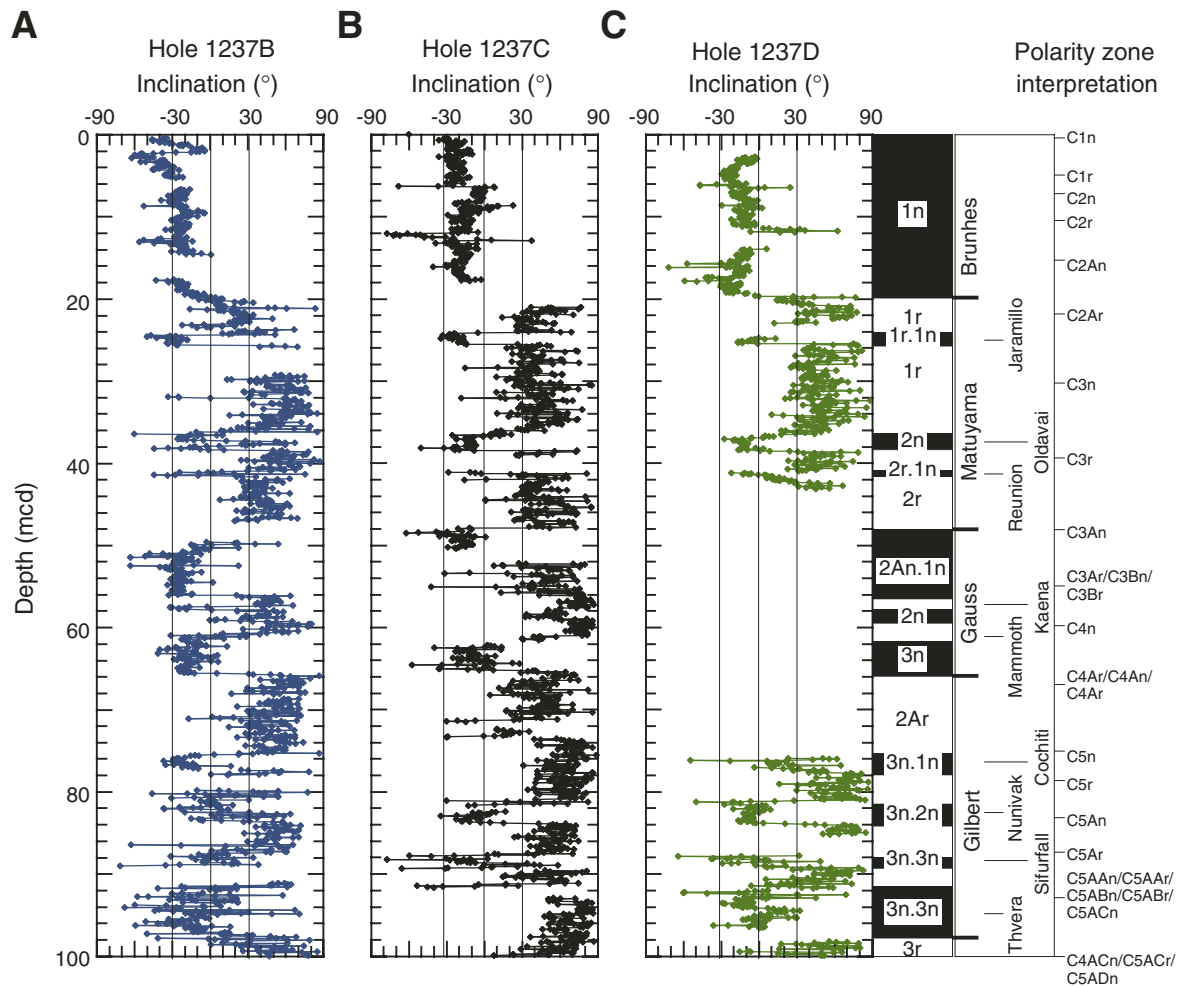


Figure F30. Inclination after demagnetization at peak alternating fields of 25 mT for the 100- to 200-mcd interval of (A) Hole 1237B, (B) Hole 1237C, and (C) the stacked and smoothed record with the accompanying polarity interpretations.

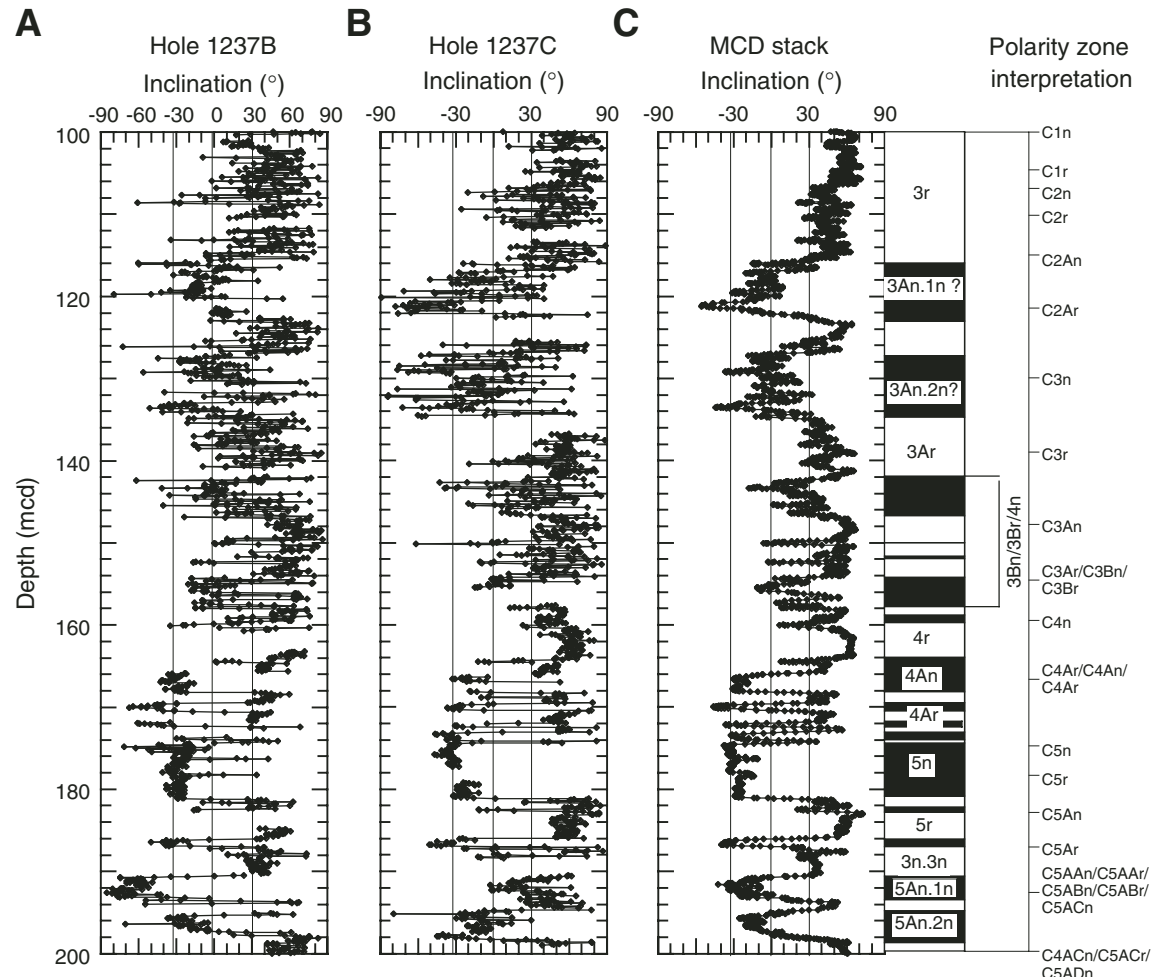


Figure F31. Inclination after demagnetization at peak alternating fields of 25 mT for the 200- to 300-mcd interval of (A) Hole 1237B, (B) Hole 1237C, (C) Hole 1237D, and (D) the stacked and smoothed record with the accompanying polarity interpretations.

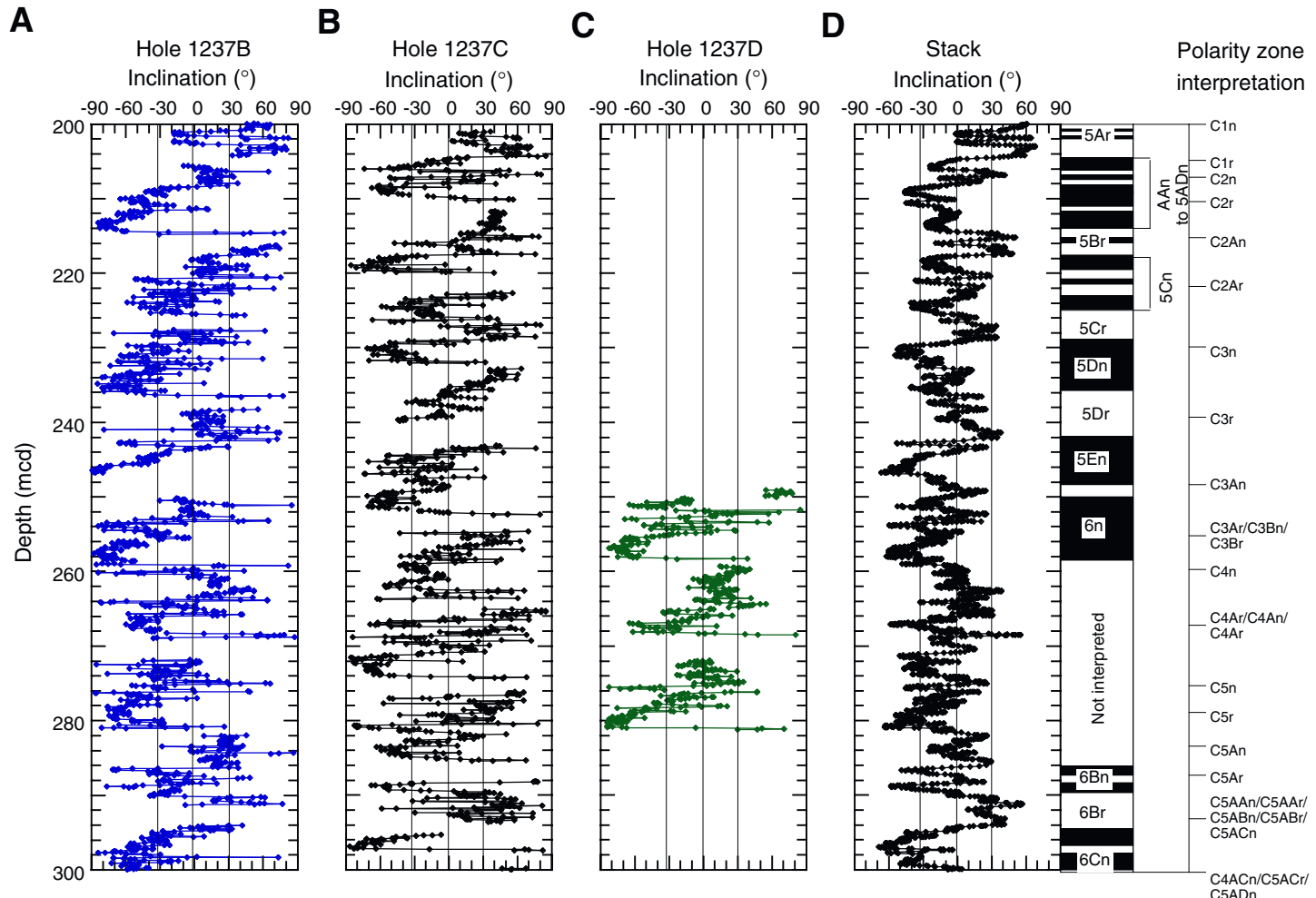


Figure F32. Inclination after demagnetization at peak alternating fields of 25 mT for the 300- to 360-mcd interval of (A) Hole 1237B, (B) Hole 1237C, and (C) the stacked and smoothed record with the accompanying polarity interpretations.

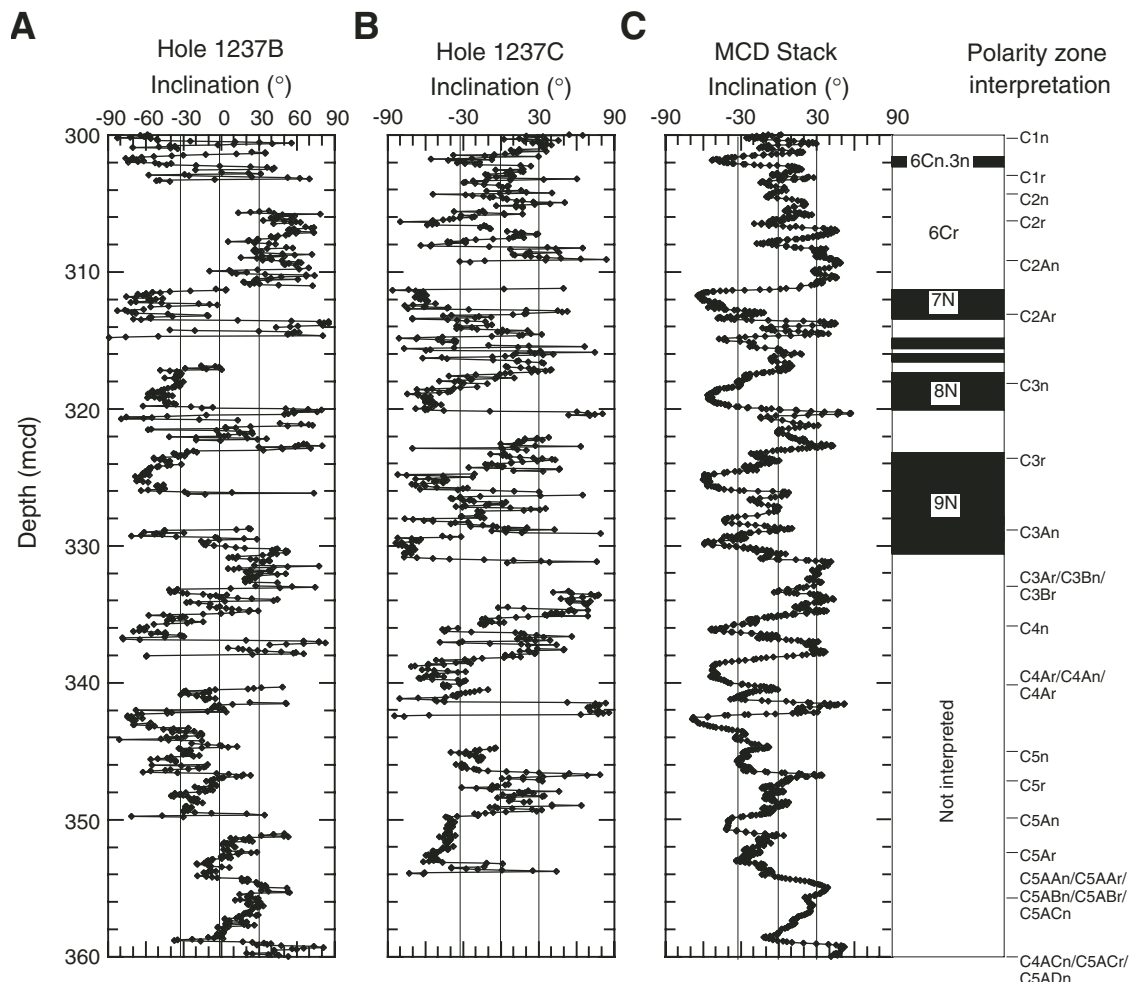


Figure F33. Headspace methane (C_1) concentrations in sediments from Hole 1237B vs. depth.

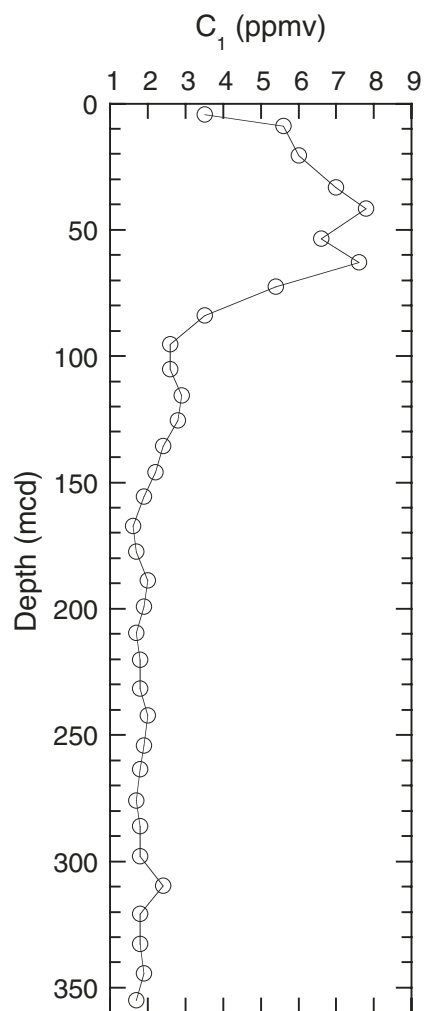


Figure F34. Interstitial water geochemical data for Site 1237. Open squares = calcium concentrations. Solid horizontal lines = lithologic unit boundaries, dashed lines = subunit boundaries (see “[Description of Lithologic Units](#),” p. 7, in “[Lithostratigraphy](#)”). Values below the detection limit (0.1 μM for manganese and 11 μM for ammonium) are plotted at zero. Iron and barium concentrations (not plotted) are in almost all samples below their respective detection limits (iron = 1.1 μM ; barium = 0.03 μM).

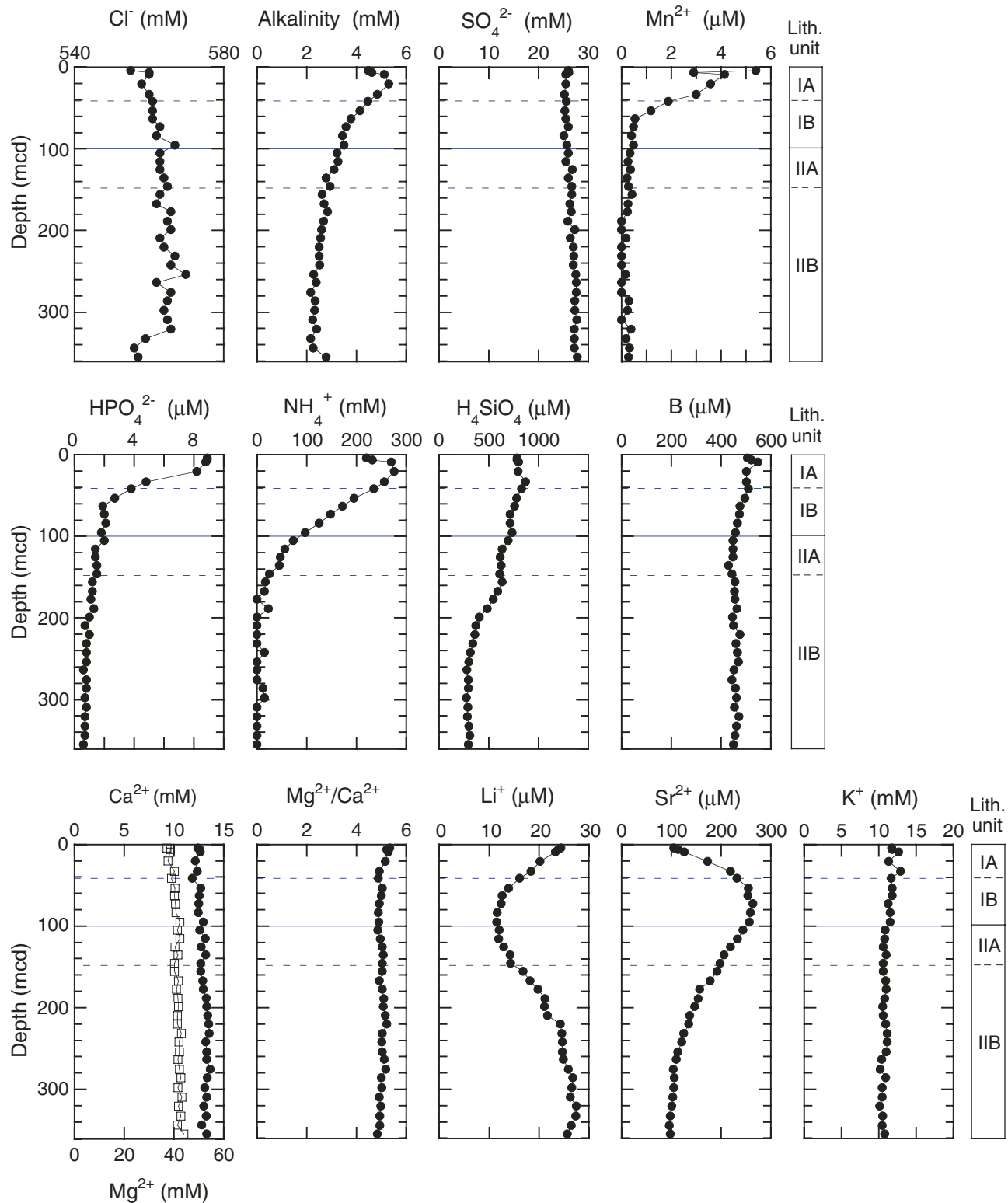


Figure F35. Calcium carbonate (CaCO_3), total organic carbon (TOC), and TOC/total nitrogen ratio (TOC/TN) vs. mcd from sediments of Hole 1237B.

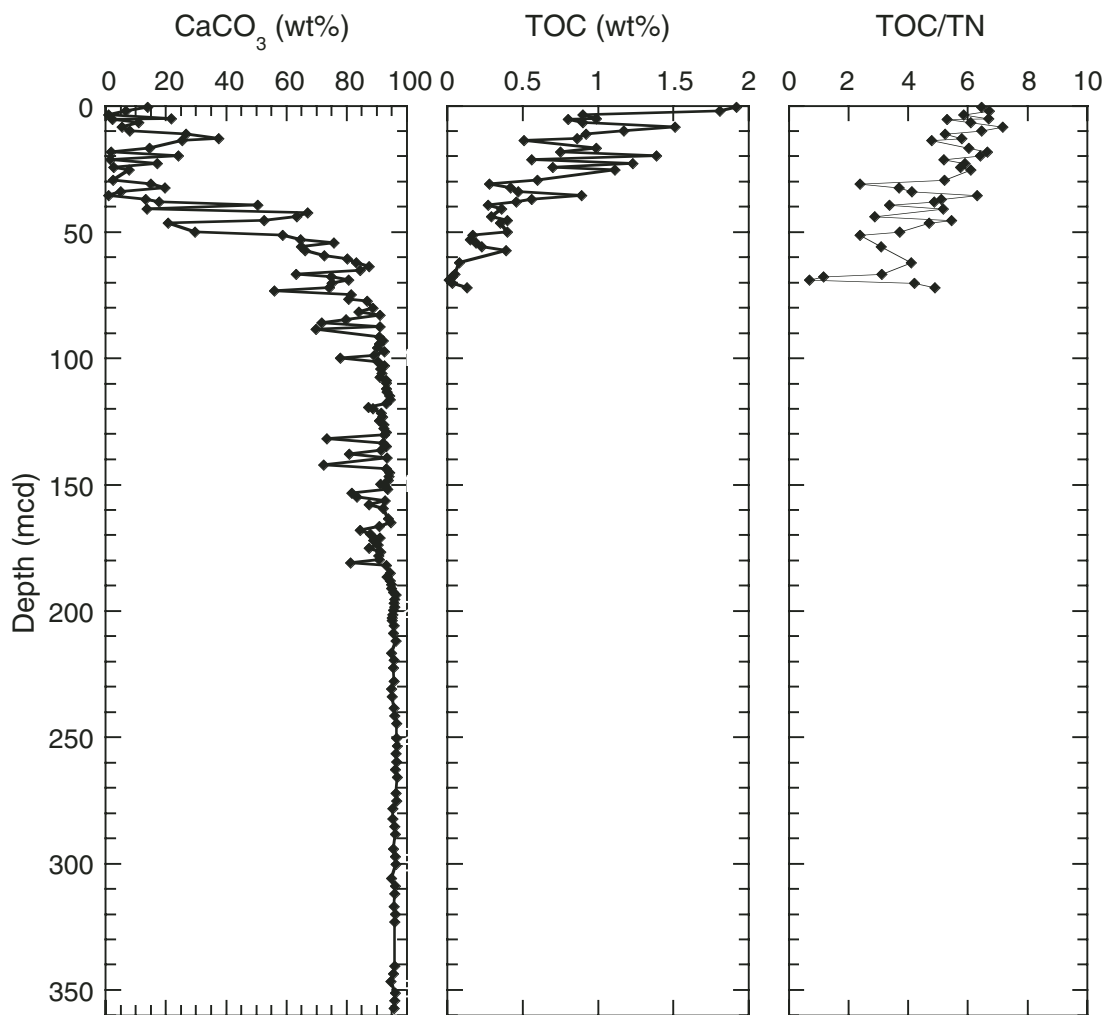


Figure F36. Total organic carbon (TOC) vs. calcium carbonate (CaCO_3) concentrations in sediments from Hole 1237B.

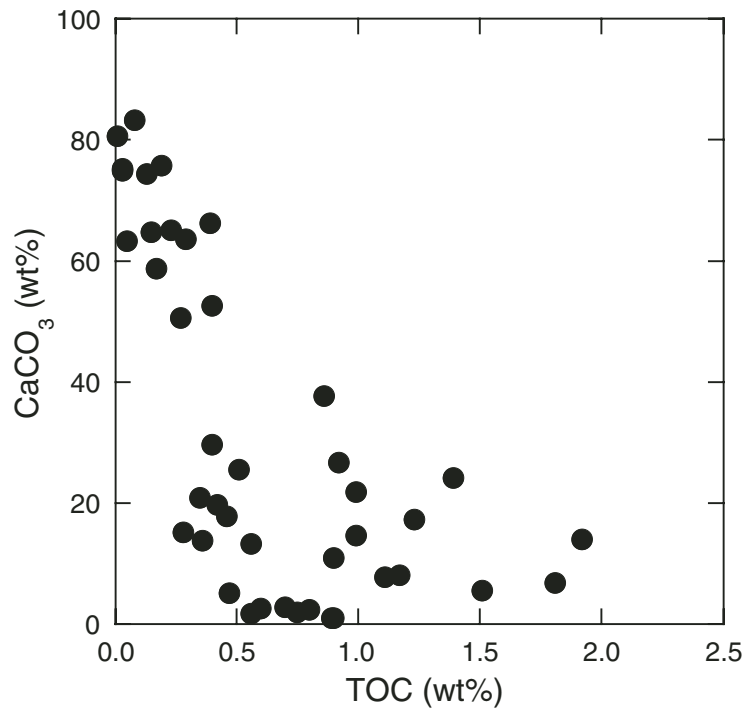


Figure F37. S_2 vs. total organic carbon (TOC) and hydrogen index (HI) vs. TOC for selected samples from Hole 1237B. Boundaries for Types I, II, and III kerogen fields are taken from Langford and Blanc-Valleron (1990).

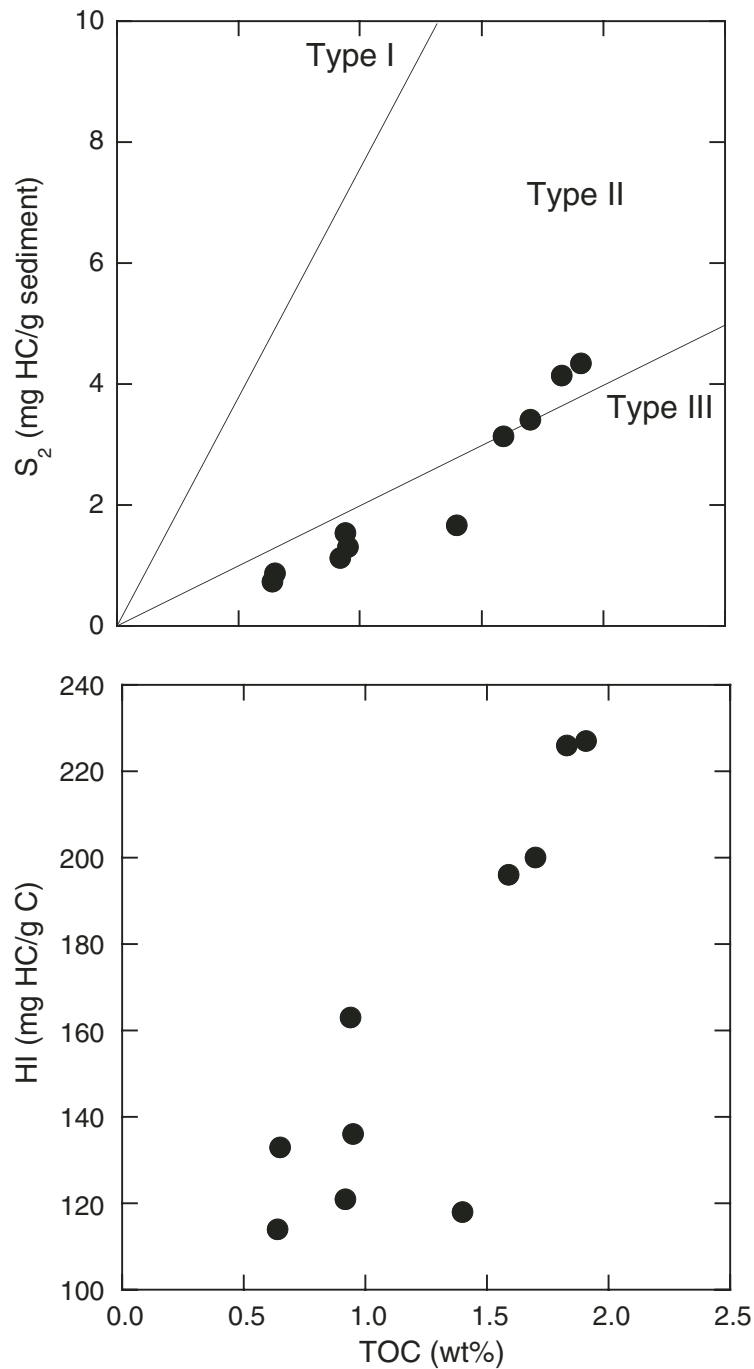


Figure F38. A. Shipboard biostratigraphic and magnetostratigraphic datums and age-depth model. Solid horizontal lines = lithologic unit boundaries, dashed horizontal lines = lithologic subunit boundaries. B. Corrected linear sedimentation rates (LSR), total mass accumulation rates (MAR), and carbonate mass accumulation rates are calculated from the smooth age model, average dry density, and calcium carbonate concentrations at 1-m.y. intervals. FO = first occurrence, LO = last occurrence.

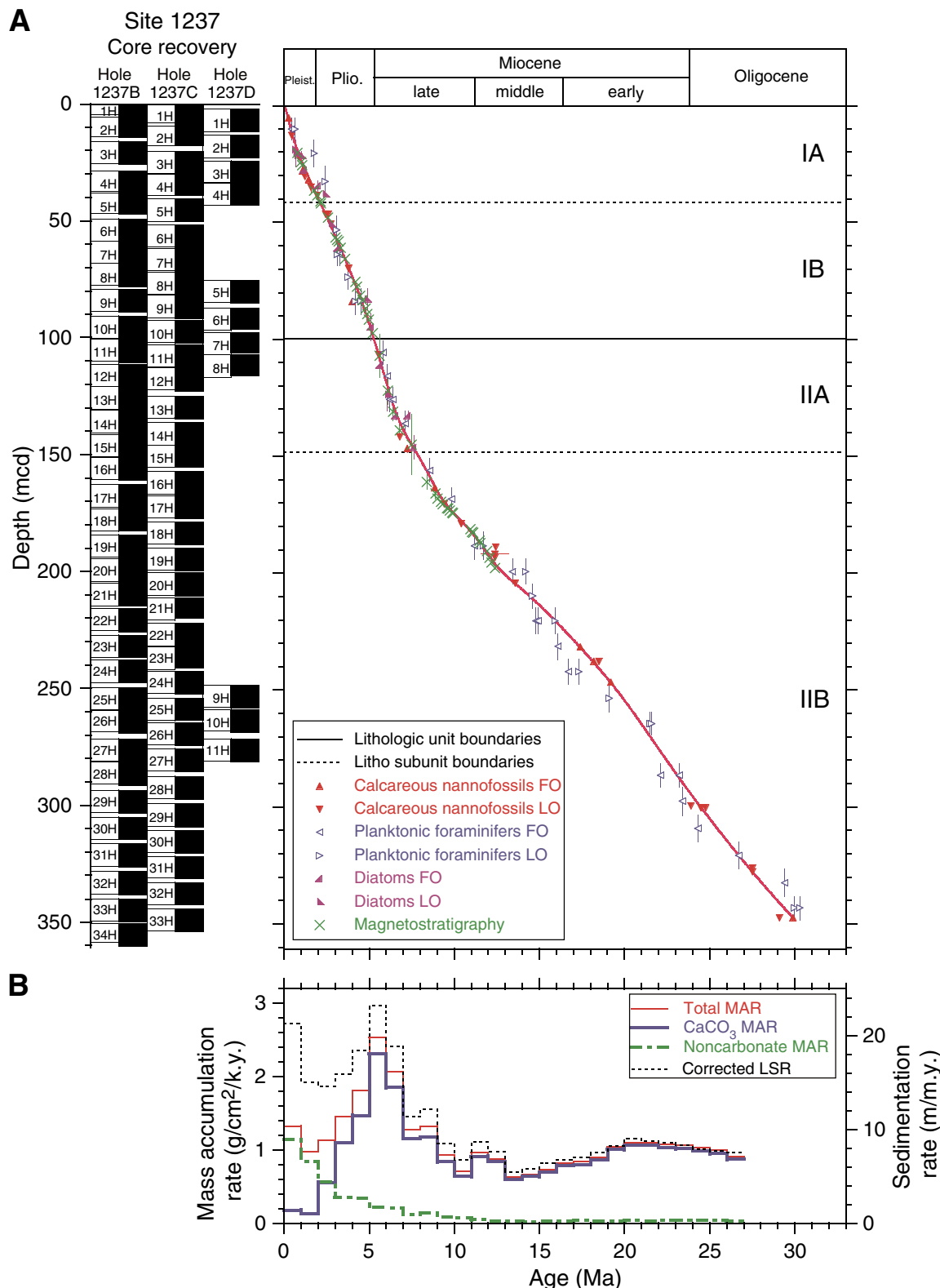
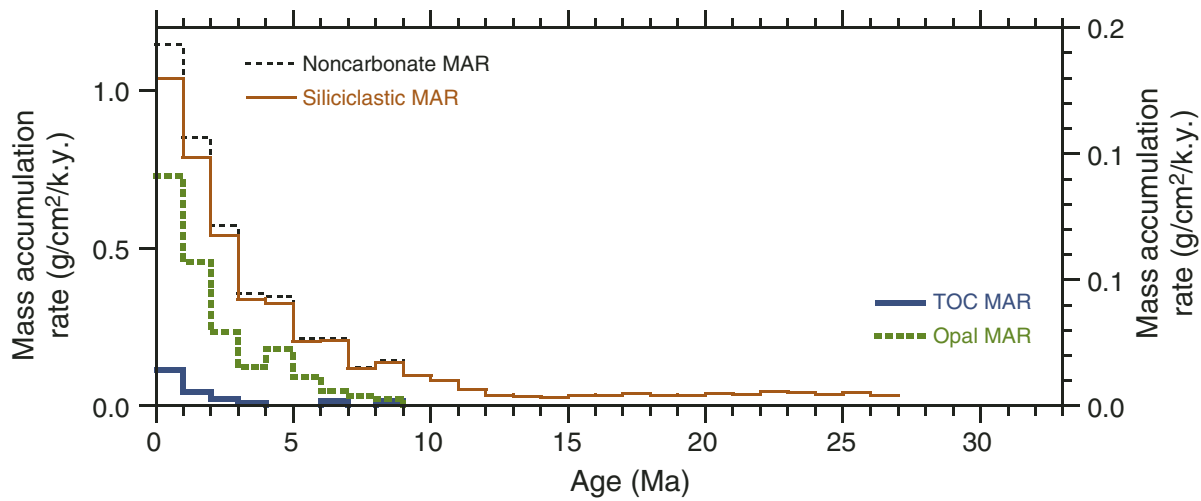


Figure F39. Noncarbonate mass accumulation rates (MARs) and the three major components: total organic carbon (TOC) based on shipboard measurements, biogenic opal measured postcruise (R. Tiedemann, pers. comm., 2002), and siliciclastic grains (noncarbonate – TOC – opal). The rates are averaged over the same 1-m.y. age intervals, as in Fig. F38, p. 71.



SHIPBOARD SCIENTIFIC PARTY
CHAPTER 8, SITE 1237

73

Table T1. Operations summary, Site 1237 (See table notes. Continued on next page.)

Core	Date (2002)	Local time (hr)	Depth (mbsf)		Length (m)		Recovery (%)	APCT	Orientation	NMCB
			Top	Bottom	Cored	Recovered				
202-1237A-										
1H	27 Apr	0415	1.0	10.5	9.5	9.95	104.7			
			Cored totals:		9.5	9.95	104.7			
202-1237B-										
1H	27 Apr	0525	0.0	5.5	5.5	5.54	100.7			X
2H	27 Apr	0625	5.5	15.0	9.5	9.97	105.0			
3H	27 Apr	0725	15.0	24.5	9.5	9.97	105.0		Tensor	
4H	27 Apr	0840	24.5	34.0	9.5	10.01	105.4	X	Tensor	X
5H	27 Apr	0940	34.0	43.5	9.5	10.00	105.3		Tensor	
6H	27 Apr	1050	43.5	53.0	9.5	10.01	105.4	X	Tensor	X
7H	27 Apr	1220	53.0	62.5	9.5	9.82	103.4		Tensor	
8H	27 Apr	1335	62.5	72.0	9.5	10.14	106.7	X	Tensor	X
9H	27 Apr	1425	72.0	81.5	9.5	9.86	103.8		Tensor	
10H	27 Apr	1535	81.5	91.0	9.5	9.75	102.6	X	Tensor	
11H	27 Apr	1650	91.0	100.5	9.5	10.03	105.6		Tensor	
12H	27 Apr	1759	100.5	110.0	9.5	9.36	98.5	X	Tensor	X
13H	27 Apr	2210	110.0	119.5	9.5	9.80	103.2		Tensor	
14H	27 Apr	2335	119.5	129.0	9.5	9.91	104.3	X	Tensor	X
15H	28 Apr	0040	129.0	138.5	9.5	9.79	103.1		Tensor*	
16H	28 Apr	0230	138.5	148.0	9.5	9.71	102.2	X	Tensor*	X
17H	28 Apr	0340	148.0	157.5	9.5	10.00	105.3		Tensor*	
18H	28 Apr	0530	157.5	167.0	9.5	9.65	101.6		Tensor*	X
19H	28 Apr	0645	167.0	176.5	9.5	9.80	103.2		Tensor*	
20H	28 Apr	0820	176.5	186.0	9.5	9.90	104.2		Tensor	X
21H	28 Apr	0920	186.0	195.5	9.5	9.77	102.8		Tensor	
22H	28 Apr	1030	195.5	205.0	9.5	10.03	105.6		Tensor	
23H	28 Apr	1140	205.0	214.5	9.5	9.66	101.7		Tensor	
24H	28 Apr	1445	214.5	224.0	9.5	9.64	101.5		Tensor	
25H	28 Apr	1625	224.0	233.5	9.5	9.69	102.0		Tensor	
26H	28 Apr	0535	233.5	243.0	9.5	9.96	104.8		Tensor	
27H	28 Apr	1850	243.0	252.5	9.5	9.79	103.1		Tensor	
28H	28 Apr	2015	252.5	262.0	9.5	9.98	105.1		Tensor	
29H	28 Apr	2225	262.0	271.5	9.5	9.94	104.6		Tensor	
30H	28 Apr	2340	271.5	281.0	9.5	9.72	102.3		Tensor	
31H	29 Apr	0115	281.0	290.5	9.5	10.05	105.8		Tensor	
32H	29 Apr	0240	290.5	300.0	9.5	10.02	105.5		Tensor	
33H	29 Apr	0410	300.0	309.5	9.5	10.08	106.1		Tensor	
34H	29 Apr	0535	309.5	317.4	7.9	10.00	126.6		Tensor	
		Cored totals:		317.4	331.35	104.4				
202-1237C-										
1H	29 Apr	1005	0.0	9.3	9.3	9.36	100.7	X		X
2H	29 Apr	1100	9.3	18.8	9.5	9.90	104.2			
3H	29 Apr	1205	18.8	28.3	9.5	9.98	105.1		Tensor	X
4H	29 Apr	1300	28.3	37.8	9.5	9.53	100.3		Tensor	
5H	29 Apr	1350	37.8	47.3	9.5	9.91	104.3		Tensor	X
6H	29 Apr	1455	47.3	56.8	9.5	10.23	107.7	X	Tensor	
7H	29 Apr	1545	56.8	66.3	9.5	10.01	105.4		Tensor	X
8H	29 Apr	1645	66.3	75.8	9.5	9.95	104.7		Tensor	
9H	29 Apr	1730	75.8	85.3	9.5	9.94	104.6		Tensor	X
10H	29 Apr	1825	85.3	94.8	9.5	9.95	104.7		Tensor	
11H	29 Apr	1915	94.8	104.3	9.5	9.51	100.1		Tensor	X
12H	29 Apr	2025	104.3	113.8	9.5	10.01	105.4	X	Tensor	
13H	29 Apr	2125	115.8	125.3	9.5	9.92	104.4		Tensor	X
14H	29 Apr	2220	125.3	134.8	9.5	9.95	104.7		Tensor	
15H	29 Apr	2315	134.8	144.3	9.5	9.89	104.1		Tensor	X
16H	30 Apr	0005	144.3	153.8	9.5	10.00	105.3		Tensor	
17H	30 Apr	0120	153.8	163.3	9.5	9.90	104.2		Tensor	X
18H	30 Apr	0240	163.3	172.8	9.5	9.79	103.1		Tensor	
19H	30 Apr	0355	172.8	182.3	9.5	9.70	102.1		Tensor	
20H	30 Apr	0455	182.3	191.8	9.5	9.88	104.0		Tensor	
21H	30 Apr	0620	191.8	201.3	9.5	8.85	93.2		Tensor	
22H	30 Apr	0730	201.3	210.8	9.5	9.99	105.2		Tensor	
23H	30 Apr	0845	210.8	220.3	9.5	8.81	92.7		Tensor	
24H	30 Apr	0955	220.3	229.8	9.5	9.91	104.3		Tensor	
25H	30 Apr	1115	229.8	239.3	9.5	9.73	102.4		Tensor	
26H	30 Apr	1225	239.3	248.8	9.5	9.88	104.0		Tensor*	

Table T1 (continued).

Core	Date (2002)	Local time (hr)	Depth (mbsf)		Length (m)		Recovery (%)	APCT	Orientation	NMCB
			Top	Bottom	Cored	Recovered				
27H	30 Apr	1340	248.8	258.3	9.5	9.95	104.7		Tensor*	
28H	30 Apr	1630	258.3	267.8	9.5	9.88	104.0		Tensor*	
29H	30 Apr	1759	267.8	277.3	9.5	10.13	106.6		Tensor*	
30H	30 Apr	2030	277.3	286.8	9.5	9.90	104.2		Tensor	
31H	30 Apr	2205	286.8	296.3	9.5	9.73	102.4		Tensor	
32H	30 Apr	2320	296.3	305.8	9.5	9.76	102.7		Tensor	
33H	1 May	0140	305.8	315.3	9.5	9.87	103.9		Tensor	
			Cored totals:		313.3	323.70	103.3			
202-1237D-										
1H	1 May	0515	2.8	12.3	9.5	9.80	103.2			
2H	1 May	0610	12.3	21.8	9.5	9.75	102.6		X	
3H	1 May	0710	21.8	31.3	9.5	9.99	105.2			
4H	1 May	0805	31.3	69.8	9.5	9.67	101.8		X	
5H	1 May	0945	69.8	80.3	9.5	9.98	105.1			
6H	1 May	1100	80.3	89.8	9.5	9.37	98.6	Tensor	X	
7H	1 May	1155	89.8	99.3	9.5	8.85	93.2	Tensor		
8H	1 May	1255	99.3	224.5	9.5	8.95	94.2	Tensor*	X	
9H	1 May	1700	224.5	234.0	9.5	9.90	104.2	Tensor		
10H	1 May	1805	234.0	243.5	9.5	9.86	103.8	Tensor		
11H	1 May	1935	243.5	253.0	9.5	9.93	104.5	Tensor		
			Cored Totals:		104.5	106.05	101.5			
			Site totals:		744.7	771.05	103.5			

Notes: APCT = advanced piston corer temperature tool (stainless-steel housing is cutting shoe). NMCB = nonmagnetic core barrel, including cutting shoe (made from monel). X = APCT or NMCB was used. Tensor = brand name for core-barrel orientation tool. * = tensor measurement attempted but problem occurred, resulting in bad or no data.

Table T2. Composite depth scale, Site 1237. (See table notes. Continued on next page.)

Core	Depth of core top		Depth offset		Translation to cmcd	
	Drillers (mbsf)	Composite (mcd)	Cumulative (m)	Differential (m)	Growth factor*	Depth (cmcd)†
202-1237A-						
1H	1.0	1.90	0.90		1	1.74
202-1237B-						
1H	0.0	0.00	0.00		1	0.00
2H	5.5	4.65	-0.85	-0.85	1	4.25
3H	15.0	16.10	1.10	1.95	1	14.70
4H	24.5	28.80	4.30	3.20	1	26.30
5H	34.0	37.27	3.27	-1.03	1	34.04
6H	43.5	49.22	5.72	2.45	1	44.95
7H	53.0	58.57	5.57	-0.15	1	53.49
8H	62.5	68.22	5.72	0.15	1	62.31
9H	72.0	79.37	7.37	1.65	1	72.49
10H	81.5	90.72	9.22	1.85	1	82.86
11H	91.0	100.67	9.67	0.45	1	91.94
12H	100.5	111.27	10.77	1.10	1	101.63
13H	110.0	121.05	11.05	0.28	1	110.56
14H	119.5	131.25	11.75	0.70	1	119.87
15H	129.0	141.55	12.55	0.80	1	129.28
16H	138.5	151.20	12.70	0.15	1	138.10
17H	148.0	162.80	14.80	2.10	2	148.78
18H	157.5	173.23	15.73	0.93	2	157.93
19H	167.0	184.35	17.35	1.62	2	167.68
20H	176.5	194.65	18.15	0.80	2	176.72
21H	186.0	205.20	19.20	1.05	2	185.97
22H	195.5	215.85	20.35	1.15	2	195.31
23H	205.0	227.15	22.15	1.80	2	205.22
24H	214.5	237.85	23.35	1.20	2	214.61
25H	224.0	249.80	25.80	2.45	2	225.09
26H	233.5	259.15	25.65	-0.15	3	233.66
27H	243.0	271.46	28.46	2.81	3	243.95
28H	252.5	281.56	29.06	0.60	3	252.39
29H	262.0	293.61	31.61	2.55	3	262.46
30H	271.5	305.11	33.61	2.00	3	272.07
31H	281.0	316.41	35.41	1.80	3	281.52
32H	290.5	328.31	37.81	2.40	3	291.46
33H	300.0	339.86	39.86	2.05	3	301.12
34H	309.5	350.61	41.11	1.25	3	310.10
202-1237C-						
1H	0.0	0.05	0.05		1	0.05
2H	9.3	8.20	-1.10	-1.15	1	7.49
3H	18.8	20.55	1.75	2.85	1	18.77
4H	28.3	29.75	1.45	-0.30	1	27.17
5H	37.8	40.67	2.87	1.42	1	37.15
6H	47.3	51.77	4.47	1.60	1	47.28
7H	56.8	61.77	4.97	0.50	1	56.42
8H	66.3	71.97	5.67	0.70	1	65.73
9H	75.8	81.97	6.17	0.50	1	74.87
10H	85.3	92.52	7.22	1.05	1	84.50
11H	94.8	102.97	8.17	0.95	1	94.05
12H	104.3	112.92	8.62	0.45	1	103.13
13H	115.8	125.00	9.20	0.58	1	114.17
14H	125.3	136.35	11.05	1.85	1	124.53
15H	134.8	145.85	11.05	0.00	1	133.21
16H	144.3	157.20	12.90	1.85	1	143.58
17H	153.8	167.65	13.85	0.95	2	153.03
18H	163.3	178.80	15.50	1.65	2	162.81
19H	172.8	190.10	17.30	1.80	2	172.72
20H	182.3	200.60	18.30	1.00	2	181.93
21H	191.8	211.25	19.45	1.15	2	191.28
22H	201.3	222.20	20.90	1.45	2	200.88
23H	210.8	232.40	21.60	0.70	2	209.83
24H	220.3	242.70	22.40	0.80	2	218.86
25H	229.8	254.20	24.40	2.00	2	228.95
26H	239.3	264.65	25.35	0.95	3	238.26
27H	248.8	275.76	26.96	1.61	3	247.54
28H	258.3	287.71	29.41	2.45	3	257.53

Table T2 (continued).

Core	Depth of core top		Depth offset		Translation to cmcd	
	Drillers (mbsf)	Composite (mcd)	Cumulative (m)	Differential (m)	Growth factor*	Depth (cmcd)†
29H	267.8	299.41	31.61	2.20	3	267.31
30H	277.3	310.76	33.46	1.85	3	276.80
31H	286.8	321.66	34.86	1.40	3	285.91
32H	296.3	332.91	36.61	1.75	3	295.31
33H	305.8	344.31	38.51	1.90	3	304.84
202-1237D-						
1H	2.8	2.30	-0.50		1	2.10
2H	12.3	13.50	1.20	1.70	1	12.33
3H	21.8	24.35	2.55	1.35	1	22.24
4H	31.3	33.72	2.42	-0.13	1	30.80
5H	69.8	75.47	5.67	3.25	1	68.93
6H	80.3	87.37	7.07	1.40	1	79.80
7H	89.8	97.82	8.02	0.95	1	89.34
8H	99.3	107.37	8.07	0.05	1	98.06
9H	224.5	248.65	24.15	16.08	2	224.08
10H	234.0	258.90	24.90	0.75	3	233.45
11H	243.5	271.51	28.01	3.11	3	243.99

Notes: * = calculated based on mbsf-mcd relationship for splice shown in Figure F10, p. 43. † = cmcd are calculated using the intervals illustrated in Figure F10, p. 43. Interval 1 (0.00–165.22 mcd): $y = 0.913x + 0.00$. Interval 2 (167.10–264.14 mcd): $y = 0.877x + 5.97$. Interval 3 (264.14–360.61 mcd): $y = 0.836x + 17.07$, where y is in cmcd units and x is in mcd units. This table is also available in [ASCII](#).

Table T3. Splice tie points, Site 1237.

Hole, core, section, interval (cm)	Depth			Hole, core, section, interval (cm)	Depth			
	(mbsf)	(mcd)	(cmcd)		(mbsf)	(mcd)	(cmcd)	
202-								
1237B-1H-3, 25.0	3.25	3.25	2.95	Tie to	1237D-1H-1, 95.0	3.75	3.25	2.95
1237D-1H-6, 135.0	11.65	11.15	10.14	Tie to	1237C-2H-2, 145.0	12.25	11.15	10.14
1237C-2H-5, 140.0	16.70	15.60	14.18	Tie to	1237D-2H-2, 60.0	14.40	15.60	14.18
1237D-2H-6, 45.0	20.25	21.45	19.50	Tie to	1237C-3H-1, 90.0	19.70	21.45	19.50
1237C-3H-6, 30.0	26.60	28.35	25.77	Tie to	1237D-3H-3, 100.0	25.80	28.35	25.77
1237D-3H-6, 135.0	30.65	33.20	30.18	Tie to	1237C-4H-3, 45.0	31.75	33.20	30.18
1237C-4H-5, 20.0	34.50	35.95	32.68	Tie to	1237D-4H-2, 85.0	33.53	35.95	32.68
1237D-4H-6, 85.0	39.50	41.92	38.11	Tie to	1237C-5H-1, 125.0	39.05	41.92	38.11
1237C-5H-7, 15.0	46.95	49.82	45.29	Tie to	1237B-6H-1, 60.0	44.10	49.82	45.29
1237B-6H-5, 55.0	50.05	55.77	50.70	Tie to	1237C-6H-3, 100.0	51.30	55.77	50.70
1237C-6H-6, 130.0	56.10	60.57	55.06	Tie to	1237B-7H-2, 50.0	55.00	60.57	55.06
1237B-7H-6, 55.0	61.05	66.62	60.56	Tie to	1237C-7H-4, 35.0	61.65	66.62	60.56
1237C-7H-6, 115.0	65.45	70.42	64.02	Tie to	1237B-8H-2, 70.0	64.70	70.42	64.02
1237B-8H-5, 30.0	68.80	74.52	67.75	Tie to	1237C-8H-2, 105.0	68.85	74.52	67.75
1237C-8H-3, 110.0	70.40	76.07	69.15	Tie to	1237D-5H-1, 60.0	70.40	76.07	69.15
1237D-5H-5, 145.0	77.25	82.92	75.38	Tie to	1237C-9H-1, 95.0	76.75	82.92	75.38
1237C-9H-5, 115.0	82.95	89.12	81.02	Tie to	1237D-6H-2, 25.0	82.05	89.12	81.02
1237D-6H-6, 80.0	88.60	95.67	86.97	Tie to	1237C-10H-3, 15.0	88.45	95.67	86.97
1237C-10H-6, 25.0	93.05	100.27	91.15	Tie to	1237D-7H-2, 95.0	92.25	100.27	91.15
1237D-7H-6, 80.0	98.10	106.12	96.47	Tie to	1237C-11H-3, 15.0	97.95	106.12	96.47
1237C-11H-5, 145.0	102.25	110.42	100.38	Tie to	1237D-8H-3, 5.0	102.35	110.42	100.38
1237D-8H-6, 45.0	107.25	115.32	104.84	Tie to	1237C-12H-2, 90.0	106.70	115.32	104.84
1237C-12H-6, 115.0	112.98	121.60	110.55	Tie to	1237B-13H-1, 55.0	110.55	121.60	110.55
1237B-13H-5, 90.0	116.90	127.95	116.32	Tie to	1237C-13H-2, 145.0	118.75	127.95	116.32
1237C-13H-7, 20.0	125.00	134.20	122.00	Tie to	1237B-14H-2, 145.0	122.45	134.20	122.00
1237B-14H-5, 130.0	126.80	138.55	125.95	Tie to	1237C-14H-2, 70.0	127.50	138.55	125.95
1237C-14H-5, 100.0	132.30	143.35	130.32	Tie to	1237B-15H-2, 30.0	130.80	143.35	130.32
1237B-15H-6, 5.0	136.55	149.10	135.55	Tie to	1237C-15H-3, 25.0	138.05	149.10	135.55
1237C-15H-6, 120.0	143.50	154.55	140.50	Tie to	1237B-16H-3, 35.0	141.85	154.55	140.50
1237B-16H-6, 65.0	146.65	159.35	144.86	Tie to	1237C-16H-2, 65.0	146.45	159.35	144.86
1237C-16H-5, 135.0	151.65	164.55	149.59	Tie to	1237B-17H-2, 25.0	149.75	164.55	149.59
1237B-17H-6, 130.0	156.80	171.60	156.00	Tie to	1237C-17H-3, 92.5	157.75	171.60	156.00
1237C-17H-6, 90.0	162.20	176.05	160.05	Tie to	1237B-18H-3, 15.0	160.32	176.05	160.05
1237B-18H-6, 100.0	165.67	181.40	164.91	Tie to	1237C-18H-2, 110.0	165.90	181.40	164.91
1237C-18H-6, 35.0	171.15	186.65	169.68	Tie to	1237B-19H-2, 80.0	169.30	186.65	169.68
1237B-19H-6, 90.0	175.40	192.75	175.23	Tie to	1237C-19H-2, 115.0	175.45	192.75	175.23
1237C-19H-4, 50.0	177.80	195.10	177.36	Tie to	1237B-20H-1, 45.0	176.95	195.10	177.36
1237B-20H-7, 20.0	185.70	203.85	185.32	Tie to	1237C-20H-3, 25.0	185.55	203.85	185.32
1237C-20H-6, 85.0	190.65	208.95	189.95	Tie to	1237B-21H-3, 75.0	189.75	208.95	189.95
1237B-21H-6, 45.0	193.95	213.15	193.77	Tie to	1237C-21H-2, 40.0	193.70	213.15	193.77
1237C-21H-6, 45.0	199.75	219.20	199.27	Tie to	1237B-22H-3, 35.0	198.85	219.20	199.27
1237B-22H-6, 85.0	203.85	224.20	203.82	Tie to	1237C-22H-2, 50.0	203.30	224.20	203.82
1237C-22H-7, 5.0	210.35	231.25	210.23	Tie to	1237B-23H-3, 110.0	209.10	231.25	210.23
1237B-23H-5, 40.0	211.40	233.55	212.32	Tie to	1237C-23H-1, 115.0	211.95	233.55	212.32
1237C-23H-6, 90.0	219.20	240.80	218.91	Tie to	1237B-24H-2, 145.0	217.45	240.80	218.91
1237B-24H-5, 95.0	221.45	244.80	222.55	Tie to	1237C-24H-2, 60.0	222.40	244.80	222.55
1237C-24H-7, 25.0	229.55	251.95	229.05	Tie to	1237D-9H-3, 30.0	227.80	251.95	229.05
1237D-9H-5, 35.0	230.85	255.00	231.82	Tie to	1237C-25H-1, 80.0	230.60	255.00	231.82
1237C-25H-6, 65.0	237.95	262.35	238.50	Tie to	1237D-10H-3, 45.0	237.45	262.35	238.50
1237D-10H-6, 75.0	242.25	267.15	242.86	Tie to	1237C-26H-2, 100.0	241.80	267.15	242.86
1237C-26H-6, 100.0	247.80	273.15	248.32	Tie to	1237B-27H-2, 18.5	244.69	273.15	248.32
1237B-27H-6, 80.0	251.30	279.76	254.33	Tie to	1237C-27H-3, 100.0	252.80	279.76	254.33
1237C-27H-7, 35.0	258.15	285.11	259.19	Tie to	1237B-28H-3, 55.0	256.05	285.11	259.19
1237B-28H-6, 95.0	260.95	290.01	263.65	Tie to	1237C-28H-2, 80.0	260.60	290.01	263.65
1237C-28H-6, 70.0	266.50	295.91	269.01	Tie to	1237B-29H-2, 80.0	264.30	295.91	269.01
1237B-29H-6, 120.0	270.70	302.31	274.83	Tie to	1237C-29H-2, 140.0	270.70	302.31	274.83
1237C-29H-6, 45.0	275.75	307.36	279.42	Tie to	1237B-30H-2, 75.0	273.75	307.36	279.42
1237B-30H-6, 115.0	280.15	313.76	285.24	Tie to	1237C-30H-2, 150.0	280.30	313.76	285.24
1237C-30H-6, 55.0	285.35	318.81	289.83	Tie to	1237B-31H-2, 90.0	283.40	318.81	289.83
1237B-31H-5, 50.0	287.50	322.91	293.55	Tie to	1237C-31H-1, 125.0	288.05	322.91	293.55
1237C-31H-6, 130.0	295.60	330.46	300.42	Tie to	1237B-32H-2, 65.0	292.65	330.46	300.42
1237B-32H-6, 30.0	298.30	336.11	305.55	Tie to	1237C-32H-3, 20.0	299.50	336.11	305.55
1237C-32H-6, 100.0	304.80	341.41	310.37	Tie to	1237B-33H-2, 5.0	301.55	341.41	310.37
1237B-33H-5, 55.0	306.55	346.41	314.92	Tie to	1237C-33H-2, 60.0	307.90	346.41	314.92
1237C-33H-5, 145.0	313.25	351.76	319.78	Tie to	1237B-34H-1, 115.0	310.65	351.76	319.78
1237B-34H-7, 67.5	319.18	360.29	327.54					

Note: This table is also available in [ASCII](#).

Table T4. OSUS-MS measurements, Hole 1237A.

Core, section, interval (cm)	Depth (mbsf)	Magnetic susceptibility (instrument units)	Run number	Depth from top of core (cm)
202-1237A-				
1H-1, 5	1.05	1.95	18.5	943
1H-1, 10	1.10	2.00	19.4	943
1H-1, 15	1.15	2.05	17.4	943
1H-1, 20	1.20	2.10	14.1	943
1H-1, 25	1.25	2.15	12.9	943
1H-1, 30	1.30	2.20	15.0	943
1H-1, 35	1.35	2.25	19.5	943
1H-1, 40	1.40	2.30	19.9	943
1H-1, 45	1.45	2.35	19.6	943
1H-1, 50	1.50	2.40	17.8	943
1H-1, 55	1.55	2.45	16.4	943
1H-1, 60	1.60	2.50	15.5	943
1H-1, 65	1.65	2.55	14.6	943
1H-1, 70	1.70	2.60	13.9	943
1H-1, 75	1.75	2.65	13.6	943
1H-1, 80	1.80	2.70	13.8	943
1H-1, 85	1.85	2.75	13.9	943
1H-1, 90	1.90	2.80	16.6	943
1H-1, 95	1.95	2.85	18.5	943
1H-1, 100	2.00	2.90	19.9	943
1H-1, 105	2.05	2.95	19.2	943
1H-1, 110	2.10	3.00	19.1	943
1H-1, 115	2.15	3.05	19.0	943
1H-1, 120	2.20	3.10	19.6	943
1H-1, 125	2.25	3.15	17.1	943
1H-1, 130	2.30	3.20	14.7	943
1H-1, 135	2.35	3.25	14.3	943
1H-1, 140	2.40	3.30	13.3	943
1H-1, 145	2.45	3.35	13.4	943
1H-2, 5	2.56	3.46	22.2	944
1H-2, 10	2.61	3.51	27.1	944
1H-2, 15	2.66	3.56	27.4	944
1H-2, 20	2.71	3.61	26.7	944
1H-2, 25	2.76	3.66	24.8	944
1H-2, 30	2.81	3.71	25.2	944
1H-2, 35	2.86	3.76	25.9	944
1H-2, 40	2.91	3.81	23.6	944
1H-2, 45	2.96	3.86	20.3	944
1H-2, 50	3.01	3.91	20.1	944
1H-2, 55	3.06	3.96	21.3	944
1H-2, 60	3.11	4.01	22.7	944
1H-2, 65	3.16	4.06	22.8	944
1H-2, 70	3.21	4.11	22.0	944
1H-2, 75	3.26	4.16	20.4	944
1H-2, 80	3.31	4.21	19.4	944
1H-2, 85	3.36	4.26	18.6	944
1H-2, 90	3.41	4.31	21.8	944
1H-2, 95	3.46	4.36	25.3	944
1H-2, 100	3.51	4.41	25.1	944
1H-2, 105	3.56	4.46	25.9	944
1H-2, 110	3.61	4.51	28.1	944
1H-2, 115	3.66	4.56	27.2	944
1H-2, 120	3.71	4.61	25.9	944
1H-2, 125	3.76	4.66	25.0	944
1H-2, 130	3.81	4.71	23.9	944
1H-2, 135	3.86	4.76	22.3	944
1H-2, 140	3.91	4.81	21.6	944
1H-2, 145	3.96	4.86	20.6	944
1H-3, 5	4.07	4.97	23.1	945
1H-3, 10	4.12	5.02	24.8	945
1H-3, 15	4.17	5.07	22.9	945
1H-3, 20	4.22	5.12	23.7	945
1H-3, 25	4.27	5.17	23.1	945

Note: Only a portion of this table appears here. The complete table is available in [ASCII](#).

Table T5. OSUS-MS measurements, Hole 1237B.

Core, section, interval (cm)	Depth (mbsf)	Depth (mcd)	Magnetic susceptibility (instrument units)	Run number	Depth from top of core (cm)
202-1237B-					
1H-1, 5	0.05	0.05	16.7	952	5
1H-1, 10	0.10	0.10	16.3	952	10
1H-1, 15	0.15	0.15	17.0	952	15
1H-1, 20	0.20	0.20	18.3	952	20
1H-1, 25	0.25	0.25	19.8	952	25
1H-1, 30	0.30	0.30	19.9	952	30
1H-1, 35	0.35	0.35	20.6	952	35
1H-1, 40	0.40	0.40	18.8	952	40
1H-1, 45	0.45	0.45	22.5	952	45
1H-1, 50	0.50	0.50	25.4	952	50
1H-1, 55	0.55	0.55	23.5	952	55
1H-1, 60	0.60	0.60	21.2	952	60
1H-1, 65	0.65	0.65	19.9	952	65
1H-1, 70	0.70	0.70	18.2	952	70
1H-1, 75	0.75	0.75	17.8	952	75
1H-1, 80	0.80	0.80	19.2	952	80
1H-1, 85	0.85	0.85	19.1	952	85
1H-1, 90	0.90	0.90	18.8	952	90
1H-1, 95	0.95	0.95	18.2	952	95
1H-1, 100	1.00	1.00	18.5	952	100
1H-1, 105	1.05	1.05	18.5	952	105
1H-1, 110	1.10	1.10	17.2	952	110
1H-1, 115	1.15	1.15	15.4	952	115
1H-1, 120	1.20	1.20	14.5	952	120
1H-1, 125	1.25	1.25	14.2	952	125
1H-1, 130	1.30	1.30	14.5	952	130
1H-1, 135	1.35	1.35	14.3	952	135
1H-1, 140	1.40	1.40	12.4	952	140
1H-1, 145	1.45	1.45	10.6	952	145
1H-2, 5	1.56	1.56	9.4	953	155
1H-2, 10	1.61	1.61	10.0	953	160
1H-2, 15	1.66	1.66	10.2	953	165
1H-2, 20	1.71	1.71	11.0	953	170
1H-2, 25	1.76	1.76	11.6	953	175
1H-2, 30	1.81	1.81	12.9	953	180
1H-2, 35	1.86	1.86	14.6	953	185
1H-2, 40	1.91	1.91	15.1	953	190
1H-2, 45	1.96	1.96	15.9	953	195
1H-2, 50	2.01	2.01	17.7	953	200
1H-2, 55	2.06	2.06	18.5	953	205
1H-2, 60	2.11	2.11	19.2	953	210
1H-2, 65	2.16	2.16	19.6	953	215
1H-2, 70	2.21	2.21	19.4	953	220
1H-2, 75	2.26	2.26	17.3	953	225
1H-2, 80	2.31	2.31	16.8	953	230
1H-2, 85	2.36	2.36	16.5	953	235
1H-2, 90	2.41	2.41	15.5	953	240
1H-2, 95	2.46	2.46	14.3	953	245
1H-2, 100	2.51	2.51	13.5	953	250
1H-2, 105	2.56	2.56	13.6	953	255
1H-2, 110	2.61	2.61	13.7	953	260
1H-2, 115	2.66	2.66	14.6	953	265
1H-2, 120	2.71	2.71	15.4	953	270
1H-2, 125	2.76	2.76	15.7	953	275
1H-2, 130	2.81	2.81	16.6	953	280
1H-2, 135	2.86	2.86	17.9	953	285
1H-2, 140	2.91	2.91	18.4	953	290
1H-2, 145	2.96	2.96	16.6	953	295
1H-3, 5	3.06	3.06	15.4	954	305
1H-3, 10	3.11	3.11	16.3	954	310
1H-3, 15	3.16	3.16	16.1	954	315
1H-3, 20	3.21	3.21	15.1	954	320
1H-3, 25	3.26	3.26	14.0	954	325

Note: Only a portion of this table appears here. The complete table is available in [ASCII](#).

Table T6. OSUS-MS measurements, Hole 1237C.

Core, section, interval (cm)	Depth (mbsf)	Magnetic susceptibility (instrument units)	Run number	Depth from top of core (cm)
202-1237C-				
1H-1, 5	0.05	0.10	1018	5
1H-1, 10	0.10	0.15	1018	10
1H-1, 15	0.15	0.20	1018	15
1H-1, 20	0.20	0.25	1018	20
1H-1, 25	0.25	0.30	1018	25
1H-1, 30	0.30	0.35	1018	30
1H-1, 35	0.35	0.40	1018	35
1H-1, 40	0.40	0.45	1018	40
1H-1, 45	0.45	0.50	1018	45
1H-1, 50	0.50	0.55	1018	50
1H-1, 55	0.55	0.60	1018	55
1H-1, 60	0.60	0.65	1018	60
1H-1, 65	0.65	0.70	1018	65
1H-1, 70	0.70	0.75	1018	70
1H-1, 75	0.75	0.80	1018	75
1H-1, 80	0.80	0.85	1018	80
1H-1, 85	0.85	0.90	1018	85
1H-1, 90	0.90	0.95	1018	90
1H-1, 95	0.95	1.00	1018	95
1H-1, 100	1.00	1.05	1018	100
1H-1, 105	1.05	1.10	1018	105
1H-1, 110	1.10	1.15	1018	110
1H-1, 115	1.15	1.20	1018	115
1H-1, 120	1.20	1.25	1018	120
1H-1, 125	1.25	1.30	1018	125
1H-1, 130	1.30	1.35	1018	130
1H-1, 135	1.35	1.40	1018	135
1H-1, 140	1.40	1.45	1018	140
1H-1, 145	1.45	1.50	1018	145
1H-2, 5	1.56	1.61	1019	155
1H-2, 10	1.61	1.66	1019	160
1H-2, 15	1.66	1.71	1019	165
1H-2, 20	1.71	1.76	1019	170
1H-2, 25	1.76	1.81	1019	175
1H-2, 30	1.81	1.86	1019	180
1H-2, 35	1.86	1.91	1019	185
1H-2, 40	1.91	1.96	1019	190
1H-2, 45	1.96	2.01	1019	195
1H-2, 50	2.01	2.06	1019	200
1H-2, 55	2.06	2.11	1019	205
1H-2, 60	2.11	2.16	1019	210
1H-2, 65	2.16	2.21	1019	215
1H-2, 70	2.21	2.26	1019	220
1H-2, 75	2.26	2.31	1019	225
1H-2, 80	2.31	2.36	1019	230
1H-2, 85	2.36	2.41	1019	235
1H-2, 90	2.41	2.46	1019	240
1H-2, 95	2.46	2.51	1019	245
1H-2, 100	2.51	2.56	1019	250
1H-2, 105	2.56	2.61	1019	255
1H-2, 110	2.61	2.66	1019	260
1H-2, 115	2.66	2.71	1019	265
1H-2, 120	2.71	2.76	1019	270
1H-2, 125	2.76	2.81	1019	275
1H-2, 130	2.81	2.86	1019	280
1H-2, 135	2.86	2.91	1019	285
1H-2, 140	2.91	2.96	1019	290
1H-2, 145	2.96	3.01	1019	295
1H-3, 5	3.07	3.12	1020	305
1H-3, 10	3.12	3.17	1020	310
1H-3, 15	3.17	3.22	1020	315
1H-3, 20	3.22	3.27	1020	320
1H-3, 25	3.27	3.32	1020	325

Note: Only a portion of this table appears here. The complete table is available in [ASCII](#).

Table T7. OSUS-MS measurements, Hole 1237D.

Core, section, interval (cm)	Depth (mbsf)	Magnetic susceptibility (instrument units)	Run number	Depth from top of core (cm)
202-1237D-				
1H-1, 5	2.85	2.35	1119	5
1H-1, 10	2.90	2.40	1119	10
1H-1, 15	2.95	2.45	1119	15
1H-1, 20	3.00	2.50	1119	20
1H-1, 25	3.05	2.55	1119	25
1H-1, 30	3.10	2.60	1119	30
1H-1, 35	3.15	2.65	1119	35
1H-1, 40	3.20	2.70	1119	40
1H-1, 45	3.25	2.75	1119	45
1H-1, 50	3.30	2.80	1119	50
1H-1, 55	3.35	2.85	1119	55
1H-1, 60	3.40	2.90	1119	60
1H-1, 65	3.45	2.95	1119	65
1H-1, 70	3.50	3.00	1119	70
1H-1, 75	3.55	3.05	1119	75
1H-1, 80	3.60	3.10	1119	80
1H-1, 85	3.65	3.15	1119	85
1H-1, 90	3.70	3.20	1119	90
1H-1, 95	3.75	3.25	1119	95
1H-1, 100	3.80	3.30	1119	100
1H-1, 105	3.85	3.35	1119	105
1H-1, 110	3.90	3.40	1119	110
1H-1, 115	3.95	3.45	1119	115
1H-1, 120	4.00	3.50	1119	120
1H-1, 125	4.05	3.55	1119	125
1H-1, 130	4.10	3.60	1119	130
1H-1, 135	4.15	3.65	1119	135
1H-1, 140	4.20	3.70	1119	140
1H-1, 145	4.25	3.75	1119	145
1H-2, 5	4.36	3.86	1120	155
1H-2, 10	4.41	3.91	1120	160
1H-2, 15	4.46	3.96	1120	165
1H-2, 20	4.51	4.01	1120	170
1H-2, 25	4.56	4.06	1120	175
1H-2, 30	4.61	4.11	1120	180
1H-2, 35	4.66	4.16	1120	185
1H-2, 40	4.71	4.21	1120	190
1H-2, 45	4.76	4.26	1120	195
1H-2, 50	4.81	4.31	1120	200
1H-2, 55	4.86	4.36	1120	205
1H-2, 60	4.91	4.41	1120	210
1H-2, 65	4.96	4.46	1120	215
1H-2, 70	5.01	4.51	1120	220
1H-2, 75	5.06	4.56	1120	225
1H-2, 80	5.11	4.61	1120	230
1H-2, 85	5.16	4.66	1120	235
1H-2, 90	5.21	4.71	1120	240
1H-2, 95	5.26	4.76	1120	245
1H-2, 100	5.31	4.81	1120	250
1H-2, 105	5.36	4.86	1120	255
1H-2, 110	5.41	4.91	1120	260
1H-2, 115	5.46	4.96	1120	265
1H-2, 120	5.51	5.01	1120	270
1H-2, 125	5.56	5.06	1120	275
1H-2, 130	5.61	5.11	1120	280
1H-2, 135	5.66	5.16	1120	285
1H-2, 140	5.71	5.21	1120	290
1H-2, 145	5.76	5.26	1120	295
1H-3, 5	5.86	5.36	1121	305
1H-3, 10	5.91	5.41	1121	310
1H-3, 15	5.96	5.46	1121	315
1H-3, 20	6.01	5.51	1121	320
1H-3, 25	6.06	5.56	1121	325

Note: Only a portion of this table appears here. The complete table is available in [ASCII](#).

Table T8. Lithologic units, Site 1237.

Unit/ Subunit	Top			Base				Description	Interpretation		
	Core, section, interval (cm)	Depth (mbsf)	(mcd)	Core, section, interval (cm)	Depth (mbsf)	(mcd)					
IA	202-			202-				(Nannofossil) diatom clay (Diatom) nannofossil-bearing clay (Silty) clayey diatom/nannofossil ooze	Increasing hemipelagic contribution		
	1237A-1H-1, 0	1.00	1.90	1237A-1H-CC, 23	10.95	11.85	Clay				
	1237B-1H-1, 0	0.00	0.00	1237B-5H-3, 102	38.05	41.32	(Diatom) nannofossil-bearing clay (Silty) clayey diatom/nannofossil ooze				
	1237C-1H-1, 0	0.00	0.05	1237C-5H-1, 61	38.41	41.28					
IB	1237D-1H-1, 0	2.80	2.30	1237D-4H-6, 25	38.93	41.35	Clayey nannofossil ooze				
	1237B-5H-3, 102	38.05	41.32	1237B-10H-7, 9	90.67	99.89					
	1237C-5H-1, 61	38.41	41.28	1237C-10H-5, 127	92.60	99.82					
IIA	1237D-4H-6, 25	38.93	41.35	1237D-7H-2, 46	91.77	99.79	Nannofossil ooze		Pelagic setting with eolian input		
	1237B-10H-7, 9	90.67	99.89	1237B-15H-5, 52	135.56	148.11					
	1237C-10H-5, 127	92.60	99.82	1237C-15H-2, 71	137.02	148.07					
IIB	1237D-7H-2, 46	91.77	99.79	1237D-8H-CC, 18	108.29	116.36	Nannofossil ooze				
	1237B-15H-5, 52	135.56	148.11	1237B-34H-CC, 29	319.54	360.65					
	1237C-15H-2, 71	137.02	148.07	1237C-33H-CC, 25	315.75	354.26					
	1237D-9H-1, 0	224.50	248.65	1237D-11H-CC, 23	253.47	281.48					

Table T9. Ash layers, Site 1237. (See table note. Continued on next page.)

Number	Core, section, interval (cm)	Depth (mcd)		Thickness (cm)	Core, section, interval (cm)	Depth (mcd)		Thickness (cm)	Core, section, interval (cm)	Depth (mcd)		Thickness (cm)
		Top	Bottom			Top	Bottom			Top	Bottom	
1	202-1237A-1H-3, 119-125	6.11	6.17	6	202-1237C-1H-5, 14-20	6.22	6.28	6	202-1237D-1H-3, 84-90	6.15	6.21	6
2	Not found				1H-6, 62-65	8.20	8.23	3	Not found			
3	202-1237B-3H-4, 48-57	21.11	21.20	9	3H-1, 48-62	21.03	21.17	14	2H-5, 9-19	19.61	19.71	10
4	Not found				Not found				3H-2, 46-48	26.32	26.34	2
5	Core gap				3H-5, 135-143	27.94	28.02	8	3H-3, 50-60	27.87	27.97	10
6	Not found				Not found				3H-3, 71-74	28.08	28.11	3
Wash	(Wash) 4H-1, 0-1	28.80	28.81	1					Not found			
7	4H-1, 33-34	29.13	29.14	1	Not found				Not found			
8	4H-1, 52-56	29.32	29.36	4	3H-6, 136-140	29.46	29.50	4	3H-4, 45-51	29.33	29.39	6
9	4H-1, 82-86	29.62	29.66	4	3H-7, 19-24	29.80	29.85	5	3H-4, 76-80	29.64	29.68	4
Wash					4H-1, 3-7	29.78	29.82	4				
10	Not found				Not found				3H-4, 100-103	29.88	29.91	3
Wash					4H-1, 26-31	30.01	30.06	5				
11	Not found				4H-1, 85-92	30.60	30.67	7	3H-5, 24-25	30.63	30.64	1
12	4H-2, 110-115	31.41	31.46	5	4H-2, 7-15	31.33	31.41	8	3H-5, 100-107	31.39	31.46	7
13	4H-3, 7-19	31.89	32.01	12	4H-2, 54-74	31.80	32.00	20	3H-5/6, (5)149-(6)9	31.88	31.99	11
14	Not found				Not found				3H-6, 10-12	32.00	32.02	2
15	4H-3, 35-36	32.17	32.18	1	4H-2, 81-85	32.07	32.11	4	3H-6, 14-19	32.04	32.09	5
16	4H-4, 79-86	34.13	34.20	7	Not found				Not found			
17	5H-1, 89-92	38.16	38.19	3	4H-6, 87-93	38.14	38.20	6	4H-4, 1-8	38.14	38.21	7
18	5H-2, 85-91	39.64	39.70	6	Core gap				4H-5, 0-7	39.60	39.67	7
19	5H-3, 85-102	41.15	41.32	17	5H-1, 44-61	41.11	41.28	17	4H-5/6, (5)149-(6)25	41.09	41.35	26
20	5H-5, 72-74	44.04	44.06	2	Not found				Core gap			
21	15H-5, 80-82	44.12	44.14	2	Not found				Core gap			
22	5H-5, 112-118	44.44	44.50	6	5H-3, 75-80	44.44	44.49	5	Core gap			
23	5H-5, 122-129	44.54	44.61	7	Not found				Core gap			
24	5H-6, 17-20	44.99	45.02	3	Not found				Core gap			
25	Core gap				5H-6, 31-38	48.53	48.60	7	Core gap			
26	6H-2, 17-18	50.90	50.91	1	Core gap				Core gap			
27	6H-2, 20-23	50.93	50.96	3	Core gap				Core gap			
28	6H-2, 139-140	52.12	52.13	1	6H-1, 10-28	51.87	52.05	18	Core gap			
29	6H-3, 12-14	52.36	52.38	2	6H-1, 44-50	52.21	52.27	6	Core gap			
30	6H-3, 40-43	52.64	52.67	3	6H-1, 68-77	52.45	52.54	9	Core gap			
31	7H-6, 85-88	66.94	66.97	3	Not found				Core gap			
32	8H-2, 89-92	70.62	70.65	3	7H-6, 130-140	70.59	70.69	10	Core gap			
33	8H-4, 63-70	73.38	73.45	7	8H-1, 141-148	73.38	73.45	7	Core gap			
34	9H-5, 0-15	85.40	85.55	15	9H-3, 41-57	85.40	85.56	16	Core gap			
35	9H-7, 37-43	88.79	88.85	6	9H-5, 64-72	88.65	88.73	8	6H-1, 127-133	88.64	88.70	6
36	Core gap				9H-6, 21-24	89.73	89.76	3	Not found			
37	10H-6/7, (6)129-(7)9	99.58	99.89	31	10H-5, 93-127	99.48	99.82	34	7H-2, 10-46	99.43	99.79	36
38	11H-5, 33-41	107.04	107.12	8	11H-3, 91-99	106.91	106.99	8	7H-CC, 17-21	106.64	106.68	4
39	12H-4, 34-41	116.13	116.20	7	12H-3, 21-26	116.15	116.20	5	8H-6, 120-127	116.11	116.18	7
40	12H-6, 83-88	119.64	119.69	5	12H-5, 89-93	119.83	119.87	4	Core gap			
41	13H-2, 123-126	123.80	123.83	3	Core gap				Core gap			
42	13H-3, 88-95	124.97	125.04	7	Not found				Core gap			
43	14H-1, 29-33	131.54	131.58	4	13H-5, 47-49	131.51	131.53	2	Core gap			
44	14H-1, 55-62	131.80	131.87	7	13H-5, 67-75	131.71	131.79	8	Core gap			

Table T9 (continued).

Number	Core, section, interval (cm)	Depth (mcd)		Thickness (cm)	Core, section, interval (cm)	Depth (mcd)		Thickness (cm)	Core, section, interval (cm)	Depth (mcd)		Thickness (cm)
		Top	Bottom			Top	Bottom			Top	Bottom	
202-1237B-												
45	14H-1, 109-110	132.34	132.35	1	Not found							Core gap
46	14H-1, 113-114	132.38	132.39	1	13H-5, 123-124	132.27	132.28	1	Core gap			
47	14H-2, 76-82	133.52	133.58	6	13H-6, 98-108	133.53	133.63	10	Core gap			
48	14H-2, 82-83	133.58	133.59	1	13H-6, 108-109	133.63	133.64	1	Core gap			
49	14H-5, 118-123	138.45	138.50	5	14H-2, 52-59	138.37	138.44	7	Core gap			
50	Core gap				14H-4/5, (4)144-(5)14	142.29	142.49	20	Core gap			
Wash	15H-1, 0-16	141.55	141.71	16					Core gap			
51	15H-1, 82-93	142.37	142.48	11	14H-6, 88-98	144.73	144.83	10	Core gap			
52	15H-5, 44-52	148.03	148.11	8	15H-2, 62-71	147.97	148.06	9	Core gap			
53	16H-5, 9-11	157.32	157.34	2	16H-1, 8-10	157.28	157.30	2	Core gap			
54	16H-6, 133-136	160.07	160.10	3	16H-2, 134-136	160.04	160.06	2	Core gap			
55	17H-3, 110-118	166.91	166.99	8	16H-7/CC, (7)70-(cc)3	166.90	166.97	7	Core gap			

Note: Ash layers that could be correlated between holes are located in the same row and printed in bold type.

Table T10. Age-depth control points, Hole 1237B. (See table notes. Continued on next page).

Datum	Source	Age (Ma)		Top sample (FO presence/LO absence)		Bottom sample (LO presence/FO absence)		Age (Ma)		Depth		
		Minimum	Maximum	Core, section, interval (cm)	Depth (mbsf)	Core, section, interval (cm)	Depth (mbsf)	Average	Uncertainty (±)	Average (mbsf)	Average (mcd)	Uncertainty (±m)
FO <i>Emiliania huxleyi</i>	CN	0.26	0.26	202-1237B-1H-4, 75	5.26	202-1237B-1H-CC, 9	5.51	0.26	0.00	5.39	5.39	0.13
FO <i>Globorotalia hirsuta</i>	PF	0.45	0.45	1H-CC, 9	5.51	2H-CC, 24	15.47	0.45	0.00	10.49	10.07	4.98
LO <i>Pseudoemiliania lacunosa</i>	CN	0.46	0.46	2H-5, 75	12.28	2H-7, 40	14.94	0.46	0.00	13.61	12.76	1.33
LO <i>Nitzschia reinholdii</i>	D	0.62	0.62	2H-CC, 24	15.47	3H-5, 75	21.79	0.62	0.00	18.63	18.76	3.16
LO <i>Globorotalia tosaensis</i>	PF	0.65	0.65	1H-CC, 9	5.51	2H-CC, 24	15.47	0.65	0.00	10.49	10.07	4.98
LO <i>Nitzschia fossilis</i>	D	0.70	0.70	2H-CC, 24	15.47	3H-CC, 19	25.00	0.70	0.00	20.24	20.36	4.77
LO <i>Reticulofenestra asanoi</i>	CN	0.88	0.88	3H-4, 60	20.13	3H-5, 60	21.64	0.88	0.00	20.89	21.99	0.75
LO <i>Rhizosolenia matuyamai</i>	D	1.05	1.05	3H-3, 75	18.77	3H-5, 75	21.79	1.05	0.00	20.28	21.38	1.51
FO <i>Reticulofenestra asanoi</i>	CN	1.08	1.08	3H-CC, 19	25.00	4H-1, 75	25.25	1.08	0.00	25.13	27.83	0.13
FO <i>Rhizosolenia matuyamai</i>	D	1.18	1.18	3H-CC, 19	25.00	4H-1, 40	24.90	1.18	0.00	24.95	27.65	-0.05
LO <i>Gephyrocapsa</i> (large)	CN	1.24	1.24	4H-1, 75	25.25	4H-2, 75	26.76	1.24	0.00	26.01	30.31	0.76
FO <i>Gephyrocapsa</i> (large)	CN	1.45	1.45	4H-2, 75	26.76	4H-3, 75	28.27	1.45	0.00	27.52	31.82	0.75
LO <i>Calcidiscus macintyrei</i>	CN	1.59	1.59	4H-3, 75	28.27	4H-6, 75	32.81	1.59	0.00	30.54	34.84	2.27
LO <i>Globigerinoides extremus</i>	PF	1.77	1.77	2H-CC, 24	15.47	3H-CC, 19	25.00	1.77	0.00	20.24	20.36	4.77
LO <i>Discoaster brouweri</i>	CN	1.96	1.96	4H-CC, 20	34.55	5H-1, 75	34.75	1.96	0.00	34.65	38.44	0.10
FO <i>Fragilariopsis doliolus</i>	D	2.00	2.00	4H-3, 40	27.92	4H-6, 40	32.46	2.00	0.00	30.19	34.49	2.27
LO <i>Globorotalia puncticulata</i>	PF	2.41	2.41	3H-CC, 19	25.00	4H-CC, 20	34.55	2.41	0.00	29.78	32.48	4.78
LO <i>Thalassiosira convexa</i> s.l.	D	2.41	2.41	4H-6, 40	32.46	4H-CC, 20	34.55	2.41	0.00	33.51	37.81	1.04
LO <i>Discoaster pentaradiatus</i>	CN	2.44	2.44	5H-6, 75	42.30	5H-CC, 22	44.02	2.44	0.00	43.16	46.43	0.86
LO <i>Discoaster surculus</i>	CN	2.61	2.61	5H-6, 75	42.30	5H-CC, 22	44.02	2.61	0.00	43.16	46.43	0.86
LO <i>Discoaster tamalis</i>	CN	2.76	2.76	6H-1, 75	44.25	6H-2, 75	45.76	2.76	0.00	45.01	50.73	0.75
LO <i>Nitzschia jouseae</i>	D	2.77	2.77	6H-1, 75	44.25	6H-2, 22	45.23	2.77	0.00	44.74	50.46	0.49
LO <i>Dentoglobigerina altispira</i>	PF	3.09	3.09	5H-CC, 22	44.02	6H-CC, 30	53.51	3.09	0.00	48.77	53.26	4.75
LO <i>Sphaeroidinellopsis seminula</i>	PF	3.12	3.12	6H-CC, 30	53.51	7H-CC, 19	62.80	3.12	0.00	58.16	63.80	4.65
FO <i>Rhizosolenia praebengtssoni</i> s.l.	D	3.17	3.17	7H-1, 110	54.10	7H-3, 73	56.74	3.17	0.00	55.42	60.99	1.32
FO <i>Sphaeroidinella dehiscens</i>	PF	3.25	3.25	6H-CC, 30	53.51	7H-CC, 19	62.80	3.25	0.00	58.16	63.80	4.65
LO <i>Globorotalia plesiotumida</i>	PF	3.77	3.77	7H-CC, 19	62.80	8H-CC, 39	72.66	3.77	0.00	67.73	73.38	4.93
LO <i>Reticulofenestra pseudoumbilicus</i>	CN	3.80	3.80	8H-1, 75	63.25	8H-2, 78	64.79	3.80	0.00	64.02	69.74	0.77
FO <i>Pseudoemiliania lacunosa</i>	CN	4.00	4.00	9H-3, 78	75.78	9H-4, 75	77.27	4.00	0.00	76.53	83.91	0.75
LO <i>Globoturborotalia nepenthes</i>	PF	4.20	4.20	8H-CC, 39	72.66	9H-CC, 20	81.86	4.20	0.00	77.26	83.81	4.60
LO <i>Sphaeroidinellopsis kochi</i>	PF	4.53	4.53	8H-CC, 39	72.66	9H-CC, 20	81.86	4.53	0.00	77.26	83.81	4.60
LO <i>Nitzschia cylindrica</i>	D	4.88	4.88	8H-CC, 39	72.66	9H-6, 30	79.83	4.88	0.00	76.25	82.79	3.59
FO <i>Nitzschia jouseae</i>	D	5.12	5.12	9H-CC, 20	81.86	10H-CC, 10	91.29	5.12	0.00	86.58	94.87	4.72
LO <i>Discoaster quinqueramus</i>	CN	5.56	5.56	11H-4, 75	96.28	11H-5, 75	97.79	5.56	0.00	97.04	106.71	0.75
FO <i>Thalassiosira oestrupii</i>	D	5.64	5.64	11H-CC, 25	101.10	12H-1, 22	100.72	5.64	0.00	100.91	111.13	-0.19
FO <i>Globorotalia tumida</i>	PF	5.82	5.82	10H-CC, 10	91.29	11H-CC, 25	101.10	5.82	0.00	96.20	105.64	4.90
LO <i>Nitzschia miocenica</i> s.s.	D	6.08	6.08	12H-4, 38	105.40	13H-CC, 1	119.75	6.08	0.00	112.58	123.49	7.18
FO <i>Globorotalia margaritae</i>	PF	6.09	6.09	11H-CC, 25	101.10	12H-CC, 18	109.81	6.09	0.00	105.46	115.68	4.36
FO <i>Globigerinoides conglobatus</i>	PF	6.20	6.20	12H-CC, 18	109.81	13H-CC, 1	119.75	6.20	0.00	114.78	125.69	4.97
FO <i>Pulletianita primalis</i>	PF	6.40	6.40	12H-CC, 18	109.81	13H-CC, 1	119.75	6.40	0.00	114.78	125.69	4.97
FO <i>Thalassiosira convexa v. aspinosa</i>	D	6.57	6.57	13H-CC, 1	119.75	14H-3, 34	122.86	6.57	0.00	121.31	132.71	1.56
LO Absence interval <i>Reticulofenestra pseudoumbilicus</i> >7 µm	CN	6.80	6.80	14H-CC, 26	129.40	15H-1, 75	129.75	6.80	0.00	129.58	141.73	0.17
FO <i>Globorotalia conomiozea</i>	PF	7.12	7.12	13H-CC, 1	119.75	14H-CC, 26	129.40	7.12	0.00	124.58	135.98	4.83
FO <i>Amaurolitus primus</i>	CN	7.24	7.24	15H-3, 75	132.77	15H-5, 75	135.79	7.24	0.00	134.28	146.83	1.51
FO <i>Nitzschia miocenica</i> s.l.	D	7.30	7.30	13H-CC, 1	119.75	14H-3, 34	122.86	7.30	0.00	121.31	132.71	1.56
FO <i>Nitzschia reinholdii</i>	D	7.64	7.64	14H-CC, 26	129.40	15H-CC, 1	138.66	7.64	0.00	134.03	146.18	4.63

Table T10 (continued).

Datum	Source	Top sample (FO presence/LO absence)			Bottom sample (LO presence/FO absence)			Age (Ma)		Depth		
		Age (Ma)	Core, section, interval (cm)	Depth (mbsf)	Core, section, interval (cm)	Depth (mbsf)	Average	Uncertainty (±)	Average (mbsf)	Average (mcd)	Uncertainty (±m)	
FO <i>Globorotalia plesiotumida</i>	PF	8.58	8.58	15H-CC, 1	138.66	16H-CC, 12	148.21	8.58	0.00	143.44	156.06	4.78
FO absence interval <i>Reticulofenestra pseudoumbilicus</i> >7µm	CN	8.85	8.85	17H-1, 75	148.75	17H-1, 86	148.86	8.85	0.00	148.81	163.61	0.06
LO <i>Discoaster hamatus</i>	CN	9.40	9.40	17H-5, 75	154.78	17H-6, 75	156.28	9.40	0.00	155.53	170.33	0.75
FO <i>Neoglobotrachina acostaensis</i>	PF	9.82	9.82	17H-1, 98	148.98	17H-CC, 21	158.00	9.82	0.00	153.49	168.29	4.51
LO <i>Coccilithus miopelagicus</i>	CN	10.40	10.40	18H-4, 75	162.43	18H-5, 75	163.94	10.40	0.00	163.19	178.92	0.75
FO <i>Globoturborotalita nepenthes</i>	PF	11.19	11.19	18H-CC, 1	166.89	19H-CC, 13	176.81	11.19	0.00	171.85	188.39	4.96
LO <i>Coronocyclus nitescens</i>	CN	12.43	12.43	19H-3, 75	170.78	19H-4, 75	172.29	12.43	0.00	171.54	188.89	0.75
LO <i>Cyclicargolithus floridanus</i>	CN	11.6	13.19	19H-5, 75	173.80	19H-6, 75	175.30	12.40	0.80	174.55	191.90	0.75
LO <i>Globorotalia foehsi</i> s.l.	PF	11.68	11.68	18H-CC, 1	166.89	19H-CC, 13	176.81	11.68	0.00	171.85	188.39	4.96
LO <i>Calcidiscus premacintyrei</i>	CN	12.4	12.4	19H-6, 75	175.30	19H-7, 40	176.46	12.40	0.00	175.88	193.23	0.58
FO <i>Globorotalia foehsi</i> s.l.	PF	13.42	13.42	19H-CC, 13	176.81	20H-CC, 24	186.41	13.42	0.00	181.61	199.36	4.80
LO <i>Sphenolithus heteromorphus</i>	CN	13.57	13.57	20H-7, 40	185.95	20H-CC, 24	186.41	13.57	0.00	186.18	204.33	0.23
LO <i>Globorotalia archeomenardii</i>	PF	14.2	14.2	19H-CC, 13	176.81	20H-CC, 24	186.41	14.20	0.00	181.61	199.36	4.80
LO <i>Globorotalia peripheroranda</i>	PF	14.6	14.6	20H-CC, 24	186.41	21H-CC, 14	195.79	14.60	0.00	191.10	209.78	4.69
FO <i>Globorotalia peripheroacuta</i>	PF	14.80	14.80	21H-CC, 14	195.79	22H-CC, 1	205.44	14.80	0.00	200.62	220.39	4.83
FO <i>Globorotalia praemenardii</i>	PF	14.9	14.9	21H-CC, 14	195.79	22H-CC, 1	205.44	14.90	0.00	200.62	220.39	4.83
LO <i>Globorotalia miozea</i>	PF	15.9	15.9	21H-CC, 14	195.79	22H-CC, 1	205.44	15.90	0.00	200.62	220.39	4.83
FO <i>Globigerinoides diminutus</i>	PF	16.1	16.1	22H-CC, 1	205.44	23H-CC, 16	214.67	16.10	0.00	210.06	231.31	4.62
FO <i>Globorotalia birnageae</i>	PF	16.7	16.7	23H-CC, 16	214.67	24H-CC, 10	224.17	16.70	0.00	219.42	242.17	4.75
LO <i>Globorotalia semivera</i>	PF	17.30	17.30	23H-CC, 16	214.67	24H-CC, 10	224.17	17.30	0.00	219.42	242.17	4.75
LO <i>Catapsydrax dissimilis</i>	PF	17.30	17.30	23H-CC, 16	214.67	24H-CC, 10	224.17	17.30	0.00	219.42	242.17	4.75
FO <i>Calcidiscus premacintyrei</i>	CN	17.40	17.40	23H-3, 75	208.77	23H-4, 75	210.28	17.40	0.00	209.53	231.68	0.75
FO <i>Sphenolithus heteromorphus</i>	CN	18.20	18.20	23H-CC, 16	214.67	24H-1, 75	215.25	18.20	0.00	214.96	237.71	0.29
LO <i>Sphenolithus belemnos</i>	CN	18.50	18.50	23H-CC, 16	214.67	24H-1, 75	215.25	18.50	0.00	214.96	237.71	0.29
LO <i>Globoquadrina binaensis</i>	PF	19.10	19.10	24H-CC, 10	224.17	25H-CC, 10	233.68	19.10	0.00	228.93	253.50	4.76
FO <i>Sphenolithus belemnos</i>	CN	19.20	19.20	24H-6, 75	222.81	24H-7, 40	223.96	19.20	0.00	223.39	246.74	0.57
LO <i>Paragloborotalia kugleri</i>	PF	21.50	21.50	25H-CC, 10	233.68	26H-CC, 9	243.48	21.50	0.00	238.58	264.31	4.90
LO <i>Globoturborotalita angulisuturalis</i>	PF	21.60	21.60	25H-CC, 10	233.68	26H-CC, 9	243.48	21.60	0.00	238.58	264.31	4.90
FO <i>Globoquadrina binaensis</i>	PF	22.10	22.10	27H-CC, 14	252.80	28H-CC, 16	262.48	22.10	0.00	257.64	286.40	4.84
FO <i>Globoquadrina dehiscens</i>	PF	23.20	23.20	27H-CC, 14	252.80	28H-CC, 16	262.48	23.20	0.00	257.64	286.40	4.84
FO <i>Globigerinoides trilobus</i>	PF	23.40	23.40	28H-CC, 16	262.48	29H-CC, 15	271.95	23.40	0.00	267.22	297.55	4.74
LO <i>Reticulofenestra bisecta</i>	CN	23.90	23.90	29H-4, 75	267.27	29H-5, 75	268.78	23.90	0.00	268.03	299.64	0.75
FO <i>Globigerinoides primordius</i> common	PF	24.30	24.30	29H-CC, 15	271.95	30H-CC, 0	281.24	24.30	0.00	276.60	309.21	4.65
LO <i>Zygrhabdolithus bijugatus</i>	CN	24.50	24.50	29H-5, 75	268.78	29H-5, 75	268.78	24.50	0.00	268.78	300.39	0.00
LO <i>Sphenolithus ciperoensis</i>	CN	24.75	24.75	29H-5, 75	268.78	29H-5, 75	268.78	24.75	0.00	268.78	300.39	0.00
FO <i>Globigerinoides primordius</i>	PF	26.70	26.70	30H-CC, 0	281.24	31H-CC, 16	291.07	26.70	0.00	286.16	320.67	4.91
LO <i>Sphenolithus distentus</i>	CN	27.5	27.5	31H-7, 40	290.47	31H-CC, 16	291.07	27.50	0.00	290.77	326.18	0.30
LO <i>Sphenolithus predistentus</i>	CN	27.5	27.5	31H-CC, 16	291.07	32H-1, 75	291.25	27.50	0.00	291.16	327.77	0.09
LO <i>Sphenolithus pseudoradians</i>	CN	29.1	29.1	33H-5, 75	306.78	33H-6, 75	308.29	29.10	0.00	307.54	347.40	0.75
FO <i>Globoturborotalita angulisuturalis</i>	PF	29.40	29.40	31H-CC, 16	291.07	32H-CC, 25	300.54	29.40	0.00	295.81	332.42	4.74
FO <i>Sphenolithus ciperoensis</i>	CN	29.9	29.9	33H-5, 75	306.78	33H-6, 75	308.29	29.90	0.00	307.54	347.40	0.75
LO <i>Subbotina angiporoidea</i>	PF	30.00	30.00	32H-CC, 25	300.54	33H-6, 75	308.29	30.00	0.00	304.42	355.28	3.88
LO <i>Turborotalia ampliapertura</i>	PF	30.30	30.30	32H-CC, 25	300.54	33H-6, 75	308.29	30.30	0.00	304.42	355.16	3.88

Notes: FO = first occurrence, LO = last occurrence. CN = calcareous nannofossils, PF = planktonic foraminifers, D = diatoms.

Table T11. Distribution of calcareous nannofossils, Holes 1237A and 1237B. (See table notes. Continued on next two pages.)

Table T11 (continued).

Table T11 (continued).

Notes: Preservation: G = good, M = moderate, P = poor. Abundance: VA = very abundant, A = abundant, C = common, F = few, R = rare, B = barren.

Table T12. Distribution of planktonic foraminifers, Hole 1237B. (Continued on next page.)

Core, section, interval (cm)	Depth (mbsf)	Depth (mcd)	Preparation	Preservation	Abundance	Benthic/planktonic foraminifers (%)	Remarks	<i>Catapsydrax dissimilis</i>	<i>Catapsydrax unicavis</i>	<i>Dentoglobigerina allispira</i>	<i>Globigerina bulloides</i>	<i>Globigerina euvoluta</i>	<i>Globigerinella quinqueloba</i>	<i>Globigerinella aequilateris</i>	<i>Globorotalia hirsuta</i>	<i>Globigerinoides conglobatus</i>	<i>Globigerinoides extremus</i>	<i>Globigerinoides primordius</i>	<i>Globigerinoides trilobus</i>	<i>Globiquadrina binaensis</i>	<i>Globorotalia birnagae</i>	<i>Globiquadrina dehiscens</i>	<i>Globorotalia archeonotata</i> ??	<i>Globorotalia conoidea</i>	<i>Globorotalia cassidiformis</i>	<i>Globorotalia conomiza</i>	<i>Globorotalia foysi</i>	
202-1237B-Mudline	0.00	0.00	S	G	R	100/0	Large agglutinated, diatom ooze; radiolarians: C																					
1H-CC	5.51	5.51	S	G	A	5/95	Diatoms: F; radiolarians: A	A	F	R	R															R	R	
2H-CC	15.47	14.62	S	G	F	40/60	Diatoms: R; radiolarians: A	C	F	R	C																	
3H-CC	25.00	26.10	S	G	C	10/90	Radiolarians: C	F																				
4H-CC	34.55	38.85	S	P	R	60/40																						
5H-CC	44.02	47.29	S	G	A	5/95																						
6H-CC	53.51	59.23	S	P/M	C	3/97	Radiolarians: F; radiolarians: R; fragmented planktonic foraminifers	R																				
7H-CC	62.80	68.37	S	M	A	2/98	Radiolarians: R; fragmented planktonic foraminifers	F																				
8H-CC	72.66	78.38	S	P	C	2/98	Radiolarians: R; fragmented planktonic foraminifers	F																				
9H-CC	81.86	89.23	S	G	A	2/98	Radiolarians: R; biotite: C; flakes	C																				
10H-CC	91.29	100.51	S	M	C	50/50		C																				
11H-CC	101.10	110.77	S	M/G	A	1/99		F																				
12H-CC	109.80	120.58	S	M/G	A	1/99		F																				
13H-CC	119.80	130.80	S	M/G	A	1/99		C																				
14H-CC	129.40	141.15	S	M/G	A	1/99		C																				
15H-CC	138.70	151.21	S	P/M	A	5/95	Fragmented planktonic foraminifers	C																				
16H-CC	148.20	160.91	S	P/M	A	1/99		R																				
17H-1, 90-91	148.91	163.71	S	P	A	2/98	Radiolarians: R; fragmented planktonic foraminifers	F																				
17H-1, 98-99	148.99	163.79	S	P	A	2/98	Radiolarians: R; radiolarians: A; fragmented planktonic foraminifers	F																				
17H-CC	158.00	172.80	S	P	C	1/99		F																				
18H-CC	166.90	182.62	S	P	C	1/99		F																				
19H-CC	176.80	194.16	S	P/M	A	1/99		C																				
20H-CC	186.40	204.56	S	P/M	A	1/99		C																				
21H-CC	195.80	214.99	S	M	A	1/99		C																				
22H-CC	205.40	225.79	S	M	A	1/99		C																				
23H-CC	214.70	236.82	S	M	A	1/99		C																				
24H-CC	224.20	247.52	S	M	A	1/99		C																				
25H-CC	233.70	259.48	S	M	A	1/99		C																				
26H-CC	243.50	269.13	S	M	A	1/99		C																				
27H-CC	252.80	281.26	S	M	A	1/99		C																				
28H-CC	262.50	291.54	S	M	A	1/99		C																				
29H-CC	272.00	303.56	S	M	A	1/99		C																				
30H-CC	281.20	314.85	S	M	A	1/99		C																				
31H-CC	291.10	326.47	S	M	A	1/99		C																				
32H-CC	300.54	338.35	S	M	A	1/99		C																				
33H-CC	310.09	349.95	S	M	A	1/99		C																				
34H-CC	319.49	360.60	S		B			C																				

Notes: Preparation: S = sieve. Preservation: G = good, M = moderate, P = poor. Abundance: A = abundant, C = common, F = few, R = rare, B = barren.

Table T12 (continued).

Table T13. Distribution of benthic foraminifers, Hole 1237B. (Continued on next page.)

Core, Section	Depth (mbsf)	Depth (mcd)	Preparation	Preservation	Abundance	Benthic/planktonic foraminifers (%)	Anomalinoides emarginatus	Buliminina marginata	Buliminina turpanensis	Cassidinoides sp.	Chilostomella ovoidea	Chrysodiscinum spp.	Cibicidoides incrassatus	Cibicidoides mundulus	Cibicidoides praemundulus	Cibicidoides spp.	Cyclammina sp.	Eggerella bradyi	Epistominella exigua	Eubuliminella exilis	Fissurina spp.	Gaudryina sp.	Glandulina sp.	Globobuliminina affinis	Globobuliminina pyrula	Globocassidulina subglobosa	Globulina gibba	Globulina priscia	Gyroidinoides soldanii	Gyroidinoides orbicularis	Hoeglundina elegans	Karreniella bradyi	Laevidentalina sp.	Laticarinina pauperata	Lenticulina spp.	Marginulina obesa	Martinotella communis	Melonis affinis	Melonis pomphiloides	Neouvigerina ampulacea	Neogloborina longiscata	Nothia excelsa	Nuttallides umbonifera	Oolina sulcata	Oridorsalis umbonatus	Planulina wuellerstorffii
202-1237B-Mudline	0.00	0.00	S	G	R	100/0																																								
1H-CC	5.51	5.51	S	G	A	5/95																																								
2H-CC	15.47	14.62	S	G	F	40/60																																								
3H-CC	25.00	26.10	S	G	C	10/90	1																																							
4H-CC	34.55	38.85	S	P	R	60/40																																								
5H-CC	44.02	47.29	S	G	A	5/95																																								
6H-CC	53.51	59.23	S	P/M	C	3/97																																								
7H-CC	62.80	68.37	S	M	A	2/98																																								
8H-CC	72.66	78.38	S	P	C	2/98																																								
9H-CC	81.86	89.23	S	G	A	2/98	1																																							
10H-CC	91.29	100.51	S	M	C	50/50																																								
11H-CC	101.10	110.77	S	M/G	A	1/99	1																																							
12H-CC	109.80	120.58	S	M/G	A	1/99	3																																							
21H-CC	195.80	214.99	S	M	A	1/99		1	1	2																																				
33H-CC	310.09	349.95	S	M	A	1/99		10	10	3																																				

Notes: Preparation: S = sieve. Preservation: G = good, M = moderate, P = poor. Abundance: A = abundant, C = common, F = few, R = rare, B = barren.

Table T13 (continued).

Core, Section	Depth (mbsf)	Depth (mcd)	Preparation	Preservation	Abundance of planktonic and benthic foraminifers	Benthic/planktonic foraminifers (%)	<i>Pleurostomella alternans</i>	<i>Pleurostomella brevis</i>	<i>Protoglobularina</i> sp.	<i>Pullenia bulloides</i>	<i>Pullenia quinqueloba</i>	<i>Pyrgo murtiniae</i>	<i>Pyrgo serrata</i>	<i>Pyrgo</i> spp.	<i>Pyrulina</i> sp.	<i>Reophax</i> sp.	<i>Spirococulina depressa</i>	<i>Sphaeroidina bulloides</i>	<i>Stilostomella abyssorum</i>	<i>Stilostomella lepidula</i>	<i>Stilostomella subspinosa</i>	<i>Textularia</i> sp. 1	<i>Triloculina</i> sp.	<i>Uvigerina peregrina</i>	<i>Vulvulina spinosa</i>
202-1237B-																									
Mudline	0.00	0.00	S	G	R	100/0											3								
1H-CC	5.51	5.51	S	G	A	5/95											1							29	
2H-CC	15.47	14.62	S	G	F	40/60				1		1	4											1	
3H-CC	25.00	26.10	S	G	C	10/90				1		1	1											28	
4H-CC	34.55	38.85	S	P	R	60/40			1	1		3	4											34	
5H-CC	44.02	47.29	S	G	A	5/95						2	12											1	
6H-CC	53.51	59.23	S	P/M	C	3/97	1					1	10						6					53	
7H-CC	62.80	68.37	S	M	A	2/98	1					1	2	11					1					4	
8H-CC	72.66	78.38	S	P	C	2/98		1		6	8	4	2	2				1	1	2	12		3		
9H-CC	81.86	89.23	S	G	A	2/98	1	2				4	2	11			2		1	3			26		
10H-CC	91.29	100.51	S	M	C	50/50	1	2	14	5	3	2					1		1	1	3	5	100		
11H-CC	101.10	110.77	S	M/G	A	1/99		1	1		3	5	4				2	4	1	11		3	5		
12H-CC	109.80	120.58	S	M/G	A	1/99			1		2	2	5				2		2	2	2	3	25		
21H-CC	195.80	214.99	S	M	A	1/99	1	2		1				1						16			1		
33H-CC	310.09	349.95	S	M	A	1/99	4										21	11						5	

Table T14. Distribution of diatoms, Site 1237. (See table notes. Continued on next three pages.)

Hole, core, section, interval (cm)	Depth (mbsf)	Depth (mcd)	Identification	Method	Abundance	Preservation	<i>Acipteryx senaria</i>	<i>Azpeitia nodulifera</i>	<i>Chaetoceros</i> spp. (resting spores)	<i>Delphinia</i> spp.	<i>Hemidiscus cuneiformis</i>	<i>Nitzschia cylindrica</i>	<i>Nitzschia miocenica</i>	<i>Nitzschia porteri</i>	<i>Nitzschia reinholdii</i>	<i>Nitzschia fossilis</i>	<i>Nitzschia jouseae</i>	<i>Paralia sulcata</i>	<i>Pseudoeunotia dolilus</i>	<i>Rhizosolenia matuyamana</i>	<i>Rhizosolenia praebengonii</i>	<i>Rosselia praepaleacea</i>	<i>Thalassiosira australis</i>	<i>Thalassiosira burckiana</i>	<i>Thalassiosira convexa</i>	<i>Thalassiosira convexa spinosa</i>	Freshwater species	Marine benthic species	Marine neritic species (other)	Marine pelagic species (other)	Remarks					
202-1237A-Mudline	0.00	0.00	PAL	S	VA	G	C	T	VA	C								R	R																	
202-1237B-1H-1, 75	0.75	0.75	Toothpick	S	A	M	F	T	C	F								R																		
1H-2, 75	2.26	2.26	Toothpick	S	C-A	M	F	T	C-A	T								F	T																	
1H-3, 75	3.76	3.76	Toothpick	S	C-A	M	F		C-A	F								A	T																	
2H-4, 20	10.22	9.37	Toothpick	S	C-A	M	R	F	C	F								F																		
202-1237A-1H-CC, 18	10.90	11.80	PAL	S	C	P-M	R	F	C	F								R	R																	
202-1237B-2H-4, 130	11.32	10.47	Toothpick	S	C-A	M	R	F	C-A	F								T	R																	
2H-7, 10	14.64	13.79	Toothpick	S	F-C	M	R	F	F	R-F																										
2H-CC, 24	15.47	14.62	PAL	S/AC	C	P-M	F		C-A	F																										
3H-1, 75	15.75	16.85	Toothpick	S	F	P				F																										
3H-3, 75	18.77	19.87	Toothpick	S	C	M-G	T	A	C-A	R								T	R																	
3H-5, 75	21.79	22.89	Toothpick	S	C	M	R	R	C-A	R																										
4H-1, 40	24.90	29.20	Toothpick	S	C-A	G	F	C	A	F								T	R																	
3H-CC, 19	25.00	26.10	PAL	S/AC	C	P-M	R	R	A	F								R	T																	
4H-3, 40	27.92	32.22	Toothpick	S	C-A	G	F	C	C-A	C																										
4H-5, 40	30.95	35.25	Toothpick	S	C	M	R	R	A	R								R																		
4H-6, 40	32.46	36.76	Toothpick	S	C	M-G		A	F	R-F								T																		
4H-CC, 20	34.55	38.85	PAL	S/AC	C-A	M	R	T	A	C	R							T	R																	
5H-1, 75	34.75	38.02	Toothpick	S	A	G	T		A	T								T?	T																	
5H-4, 75	39.29	42.56	Toothpick	S	F	P	R	F																												
5H-6, 75	42.30	45.57	Toothpick	S	F	M-G	F	F	F	F																										
5H-CC, 22	44.02	47.29	PAL	S/AC	F	M	T	R	T	T								R	T																	
6H-1, 75	44.25	49.97	Toothpick	S	F	P-M	T	T	F	F																										
6H-2, 22	45.23	50.95	Toothpick	S	F	P-M	T	F	A	F								R	T	T																
6H-3, 13	46.65	52.37	Toothpick	S	F-C	M-G	T	F	T									R	R	A																
6H-3, 45	46.97	52.69	Toothpick	S	F	P	F	F	F	F																										
6H-4, 35	48.37	54.09	Toothpick	S	C	M	F	C	R									T	T																	
6H-5, 70	50.22	55.94	Toothpick	S	C	M-G	R	C	F	F								T	T																	
6H-6, 101	52.04	57.76	Toothpick	S	R-F	P-M	F	R	R	R																										
6H-CC, 30	53.51	59.23	PAL	S/AC	F	P-M	R	R	A	F	T							T		T																
7H-1, 110	54.10	59.67	Toothpick	S	C-A	M-G	R			F																										
7H-2, 40	54.91	60.48	Toothpick	S	C	M	R	C	F									T	T																	
7H-3, 73	56.74	62.31	Toothpick	S	T	P				T																										

Very rich in *Stephanopyxis*

Table T14 (continued).

Table T14 (continued).

Hole, core, section, interval (cm)	Depth (mbsf)	Depth (mcd)	Identification	Method	Abundance	Preservation	<i>Actinoptychus senarius</i>	<i>Azpeitia nodulifera</i>	<i>Chaetoceros</i> spp. (resting spores)	<i>Delphineis</i> spp.	<i>Hemidiscus cuneiforms</i>	<i>Nitzschia cylindrica</i>	<i>Nitzschia micrenica</i>	<i>Nitzschia porteri</i>	<i>Nitzschia reinholdii</i>	<i>Nitzschia fossilis</i>	<i>Nitzschia joussea</i>	<i>Paralia sulcata</i>	<i>Pseudocunonia doliolus</i>	<i>Rhizosolenia matuyama</i>	<i>Rhizosolenia praebengonii robusta</i>	<i>Rosselia praepalacea</i>	<i>Thalassiosira oestrupii</i>	<i>Thalassiosira burckiana</i>	<i>Thalassiosira convexa</i>	<i>Thalassiosira convexa aspinosa</i>	<i>Thalassiosira miocenica</i>	<i>Thalassiosira praeconvexa</i>	<i>Thalassionema nitzschioïdes</i>	<i>Thalassiosira</i> spp.	Freshwater species	Marine benthic species	Marine neritic species (other)	Marine pelagic species (other)	Remarks
13H-5, 38	116.43	127.48	Toothpick	S S	B R	P																													
13H-6, 78	118.33	129.38	Toothpick	S PAL	C-A R	M P	C C	R T	R T	C T	F T																								
13H-CC, 1	119.75	130.80	Toothpick	S S	R-F P-M	P																													
14H-1, 95	120.45	132.20	Toothpick	S S	R R	P																													
14H-2, 95	121.96	133.71	Toothpick	S S	R-F P-M	P	T		T	T	T	T																							
202-1237C-																																			
13H-5, 26	122.10	131.30	Toothpick	S S	F R	P-M P	R		R R		R																								
13H-6, 98	124.33	133.53	Toothpick	S S	T R	P																													
202-1237B-																																			
14H-4, 95	124.97	136.72	Toothpick	S S	T R	P																													
202-1237C-																																			
14H-2, 91	127.71	138.77	Toothpick	S S	R R	P-M		R																											
202-1237B-																																			
15H-1, 3	129.03	141.58	Toothpick	S PAL	B S/AC	P	R R	R R		R																									
14H-CC, 26	129.40	141.15	Toothpick	S S/AC	R	P																													
202-1237C-																																			
14H-4, 70	130.50	141.57	Toothpick	S S	F R	M P		R T																											
14H-4, 144	131.24	142.31	Toothpick	S S	R T	P P																													
15H-2, 125	131.76	144.31	Toothpick	S S	T T	P P																													
15H-3, 58	132.60	145.15	Toothpick	S S	R R	P P																													
15H-5, 46	135.50	148.05	Toothpick	S S	R R	P P																													
15H-CC, 1	138.66	151.21	PAL	S S/AC	F F	P P	R F	R R		R T																									
16H-3, 24	141.75	154.45	Toothpick	S S	R R	P P																													
16H-5, 8	144.61	157.31	Toothpick	S S	T T	P P																													
16H-6, 133.5	147.38	160.07	Toothpick	S PAL	S S/AC	B T	P P																												
16H-CC, 12	148.21	160.91	Toothpick	S S/AC	T T	P P																													
17H-1, 30	148.30	163.10	Toothpick	S S	T T	P P																													
17H-3, 124	152.25	167.05	Toothpick	S S	T T	P P																													
17H-4, 30	152.82	167.62	Toothpick	S S	T T	M																													
17H-5, 30	154.33	169.13	Toothpick	S S	B B																														
17H-6, 30	155.83	170.63	Toothpick	S S	B B																														
17H-7, 30	157.33	172.13	Toothpick	S S	B B																														
17H-CC, 21	158.00	172.80	PAL	S S/AC	T T																														
18H-1, 75	158.25	173.98	Toothpick	S S	B B																														
18H-2, 75	159.42	175.15	Toothpick	S S	B B																														
18H-3, 75	160.92	176.65	Toothpick	S S	B B																														
18H-4, 75	162.43	178.16	Toothpick	S S	B B																														

Table T14 (continued).

Hole, core, section, interval (cm)	Depth (mbsf)	Depth (mcd)	Identification	Method	Abundance	Preservation	<i>Actinopytchus senarius</i>	<i>Azpeitia nodulifera</i>	<i>Chaetoceros</i> spp. (resting spores)	<i>Delphineis</i> spp.	<i>Hemidiscus cuneiforms</i>	<i>Nitzschia cylindrica</i>	<i>Nitzschia micenica</i>	<i>Nitzschia porteri</i>	<i>Nitzschia reinholdii</i>	<i>Nitzschia fossilis</i>	<i>Nitzschia joussea</i>	<i>Paralia sulcata</i>	<i>Pseudocunota doliolus</i>	<i>Rhizosolenia matuyama</i>	<i>Rhizosolenia praebergonii robusta</i>	<i>Rosselia praepalacea</i>	<i>Thalassiosira oestrupii</i>	<i>Thalassiosira burckiana</i>	<i>Thalassiosira convexa</i>	<i>Thalassiosira convexa aspinosa</i>	<i>Thalassiosira micenica</i>	<i>Thalassiosira praeconvexa</i>	<i>Thalassionema nitzschioides</i>	<i>Thalassiosira</i> spp.	Freshwater species	Marine benthic species	Marine neritic species (other)	Marine pelagic species (other)	Remarks
18H-5, 75	163.94	179.67	Toothpick	S	B																														
18H-6, 75	165.45	181.18	Toothpick	S	B																														
18H-CC, 1	166.89	182.62	PAL	S/AC	T	P																													
19H-1, 3	167.03	184.38	Toothpick	S/AC	VA	M																													
19H-1, 5	167.05	184.40	Toothpick	S	VA	E																													
19H-3, 67	170.70	188.05	Toothpick	S	B																														
19H-5, 85	173.90	191.25	Toothpick	S	B																														
19H-5, 89	173.94	191.29	Toothpick	S	B																														
19H-CC, 13	176.81	194.16	PAL	S/AC	T	P																													
20H-1, 75	177.25	195.40	Toothpick	S	B																														
20H-2, 137	179.38	197.53	Toothpick	S	B																														
20H-3, 25	179.77	197.92	Toothpick	S	B																														
20H-4, 9	181.11	199.26	Toothpick	S	B																														
20H-5, 10	182.63	200.78	Toothpick	S	B																														
20H-CC, 24	186.41	204.56	PAL	S/AC	B																														
21H-1, 107	187.07	206.27	Toothpick	S	B																														
21H-3, 120	190.22	209.42	Toothpick	S	B																														
21H-5, 132	193.36	212.56	Toothpick	S	B																														
21H-6, 116	194.71	213.91	Toothpick	S	B																														
21H-7, 20	195.26	214.46	Toothpick	S	B																														
22H-1, 10	195.60	215.95	Toothpick	S	B																														
22H-1, 20	195.70	216.05	Toothpick	S	B																														
21H-CC, 14	195.79	214.99	PAL	S/AC	B																														
22H-5, 60	202.13	222.48	Toothpick	S	B																														
22H-6, 140	204.44	224.79	Toothpick	S	B																														
22H-CC, 1	205.44	225.79	PAL	AC	B																														
23H-CC, 16	214.67	236.82	PAL	AC	B																														
24H-CC, 10	224.17	247.52	PAL	AC	B																														
25H-CC, 10	233.68	259.48	PAL	AC	B																														
26H-CC, 9	243.48	269.13	PAL	AC	B																														
27H-CC, 14	252.80	281.26	PAL	AC	B																														
28H-CC, 16	262.48	291.54	PAL	AC	B																														
29H-CC, 15	271.95	303.56	PAL	AC	B																														
30H-CC, 0	281.24	314.85	PAL	AC	B																														
31H-CC, 15	291.06	326.47	PAL	AC	B																														
32H-CC, 25	300.54	338.35	PAL	AC	B																														
33H-CC, 14	310.09	349.95	PAL	AC	B																														
34H-CC, 24	319.49	360.60	PAL	AC	B																														

Notes: PAL = paleontology sample. S = smear slide, AC = acid-centrifuge enrichment method. Abundance: VA = very abundant, A = abundant, C = common, F = few, T = trace, B = barren.

late Miocene contamination?
Contaminated sample down fall???

Table T15. Determinations of polarity chron boundaries, Site 1237. (See table notes. Continued on next page.)

Polarity interval	Core, section	Depth		Core, section	Depth		Core, section	Depth		Polarity chron interpretation	Age (Ma)
		(mbsf)	(mcd)		(mbsf)	(mcd)		(mbsf)	(mcd)		
		202-1237B-			202-1237C-			202-1237D-			
Upper	3H-2	17.90	19.00				2H-4	18.17	19.35	C1n (b) Matuyama/Brunhes	
Middle		20.29						19.86		C1n (b) Matuyama/Brunhes	0.78
Lower	3H-4	20.48	21.58				2H-5	19.17	20.36	C1n (b) Matuyama/Brunhes	
Upper	3H-6	22.90	24.00	3H-3	22.27	24.02				C1r.1n (t) Jaramillo	
Middle		24.22			24.13					C1r.1n (t) Jaramillo	0.99
Lower	3H-7	23.34	24.44	3H-3	22.49	24.24				C1r.1n (t) Jaramillo	
Upper	3H-7	24.59	25.69	3H-3	22.72	24.47	3H-1	22.84	25.39	C1r.1n (b) Jaramillo	
Middle		25.76			25.08			25.52		C1r.1n (b) Jaramillo	1.07
Lower	3H-7*	24.73	25.83	3H-4	23.92	25.69	3H-1	23.09	25.64	C1r.1n (b) Jaramillo	
Upper	4H-5	31.59	35.89	4H-4	34.07	35.53	4H-2	33.54	35.94	C2n (t) Olduvai	
Middle		36.17			36.20			36.57		C2n (t) Olduvai	1.77
Lower	4H-6	32.16	36.45	4H-5	35.42	36.87	4H-3	34.80	37.20	C2n (t) Olduvai	
Upper	5H-1	35.00	38.26	4H-6	36.97	38.43	4H-4	36.06	38.46	C2n (b) Olduvai	
Middle		38.40			38.55			38.65		C2n (b) Olduvai	1.95
Lower	5H-1	35.27	38.54	4H-7*	37.21	38.66	4H-4	36.44	38.84	C2n (b) Olduvai	
Upper	5H-3	37.63	40.92							C2r.1n (t) Reunion	2.14
Middle		41.06								C2r.1n (t) Reunion	
Lower	5H-3	37.93	41.20							C2r.1n (t) Reunion	
Upper	5H-3	38.23	41.48				4H-6	38.93	41.35	C2r.1n (b) Reunion	
Middle		41.75						41.86		C2r.1n (b) Reunion	2.15
Lower	5H-4	38.74	42.03				4H-6	40.04	42.36	C2r.1n (b) Reunion	
Upper				5H-5	44.95	47.82				C2An.1n (t) Gauss/Matuyama	
Middle					47.93					C2An.1n (t) Gauss/Matuyama	2.581
Lower				5H-5	45.17	48.04				C2An.1n (t) Gauss/Matuyama	
Upper	6H-5	50.72	56.44							C2An.1n (b)	
Middle		56.52								C2An.1n (b)	3.04
Lower	6H-5	50.87	56.59							C2An.1n (b)	
Upper	6H-6	51.63	57.37							C2An.2n (t)	
Middle		57.48								C2An.2n (t)	3.11
Lower	6H-6	51.88	57.59							C2An.2n (t)	
Upper	6H-6	52.08	57.82							C2An.2n (b)	
Middle		58.10								C2An.2n (b)	3.22
Lower	6H-7	52.65	58.37							C2An.2n (b)	
Upper	7H-1	54.50	60.60							C2An.3n (t)	
Middle		60.94								C2An.3n (t)	3.33
Lower	7H-2	55.71	61.28							C2An.3n (t)	
Upper	7H-5	59.96	65.53	7H-3	60.06	65.02				C2An.3n (b) Gauss/Gilbert	
Middle		65.92			65.36					C2An.3n (b) Gauss/Gilbert	3.58
Lower	7H-6	60.72	66.31	7H-3	60.73	65.69				C2An.3n (b) Gauss/Gilbert	
Upper	8H-5	69.39	75.13							C3n.1n (t)	
Middle		75.48								C3n.1n (t)	4.18
Lower	8H-6	70.10	75.83							C3n.1n (t)	
Upper	8H-6	71.50	77.23							C3n.1n (b)	
Middle		77.44								C3n.1n (b)	4.29
Lower	8H-7*	71.91	77.65							C3n.1n (b)	
Upper				8H-6	75.21	80.89	5H-4	75.33	81.00	C3n.2n (t)	
Middle					81.34			81.17		C3n.2n (t)	4.48
Lower				8H-7*	76.11	81.78	5H-4	75.67	81.34	C3n.2n (t)	
Upper	9H-2	75.01	82.37	9H-2	77.51	83.68	5H-6	77.99	83.57	C3n.2n (b)	
Middle		83.07			83.86			83.91		C3n.2n (b)	4.62
Lower	9H-3	76.42	83.77	9H-2	77.87	84.04	5H-6	78.59	84.24	C3n.2n (b)	
Upper			84.76								
Upper	9H-5	78.38	85.75	9H-4	81.18	87.37				C3n.3n (t)	
Middle		86.65			87.65					C3n.3n (t)	4.8
Lower	9H-6	80.18	87.56	9H-4	81.76	87.93				C3n.3n (t)	
Upper				9H-5	83.32	89.49	6H-1	81.70	88.70	C3n.3n (b)	
Middle					89.60			88.99		C3n.3n (b)	4.89

Table T15 (continued).

Polarity interval	Core, section	Depth		Core, section	Depth		Core, section	Depth		Polarity chron interpretation	Age (Ma)
		(mbsf)	(mcd)		(mbsf)	(mcd)		(mbsf)	(mcd)		
Lower				9H-6	83.55	89.72	6H-2	82.20	89.27	C3n.3n (b)	
Upper	10H-1	82.00	91.20				6H-3	83.77	90.83	C3n.4n (t)	4.98
Middle			91.82					91.50	C3n.4n (t)		
Lower	10H-2	83.25	92.45				6H-4	85.08	92.17	C3n.4n (t)	
Upper	10H-4	87.41	96.64							C3n.4n (b)	
Middle			97.32							C3n.4n (b)	
Lower	10H-5	88.81	98.00							C3n.4n (b)	5.23
Upper	17H-4	13.22	168.04							C4An (b)	
Middle			168.21							C4An (b)	9.025
Lower	17H-4	153.57	168.38							C4An (b)	
Upper	17H-5	154.48	169.27	17H-2	155.51	169.38				C4Ar.1n (t)	
Middle			169.44					169.61		C4Ar.1n (t)	9.23
Lower	17H-5	154.83	169.61	17H-2	155.96	169.83				C4Ar.1n (t)	
Upper	17H-6	155.68	170.50	17H-2	156.41	170.27				C4Ar.1n (b)	
Middle			170.61					170.44		C4Ar.1n (b)	9.308
Lower	17H-6	155.93	170.72	17H-2	156.76	170.61				C4Ar.1n (b)	
Upper				17H-3	157.99	171.84				C4Ar.2n (t)	
Middle						172.12				C4Ar.2n (t)	9.58
Lower				17H-4	158.55	172.40				C4Ar.2n (t)	
Upper	17H-7	157.48	172.29	17H-4	158.55	172.40				C4Ar.2n (b)	
Middle			172.40					172.51		C4Ar.2n (b)	9.642
Lower	17H-7	157.73	172.51	17H-4	158.77	172.62				C4Ar.2n (b)	
Upper				17H-4	159.11	172.96				C5n.1n (t)	
Middle						173.13				C5n.1n (t)	9.74
Lower				17H-4	159.44	173.29				C5n.1n (t)	
Upper	18H-1	158.20	173.91	17H-5	160.22	174.07				C5n.1n (b)	
Middle			173.99					174.13		C5n.1n (b)	9.88
Lower	18H-1	158.35	174.08	17H-5	160.31	174.18				C5n.1n (b)	
Upper	18H-1	158.45	174.17	17H-5	160.43	174.30				C5n.2n (t)	
Middle			174.40					174.43		C5n.2n (t)	9.92
Lower	18H-2	158.92	174.63	17H-5	160.58	174.55				C5n.2n (t)	
Upper	18H-6	165.40	181.11	18H-2	165.41	180.89				C5n.2n (b)	10.949
Middle			181.28					181.12		C5n.2n (b)	
Lower	18H-6	165.72	181.45	18H-2	165.86	181.34				C5n.2n (b)	
Upper	18H-7	166.65	182.39	18H-3	166.82	182.34				C5r.1n (t)	
Middle			182.47					182.45		C5r.1n (t)	11.052
Lower	18H-7*	166.83	182.56	18H-3	167.04	182.56				C5r.1n (t)	
Upper				18H-3	167.04	182.56				C5r.1n (b)	
Middle						182.73				C5r.1n (b)	11.099
Lower				18H-3	167.38	182.90				C5r.1n (b)	
Upper	19H-2	168.77	186.14	18H-5	170.29	185.81				C5r.2n (t)	
Middle			186.25					186.15		C5r.2n (t)	11.476
Lower	19H-2	169.01	186.36	18H-6	170.97	186.48				C5r.2n (t)	
Upper	19H-2	169.52	186.92	18H-6	171.42	186.92				C5r.2n (b)	
Middle			187.20					187.20		C5r.2n (b)	11.531
Lower	19H-3	170.13	187.48	18H-6	171.98	187.48				C5r.2n (b)	
Upper	19H-4	172.89	190.25							C5An.1n (t)	
Middle			190.54							C5An.1n (t)	11.935
Lower	19H-5	173.50	190.83							C5An.1n (t)	
Upper	19H-6	175.83	193.18							C5An.1n (b)	
Middle			193.51							C5An.1n (b)	12.078
Lower	19H-7*	176.52	193.85							C5An.1n (b)	
Upper	20H-1	177.05	195.19	19H-3	176.72	194.30				C5An.2n (t)	
Middle			195.41					194.75		C5An.2n (t)	12.184
Lower	20H-1	177.50	195.64	19H-4	177.90	195.19				C5An.2n (t)	
Upper	20H-2	178.96	197.09	19H-6	180.81	198.10				C5An.2n (b)	
Middle			197.53					198.44		C5An.2n (b)	12.401
Lower	20H-3	179.82	197.98	19H-6	181.47	198.77				C5An.2n (b)	

Notes: * = near core break. (b) = bottom, (t) = top.

Table T16. Paleomagnetic age control points based on polarity chron boundary and polarity chron interpretation, Site 1237.

Polarity chron boundary interpretation	Polarity chron interpretation	Age (Ma)	Depth (mcd)	Error (\pm m)
C1n (b) Matuyama/Brunhes		0.78	20.3	0.6
C1r.1n (t) Jaramillo		0.99	24.2	0.2
C1r.1n (b) Jaramillo		1.07	25.6	0.2
C2n (t) Olduvai		1.77	36.4	0.4
C2n (b) Olduvai		1.95	38.5	0.3
C2r.1n (t) Reunion		2.14	41.1	0.2
C2r.1n (b) Reunion		2.15	41.9	0.3
C2An.1n (t) Gauss/Matuyama		2.581	47.9	0.2
C2An.1n (b)		3.04	56.5	0.2
C2An.2n (t)		3.11	57.5	0.2
C2An.2n (b)		3.22	58.1	0.2
C2An.3n (t)		3.33	60.9	0.2
C2An.3n (b) Gauss/Gilbert		3.58	65.7	0.3
C3n.1n (t)		4.18	75.5	0.2
C3n.1n (b)		4.29	77.4	0.2
C3n.2n (t)		4.48	81.3	0.2
C3n.2n (b)		4.62	83.3	0.5
C3n.3n (t)		4.8	86.8	0.5
C3n.3n (b)		4.89	89.2	0.3
C3n.4n (t)		4.98	91.6	0.4
C3n.4n (b)		5.23	97.3	0.3
C3r		5.64	107	9.2
C3An.1n		6.1	122	5.8
C3An.2n		6.4	131	3.8
C3Ar		6.8	139	3.5
C3Bn/C3Br/4n		7.5	145	13.0
C4r		8.4	161	3.0
C4An		8.9	166	2.3
C4An (b)		9.025	168.2	0.2
C4Ar.1n (t)		9.23	169.6	0.2
C4Ar.1n (b)		9.308	170.5	0.2
C4Ar.2n (t)		9.58	172.1	0.2
C4Ar.2n (b)		9.642	172.5	0.2
C5n.1n (t)		9.74	173.1	0.2
C5n.1n (b)		9.88	174.0	0.2
C5n.2n (t)		9.92	174.4	0.2
C5n.2n (b)		10.949	181.2	0.2
C5r.1n (t)		11.052	182.5	0.2
C5r.1n (b)		11.099	182.7	0.2
C5r.2n (t)		11.476	186.1	0.2
C5r.2n (b)		11.531	187.2	0.2
C5An.1n (t)		11.935	190.5	0.2
C5An.1n (b)		12.078	193.5	0.2
C5An.2n (t)		12.184	195.4	0.2
C5An.2n (b)		12.401	197.9	0.4

Note: (b) = bottom, (t) = top.

Table T17. Headspace gas analysis, Hole 1237B.

Core, section, interval (cm)	Depth (mbsf)	C ₁ (ppmv)
202-1237B-		
1H-4, 0-5	4.51	4.51
2H-4, 0-5	10.02	9.17
3H-4, 0-5	19.53	20.63
4H-4, 0-5	29.04	33.34
5H-4, 0-5	38.54	41.81
6H-4, 0-5	48.02	53.74
7H-4, 0-5	57.51	63.08
8H-4, 0-5	67.03	72.75
9H-4, 0-5	76.52	83.89
10H-4, 0-5	86.06	95.28
11H-4, 0-5	95.53	105.20
12H-4, 0-5	105.02	115.79
13H-4, 0-5	114.54	125.59
14H-4, 0-5	124.02	135.77
15H-4, 0-5	133.53	146.08
16H-4, 0-5	143.02	155.72
17H-4, 0-5	152.52	167.32
18H-4, 0-5	161.68	177.41
19H-4, 0-5	171.54	188.89
20H-4, 0-5	181.02	199.17
21H-4, 0-5	190.53	209.73
22H-4, 0-5	200.02	220.37
23H-4, 0-5	209.53	231.68
24H-4, 0-5	219.04	242.39
25H-4, 0-5	228.52	254.32
26H-4, 0-5	238.03	263.68
27H-4, 0-5	247.53	275.99
28H-4, 0-5	257.02	286.08
29H-4, 0-5	266.52	298.13
30H-4, 0-5	276.03	309.64
31H-4, 0-5	285.55	320.96
32H-4, 0-5	295.05	332.86
33H-4, 0-5	304.52	344.38
34H-4, 0-5	314.01	355.12

Table T18. Interstitial water geochemical data, Holes 1237A and 1237B.

Core, section, interval (cm)	Depth		pH	Alkalinity (mM)	Salinity	Cl ⁻ (mM)	Na ⁺ (mM)	SO ₄ ²⁻ (mM)	HPO ₄ ²⁻ (μM)	NH ₄ ⁺ (μM)	H ₄ SiO ₄ (μM)	Mn ²⁺ (μM)	Fe ²⁺ (μM)	Ca ²⁺ (mM)	Mg ²⁺ (mM)	B (μM)	Sr ²⁺ (μM)	Ba ²⁺ (μM)	Li ⁺ (μM)	K ⁺ (mM)
	(mbsf)	(mcd)																		
202-1237A-																				
1H-3, 145–150	5.47	6.37	7.76	4.61	35.0	560	485	26.1	8.9	232	784	2.9	BDL	9.7	50.4	522	114	BDL	24	11.8
202-1237B-																				
1H-3, 145–150	4.46	4.46	7.61	4.48	35.0	555	482	26.0	8.9	220	784	5.4	2.5	9.3	49.7	506	105	BDL	24	11.7
2H-3, 145–150	9.97	9.12	7.52	5.12	35.0	560	483	25.5	8.8	270	800	4.1	BDL	9.6	50.6	548	126	BDL	23	12.6
3H-3, 145–150	19.47	20.57	7.49	5.30	35.0	558	487	25.5	8.2	276	792	3.6	BDL	9.4	48.7	501	173	BDL	20	11.3
4H-3, 145–150	28.97	33.27	7.58	4.84	35.0	560	483	25.1	4.8	256	869	3.0	2.2	10.1	49.4	501	219	BDL	19	12.9
5H-3, 145–150	38.48	41.75	7.40	4.46	35.0	561	490	25.6	3.8	235	831	1.9	BDL	9.8	47.6	510	232	BDL	16	11.7
6H-3, 145–150	47.97	53.69	7.40	4.13	35.0	561	482	25.3	2.7	195	780	1.2	2.1	10.1	50.9	496	255	BDL	14	11.8
7H-3, 145–150	57.46	63.03	7.41	3.78	35.0	561	483	25.5	1.9	172	757	0.5	1.6	10.1	50.3	475	254	BDL	13	11.8
8H-3, 145–150	66.98	72.70	7.44	3.58	35.0	563	487	26.0	2.0	148	713	0.5	0.8	10.2	50.1	473	264	BDL	13	11.3
9H-3, 145–150	76.47	83.84	7.43	3.44	35.0	562	484	25.1	2.1	125	715	0.4	BDL	10.2	49.8	466	259	BDL	12	11.5
10H-3, 145–150	86.01	95.23	7.44	3.50	35.0	567	485	25.7	1.8	97	734	0.5	BDL	10.6	51.9	457	257	BDL	12	11.6
11H-3, 145–150	95.47	105.14	7.46	3.21	35.0	563	486	26.0	2.0	73	693	0.3	BDL	10.4	50.3	448	244	BDL	12	10.9
12H-3, 140–150	104.92	115.69	7.48	3.26	34.0	563	480	25.5	1.4	56	632	0.3	BDL	10.6	52.6	448	233	BDL	12	10.8
13H-3, 140–150	114.44	125.49	7.52	3.11	35.0	563	487	26.8	1.4	47	612	0.4	BDL	10.1	51.0	447	219	BDL	13	10.6
14H-3, 140–150	123.92	135.67	7.52	2.78	35.0	564	481	25.9	1.5	45	622	0.2	BDL	10.4	52.9	430	206	BDL	14	11.0
15H-3, 140–150	133.42	145.97	7.51	2.94	34.0	565	489	26.7	1.5	25	610	0.3	BDL	10.1	50.8	443	198	BDL	14	10.6
16H-3, 140–150	142.91	155.61	7.55	2.63	34.0	563	487	26.7	1.2	17	634	0.4	BDL	10.1	50.8	456	192	BDL	17	10.6
17H-3, 140–150	152.41	167.21	7.52	2.70	34.0	562	482	26.3	1.2	15	587	0.3	BDL	10.5	51.6	454	178	BDL	18	10.9
18H-3, 140–150	161.57	177.30	7.53	2.83	34.0	566	487	26.6	1.1	BDL	543	0.2	BDL	10.3	51.8	455	157	BDL	20	11.0
19H-3, 140–150	171.43	188.78	7.56	2.67	35.0	565	482	25.9	1.3	23	483	BDL	BDL	10.4	53.0	465	154	BDL	21	10.8
20H-3, 140–150	180.92	199.07	7.58	2.59	35.0	566	485	27.3	1.0	BDL	406	BDL	BDL	10.5	53.2	446	147	BDL	21	10.5
21H-3, 140–150	190.42	209.62	7.80	2.57	35.0	563	480	26.4	0.7	BDL	371	0.2	BDL	10.4	53.6	450	137	BDL	22	10.6
22H-3, 140–150	199.92	220.27	7.45	2.50	35.0	564	481	27.0	1.0	BDL	361	BDL	BDL	10.4	54.1	476	135	BDL	24	10.9
23H-3, 140–150	209.42	231.57	7.56	2.51	36.0	567	482	27.1	0.8	BDL	340	BDL	BDL	10.8	54.3	460	125	BDL	25	11.1
24H-3, 140–150	218.92	242.27	7.59	2.53	35.0	566	485	27.0	0.8	15	313	BDL	BDL	10.5	52.8	465	121	BDL	25	11.1
25H-3, 140–150	228.42	254.22	7.64	2.28	35.0	570	488	27.5	0.8	BDL	299	0.2	BDL	10.6	53.3	470	113	BDL	25	11.0
26H-3, 140–150	237.92	263.57	7.58	2.38	35.0	562	482	27.6	0.6	BDL	278	BDL	BDL	10.4	53.3	451	110	BDL	25	10.4
27H-3, 140–150	247.42	275.88	7.63	2.17	35.0	566	482	27.6	0.8	BDL	294	BDL	BDL	10.6	54.7	444	104	BDL	26	10.2
28H-3, 140–150	256.92	285.98	7.61	2.33	35.0	565	483	27.3	0.8	12	296	0.3	BDL	10.7	53.3	457	106	BDL	27	10.9
29H-3, 140–150	266.41	298.02	7.65	2.33	35.0	564	485	27.3	0.7	15	276	0.2	BDL	10.4	52.4	462	105	BDL	27	10.5
30H-3, 140–150	275.91	309.52	7.63	2.23	35.0	565	484	27.7	0.8	BDL	290	BDL	BDL	10.8	53.2	455	103	BDL	26	10.5
31H-3, 140–150	285.44	320.85	7.64	2.40	34.0	566	487	27.2	0.7	BDL	286	0.4	BDL	10.5	52.1	471	101	BDL	28	10.1
32H-3, 140–150	294.93	332.74	7.47	2.16	34.0	559	477	27.2	0.7	BDL	301	0.2	BDL	10.7	53.1	463	98	BDL	27	10.5
33H-3, 140–150	304.42	344.28	7.99	2.26	34.0	556	479	27.2	0.7	BDL	311	0.3	BDL	10.4	51.2	457	96	BDL	27	10.5
34H-3, 140–150	313.90	355.01	7.52	2.78	35.0	557	476	27.8	0.6	BDL	296	0.3	BDL	11.0	53.2	450	98	BDL	26	10.8

Note: BDL = below detection limit ($\text{NH}_4^+ = 11 \mu\text{M}$, $\text{Mn}^{2+} = 0.1 \mu\text{M}$, $\text{Fe}^{2+} = 1.1 \mu\text{M}$, $\text{Ba}^{2+} = 0.03 \mu\text{M}$).

Table T19. Inorganic carbon, calcium carbonate, total carbon, total organic carbon, and total nitrogen concentrations, and TOC/TN ratios, Hole 1237B. ([See table note](#). Continued on next two pages.)

Core, section, interval (cm)	Depth		IC (wt%)	CaCO ₃ (wt%)	TC (wt%)	TOC (wt%)	TN (wt%)	TOC/TN (atomic)
	(mbsf)	(mcd)						
202-1237B-								
1H-1, 74-75	0.74	0.74	1.67	13.9	3.59	1.92	0.26	6.46
1H-2, 74-75	2.25	2.25	0.81	6.7	2.62	1.81	0.23	6.72
1H-3, 74-75	3.75	3.75	0.11	0.9	1.01	0.90	0.13	5.86
1H-4, 74-75	5.25	5.25	2.61	21.8	3.60	0.99	0.13	6.71
2H-1, 74-75	6.24	5.39	0.27	2.3	1.07	0.80	0.13	5.30
2H-2, 74-75	7.75	6.90	1.31	10.9	2.21	0.90	0.13	6.09
2H-3, 74-75	9.26	8.41	0.66	5.5	2.17	1.51	0.18	7.17
2H-4, 74-75	10.76	9.91	0.96	8.0	2.13	1.17	0.16	6.45
2H-5, 74-75	12.27	11.42	3.20	26.6	4.12	0.92	0.15	5.25
2H-6, 74-75	13.78	12.93	4.51	37.6	5.37	0.86	0.13	5.79
2H-7, 20-21	14.74	13.89	3.06	25.5	3.57	0.51	0.09	4.79
3H-1, 74-75	15.74	16.84	1.74	14.5	2.73	0.99	0.14	6.04
3H-2, 74-75	17.25	18.35	0.22	1.9	0.97	0.75	0.10	6.66
3H-3, 74-75	18.76	19.86	2.90	24.1	4.29	1.39	0.19	6.41
3H-4, 74-75	20.27	21.37	0.20	1.6	0.76	0.56	0.09	5.19
3H-5, 74-75	21.78	22.88	2.07	17.2	3.30	1.23	0.18	5.90
3H-6, 74-75	23.29	24.39	0.33	2.8	1.03	0.70	0.10	5.76
3H-7, 20-21	24.27	25.37	0.92	7.7	2.03	1.11	0.16	6.10
4H-1, 74-75	25.24	29.54	0.30	2.5	0.90	0.60	0.10	5.23
4H-2, 74-75	26.75	31.05	1.81	15.1	2.09	0.28	0.10	2.40
4H-3, 74-75	28.26	32.56	2.36	19.6	2.78	0.42	0.10	3.70
4H-4, 74-75	29.78	34.08	0.61	5.1	1.08	0.47	0.10	4.13
4H-5, 74-75	31.29	35.59	0.11	0.9	1.00	0.89	0.12	6.30
4H-6, 74-75	32.80	37.10	1.59	13.2	2.15	0.56	0.09	5.11
5H-1, 74-75	34.74	38.01	2.14	17.8	2.60	0.46	0.08	4.87
5H-2, 74-75	36.26	39.53	6.06	50.5	6.33	0.27	0.07	3.38
5H-3, 74-75	37.77	41.04	1.64	13.7	2.00	0.36	0.06	5.18
5H-4, 74-75	39.28	42.55	8.05	67.1	7.83		0.07	
5H-5, 74-75	40.79	44.06	7.63	63.5	7.92	0.29	0.08	2.89
5H-6, 74-75	42.29	45.56	6.30	52.5	6.70	0.40	0.06	5.45
5H-7, 20-21	43.27	46.54	2.50	20.8	2.85	0.35	0.06	4.70
6H-1, 74-75	44.24	49.96	3.56	29.6	3.96	0.40	0.09	3.72
6H-2, 74-75	45.75	51.47	7.04	58.7	7.21	0.17	0.06	2.40
6H-3, 74-75	47.26	52.98	7.77	64.7	7.92	0.15		
6H-4, 74-75	48.76	54.48	9.09	75.7	9.28	0.19		
6H-5, 74-75	50.26	55.98	7.80	65.0	8.03	0.23	0.06	3.10
6H-6, 74-75	51.77	57.49	7.95	66.2	8.34	0.39		
7H-1, 74-75	53.74	59.31	8.70	72.5	7.60		0.06	
7H-2, 74-75	55.25	60.82	9.63	80.2	9.63		0.02	
7H-3, 74-75	56.75	62.32	9.99	83.2	10.07	0.08	0.02	4.11
7H-4, 74-75	58.25	63.82	10.50	87.4	10.45		0.01	
7H-5, 74-75	59.75	65.32	10.14	84.5	10.06		0.11	
7H-6, 74-75	61.26	66.83	7.59	63.2	7.64	0.05	0.01	3.13
7H-7, 20-21	62.23	67.80	8.99	74.9	9.02	0.03	0.02	1.17
8H-1, 74-75	63.24	68.96	9.68	80.6	9.69	0.01	0.01	0.69
8H-2, 74-75	64.75	70.47	9.02	75.2	9.05	0.03	0.01	4.22
8H-3, 74-75	66.27	71.99	8.92	74.3	9.05	0.13	0.02	4.91
8H-4, 74-75	67.77	73.49	6.73	56.0	6.37		0.02	
8H-5, 74-75	69.28	75.00	9.80	81.6	9.72		0.01	
8H-6, 74-75	70.79	76.51	9.69	80.7	9.53		0.01	
8H-7, 20-21	71.76	77.48	10.43	86.9	10.35		0.01	
9H-1, 74-75	72.74	80.11	10.65	88.8	10.55		0.01	
9H-2, 74-75	74.25	81.62	10.08	84.0	10.07		0.01	
9H-3, 74-75	75.76	83.13	10.92	91.0	10.84		0.00	
9H-4, 74-75	77.26	84.63	9.59	79.9	9.50		0.00	
9H-5, 74-75	78.77	86.14	8.62	71.8	8.43		0.01	
9H-6, 74-75	80.27	87.64	10.93	91.0	10.74		0.00	
9H-7, 20-21	81.25	88.62	8.38	69.8	8.31		0.01	
10H-1, 74-75	82.24	91.46	10.91	90.9				
10H-2, 74-75	83.79	93.01	11.06	92.2				
10H-3, 74-75	85.30	94.52	10.91	90.9	10.86		0.00	
10H-4, 74-75	86.80	96.02	10.83	90.2				

Table T19 (continued).

Core, section, interval (cm)	Depth		IC (wt%)	CaCO ₃ (wt%)	TC (wt%)	TOC (wt%)	TN (wt%)	TOC/TN (atomic)
	(mbsf)	(mcd)						
10H-5, 74–75	88.30	97.52	11.10	92.5				
10H-6, 74–75	89.81	99.03	10.70	89.1				
10H-7, 20–21	90.78	100.00	9.35	77.9	9.31		0.01	
11H-1, 74–75	91.74	101.41	10.86	90.5				
11H-2, 74–75	93.25	102.92	11.10	92.5				
11H-3, 74–75	94.76	104.43	10.94	91.2	10.84		0.00	
11H-4, 74–75	96.27	105.94	11.00	91.7				
11H-5, 74–75	97.78	107.45	10.92	91.0				
11H-6, 74–75	99.29	108.96	11.19	93.2				
11H-7, 20–21	100.26	109.93	11.20	93.3				
12H-1, 74–75	101.24	112.01	11.18	93.2				
12H-2, 74–75	102.75	113.52	11.23	93.5				
12H-3, 74–75	104.26	115.03	11.32	94.3	11.20		0.00	
12H-4, 74–75	105.76	116.53	11.35	94.5				
12H-5, 74–75	107.27	118.04	11.20	93.3				
12H-6, 74–75	108.78	119.55	10.48	87.3	8.59		0.01	
12H-7, 20–21	109.24	120.01	10.65	88.7	10.60		0.00	
13H-1, 74–75	110.74	121.79	11.00	91.6				
13H-2, 74–75	112.26	123.31	11.03	91.8				
13H-3, 74–75	113.78	124.83	10.90	90.8	7.68		0.01	
13H-4, 74–75	115.28	126.33	11.08	92.3				
13H-5, 74–75	116.79	127.84	11.09	92.3				
13H-6, 80–81	118.35	129.40	11.19	93.2				
13H-7, 20–21	119.25	130.30	11.12	92.6				
14H-1, 74–75	120.24	131.99	8.81	73.4	9.20			
14H-2, 96–97	121.97	133.72	11.06	92.1				
14H-3, 74–75	123.26	135.01	11.19	93.2				
14H-4, 74–75	124.76	136.51	11.00	91.6				
14H-5, 74–75	126.26	138.01	9.72	80.9				
14H-6, 74–75	127.76	139.51	11.21	93.4				
15H-1, 74–75	129.74	142.29	8.70	72.5	8.64			
15H-2, 74–75	131.25	143.80	11.20	93.3				
15H-3, 74–75	132.76	145.31	11.32	94.3	11.12			
15H-4, 74–75	134.27	146.82	11.28	94.0				
15H-5, 74–75	135.78	148.33	11.26	93.8				
15H-6, 74–75	137.30	149.85	10.95	91.2				
15H-7, 20–21	138.27	150.82	11.16	92.9				
16H-1, 74–75	139.24	151.94	11.24	93.6				
16H-2, 74–75	140.74	153.44	9.80	81.6	9.94			
16H-3, 74–75	142.25	154.95	10.01	83.4				
16H-4, 74–75	143.76	156.46	11.14	92.8				
16H-5, 74–75	145.27	157.97	10.49	87.4				
16H-6, 74–75	146.78	159.48	11.06	92.2				
17H-1, 74–75	148.74	163.54	11.27	93.9				
17H-2, 74–75	150.25	165.05	11.36	94.6				
17H-3, 74–75	151.75	166.55	10.91	90.9				
17H-4, 74–75	153.26	168.06	10.15	84.5				
17H-5, 74–75	154.77	169.57	10.55	87.9				
17H-6, 74–75	156.27	171.07	10.94	91.1				
17H-7, 20–21	157.23	172.03	10.67	88.9				
18H-1, 74–75	158.24	173.97	10.86	90.5				
18H-2, 74–75	159.41	175.14	10.48	87.3				
18H-3, 74–75	160.91	176.64	10.95	91.2				
18H-4, 74–75	162.42	178.15	10.89	90.7				
18H-5, 74–75	163.93	179.66	10.90	90.8				
18H-6, 74–75	165.44	181.17	9.77	81.4				
18H-7, 20–21	166.40	182.13	11.20	93.3				
19H-1, 80–81	167.80	185.15	11.34	94.5				
19H-2, 74–75	169.26	186.61	11.21	93.4				
19H-3, 74–75	170.77	188.12	11.35	94.5				
19H-4, 74–75	172.28	189.63	11.38	94.8				
19H-5, 74–75	173.79	191.14	11.40	94.9				
19H-6, 74–75	175.29	192.64	11.48	95.6				
19H-7, 20–21	176.26	193.61	11.58	96.4				
20H-1, 74–75	177.24	195.39	11.51	95.9				
20H-2, 74–75	178.75	196.90	11.49	95.7				
20H-3, 74–75	180.26	198.41	11.52	96.0				
20H-4, 74–75	181.76	199.91	11.46	95.5				
20H-5, 74–75	183.27	201.42	11.44	95.3				

Table T19 (continued).

Core, section, interval (cm)	Depth (mbsf)	Depth (mcd)	IC (wt%)	CaCO ₃ (wt%)	TC (wt%)	TOC (wt%)	TN (wt%)	TOC/TN (atomic)
20H-6, 74-75	184.78	202.93	11.43	95.2				
20H-7, 20-21	185.75	203.90	11.42	95.2				
21H-1, 74-75	186.74	205.94	11.48	95.7				
21H-3, 74-75	189.76	208.96	11.46	95.5				
21H-5, 74-75	192.78	211.98	11.57	96.4				
22H-1, 74-75	196.24	216.59	11.40	95.0				
22H-3, 74-75	199.26	219.61	11.50	95.8				
22H-5, 74-75	202.27	222.62	11.47	95.6				
23H-1, 74-75	205.74	227.89	11.49	95.7				
23H-3, 74-75	208.76	230.91	11.39	94.9				
23H-5, 74-75	211.77	233.92	11.41	95.1				
24H-1, 74-75	215.24	238.59	11.50	95.8				
24H-3, 74-75	218.26	241.61	11.51	95.9				
24H-5, 74-75	221.29	244.64	11.59	96.5				
25H-1, 74-75	224.74	250.54	11.61	96.7				
25H-3, 74-75	227.76	253.56	11.63	96.9				
25H-5, 74-75	230.76	256.56	11.57	96.4				
26H-1, 74-75	234.24	259.89	11.58	96.5				
26H-3, 74-75	237.26	262.91	11.55	96.2				
26H-5, 74-75	240.28	265.93	11.64	96.9				
27H-1, 74-75	243.74	272.20	11.56	96.3				
27H-3, 74-75	246.76	275.22	11.59	96.6				
27H-5, 74-75	249.78	278.24	11.44	95.3				
28H-1, 74-75	253.24	282.30	11.44	95.3				
28H-3, 74-75	256.26	285.32	11.52	95.9				
28H-5, 74-75	259.27	288.33	11.56	96.3				
29H-1, 74-75	262.74	294.35	11.47	95.6				
29H-3, 74-75	265.75	297.36	11.54	96.2				
29H-5, 74-75	268.77	300.38	11.58	96.4				
30H-1, 74-75	272.24	305.85	11.39	94.9				
30H-3, 74-75	275.25	308.86	11.53	96.1				
30H-5, 74-75	278.28	311.89	11.51	95.9				
31H-1, 74-75	281.74	317.15	11.50	95.8				
31H-3, 74-75	284.78	320.19	11.53	96.1				
31H-5, 74-75	287.80	323.21	11.52	95.9				
33H-1, 74-75	300.74	340.60	11.53	96.0				
33H-3, 74-75	303.76	343.62	11.46	95.4				
33H-5, 74-75	306.77	346.63	11.35	94.6				
34H-1, 74-75	310.24	351.35	11.55	96.2				
34H-3, 74-75	313.24	354.35	11.52	96.0				
34H-5, 74-75	316.26	357.37	11.50	95.8				

Note: IC = inorganic carbon, TC = total carbon, TOC = total organic carbon, TN = total nitrogen.

Table T20. Results of Rock-Eval pyrolysis analyses of selected sediment samples, Hole 1237B.

Core, section, interval (cm)	Depth		TOC (wt%)	S_1 (mg/g)	S_2 (mg/g)	T_{max} (°)	HI (mg HC/g C)
202-1237B-							
1H-1, 74–75	0.74	0.74	1.91	0.22	4.34	416	227
1H-2, 74–75	2.25	2.25	1.83	0.20	4.14	419	226
1H-3, 74–75	3.75	3.75	0.95	0.09	1.30	380	136
2H-1, 74–75	6.24	5.39	0.65	0.09	0.87	399	133
2H-3, 74–75	9.26	8.41	1.70	0.14	3.41	423	200
2H-5, 74–75	12.27	11.42	0.92	0.07	1.12	404	121
3H-1, 74–75	15.74	16.84	0.94	0.09	1.54	407	163
3H-3, 74–75	18.76	19.86	1.59	0.19	3.13	407	196
3H-4, 74–75	20.27	21.37	0.64	0.05	0.73	382	114
3H-7, 20–21	24.27	25.37	1.40	0.09	1.66	408	118

Notes: TOC = total organic carbon. S_1 = amount of volatile hydrocarbons, S_2 = amount of hydrocarbons due to thermal cracking of kerogen. T_{max} = peak temperature of kerogen breakdown. HI = hydrogen index ($100 \times S_2/TOC$).

Table T21. Age-depth model, linear sedimentation rates, and mass accumulation rates, Site 1237.

Age (Ma)	Depth (mcd)	LSR (mcd/m.y.)	mcd growth factor	Corrected LSR (m/m.y.)	Dry density (g/cm ³)	CaCO ₃ average concentration (wt%)	TOC average concentration (wt%)	Opal average concentration (wt%)	Total MAR (g/cm ² /k.y.)	CaCO ₃ MAR (g/cm ² /k.y.)	TOC MAR (g/cm ² /k.y.)	Opal MAR (g/cm ² /k.y.)	Noncarbonate MAR (g/cm ² /k.y.)
0.0	0.0												
1.0	23.3	23.3	1.09	21.3	0.62	13.7	1.08	6.88	1.33	0.18	0.014	0.091	1.15
2.0	39.7	16.4	1.09	15.0	0.65	13.5	0.58	5.82	0.98	0.13	0.006	0.057	0.85
3.0	55.6	16.0	1.09	14.6	0.77	49.6	0.26	2.59	1.13	0.56	0.003	0.029	0.57
4.0	72.9	17.3	1.09	15.9	0.91	75.6	0.08	1.06	1.45	1.10	0.001	0.015	0.35
5.0	93.1	20.1	1.09	18.5	0.99	81.0	0.00	1.24	1.82	1.47	0.000	0.023	0.34
6.0	118.4	25.3	1.09	23.2	1.09	91.4	0.00	0.47	2.53	2.32	0.000	0.012	0.22
7.0	138.9	20.5	1.09	18.8	1.10	89.7	0.10	0.30	2.07	1.85	0.002	0.006	0.21
8.0	151.3	12.4	1.09	11.3	1.13	90.3	0.00	0.30	1.29	1.16	0.000	0.004	0.12
9.0	165.0	13.8	1.13	12.2	1.09	89.3	0.14	0.20	1.33	1.18	0.002	0.003	0.14
10.0	174.7	9.7	1.13	8.6	1.09	89.8			0.93	0.84			0.10
11.0	182.3	7.6	1.13	6.8	1.06	89.1			0.72	0.64			0.08
12.0	192.2	9.9	1.13	8.7	1.11	94.4			0.97	0.92			0.05
13.0	200.9	8.7	1.13	7.7	1.15	95.9			0.88	0.85			0.04
14.0	207.1	6.2	1.13	5.5	1.15	95.3			0.63	0.60			0.03
15.0	213.7	6.6	1.13	5.9	1.14	95.9			0.67	0.64			0.03
16.0	220.9	7.2	1.13	6.4	1.14	95.4			0.73	0.70			0.03
17.0	228.6	7.6	1.13	6.8	1.22	95.6			0.83	0.79			0.04
18.0	236.6	8.0	1.13	7.1	1.19	95.0			0.85	0.80			0.04
19.0	245.1	8.5	1.13	7.5	1.20	96.1			0.90	0.87			0.04
20.0	254.4	9.3	1.13	8.2	1.26	96.8			1.04	1.01			0.03
21.0	264.6	10.2	1.13	9.0	1.23	96.4			1.11	1.07			0.04
22.0	275.1	10.5	1.20	8.8	1.26	96.6			1.11	1.07			0.04
23.0	285.5	10.4	1.20	8.7	1.25	95.8			1.08	1.04			0.05
24.0	295.5	10.0	1.20	8.3	1.28	95.9			1.06	1.02			0.04
25.0	305.0	9.5	1.20	7.9	1.30	96.3			1.03	0.99			0.04
26.0	314.3	9.2	1.20	7.7	1.30	95.6			1.00	0.95			0.04
27.0	323.3	9.0	1.20	7.5	1.21	95.9			0.91	0.88			0.04
28.0	332.2	8.9	1.20	7.4	1.20				0.89	0.00			0.89

Notes: LSR = linear sedimentation rate, MAR = mass accumulation rate. TOC = total organic carbon. This table is also available in [ASCII](#).